



HAL
open science

Experimental and numerical analysis of the impact of the variability of the microstructural properties of thermoplastics reinforced with short mineral or natural fibers on the dynamic mechanical behavior

Julien Proy

► **To cite this version:**

Julien Proy. Experimental and numerical analysis of the impact of the variability of the microstructural properties of thermoplastics reinforced with short mineral or natural fibers on the dynamic mechanical behavior. Mechanics of materials [physics.class-ph]. Université Polytechnique Hauts-de-France, 2023. English. NNT : 2023UPHF0009 . tel-04208268

HAL Id: tel-04208268

<https://theses.hal.science/tel-04208268>

Submitted on 15 Sep 2023

HAL is a multi-disciplinary open access archive for the deposit and dissemination of scientific research documents, whether they are published or not. The documents may come from teaching and research institutions in France or abroad, or from public or private research centers.

L'archive ouverte pluridisciplinaire **HAL**, est destinée au dépôt et à la diffusion de documents scientifiques de niveau recherche, publiés ou non, émanant des établissements d'enseignement et de recherche français ou étrangers, des laboratoires publics ou privés.



Thèse de doctorat
Pour obtenir le grade de Docteur de
L'UNIVERSITE POLYTECHNIQUE HAUTS-DE-FRANCE
et de l'INSA HAUTS-DE-FRANCE

Mécanique des solides, des matériaux, des structures et des surfaces

Présentée et soutenue par Julien, PROY.

Le 31/01/23, à Valenciennes

École doctorale :

École Doctorale Polytechnique Hauts-de-France (ED PHF n°635)

Équipe de Recherche, Laboratoire :

Laboratoire d'Automatique, de Mécanique et d'Informatique Industrielles et Humaines
(LAMIH – UMR CNRS 8201)

Analyse expérimentale et numérique de l'impact de la variabilité des propriétés microstructurales de thermoplastiques renforcés par fibres courtes minérales ou végétales sur le comportement mécanique dynamique

JURY

- DRUESNE, Frédéric. Professeur contractuel, Roberval, UTC de Compiègne, Rapporteur et président de jury.
- PLACET, Vincent. Ingénieur de Recherche HDR, FEMTO-ST, Université de Franche-Comté, Rapporteur.
- BAHLOULI, Nadia. Professeur des Universités, ICUBE, Université de Strasbourg, Examinatrice.
- LAURO, Franck. Professeur des Universités, LAMIH, UPHF, Directeur de thèse.
- TISON, Thierry. Professeur des Universités, LAMIH, UPHF, co-Directeur de thèse. (†)
- MASSA, Franck. Maître de Conférences, LAMIH, INSA HdF, co-encadrant.
- NOTTA-CUVIER, Delphine. Maître de Conférences, LAMIH, INSA HdF, co-encadrante.
- DOGGUI, Mehdi. Manager calcul côté mécanique, Novarès Lens, invité.



PhD Thesis
Submitted for the degree of Doctor of Philosophy from
UNIVERSITE POLYTECHNIQUE HAUTS-DE-FRANCE
and l'INSA HAUTS-DE-FRANCE

mechanics of solids, materials, structures and of surfaces

Presented and defended by **Julien, PROY.**

On **31/01/23**, at Valenciennes

Doctoral school :

Doctoral School Polytechnique Hauts-de-France (ED PHF n°635)

Research unit :

Laboratory of Industrial and Human Automation control Mechanical engineering and Computer science (LAMIH – UMR CNRS 8201)

Experimental and numerical analysis of the impact of the variability of the microstructural properties of thermoplastics reinforced with short mineral or natural fibers on the dynamic mechanical behavior

JURY

- DRUESNE, Frédéric. Professors , Roberval, UTC de Compiègne, Referee and jury president.
- PLACET, Vincent. Research engineer HDR, FEMTO-ST, Université de Franche-Comté, Referee.
- BAHLOULI, Nadia. Professors, ICUBE, Université de Strasbourg, Examiner.
- LAURO, Franck. Professors, LAMIH, UPHF, Thesis director.
- TISON, Thierry. Professors, LAMIH, UPHF, Thesis co-director. (†)
- MASSA, Franck. Associate professor, LAMIH, INSA HdF, Co-supervisor.
- NOTTA-CUVIER, Delphine. Associate professor, LAMIH, INSA HdF, Co-supervisor.
- DOGGUI, Mehdi. Mechanical engineer, Novares Lens, Guest.

This work is licensed under the Creative Commons Attribution International License (CC BY NC ND 2.0 FR). Please find more informations on <https://creativecommons.org/licenses/by-nc-nd/2.0/fr/deed.en%7D>.



Remerciements

Ce projet est cofinancé par l'Union européenne avec le Fonds européen de développement régional.

Tout d'abord, je tiens à remercier l'équipe de Novarès - Lens, M. Doggui, S. Kingue, J. Stelletta et surtout G. Spingler pour leur accueil ainsi que pour toutes les discussions que nous avons pu avoir. Je remercie aussi la région des Hauts-de-France pour le financement de cette thèse.

Ensuite, je remercie mon équipe d'encadrement à savoir mes deux directeurs de thèse F. Lauro et T. Tison pour leur supervision ainsi que leurs conseils. Aussi, je remercie tout particulièrement mes deux encadrants F. Massa et D. Notta-Cuvier sans qui ce travail n'aurait pu aboutir. Egalement, je remercie l'ensemble des personnes travaillant au Lamih avec qui j'ai travaillé de près ou de loin.

Je tiens à remercier les membres de mon jury de thèse, N. Bahlouli, F. Druesne et V. Placet pour l'analyse et l'évaluation de cette thèse.

Je remercie l'ensemble de mes collègues Xavier, Hugo, Benjam', Hans et tous les autres pour les moments que nous avons pu passer ensemble. Tout particulièrement, je remercie mes collègues de bureau, Yassine, Jérémy, Martin et Maxime pour toutes les discussions et tous les fous rires que nous avons pu avoir.

Je souhaite remercier Nico pour tout, les soirées jeux vidéos / de sociétés et toutes nos discussions. Egalement, je remercie ma famille, ma soeur, mon frère et mes parents sans qui je ne serais pas arrivé jusqu'ici. Enfin, last but not least, je souhaite dire un gros MERCI à toi pépé, pour m'avoir supporté, soutenu et encouragé pendant mes trois années.

Contents

Table of Contents	vii
List of Figures	ix
List of Tables	xiii
Introduction	1
1 State of the art	7
1.1 Investigation of short-fiber-reinforced thermoplastics' microstructure	8
1.1.1 Short fibers	8
1.1.2 Basic concept of injection molding process	10
1.1.3 Microstructure of short-fiber-reinforced thermoplastics after injection molding	12
1.2 Thermo-mechanical behavior of short-fiber-reinforced thermoplastics	14
1.2.1 Behavior of thermoplastic polymers	14
1.2.2 Matrix fiber interface and fibers orientation measurement	17
1.3 Sources of uncertainty of composite mechanical behavior	19
1.3.1 Uncertainty quantification for composite materials from fibers to injection molded process	21
1.3.2 Modeling uncertainty of composite materials	25
1.3.3 Uncertainty propagation and uncertainty management	28
1.4 Description of existing tools in the laboratory	33
1.4.1 VE-VP-damage behavior model for SFRT	33
1.4.2 Realization and post-treatment of microtomographic scans	37
1.5 Conclusions	41
2 Analyses of SFRTs' microstructure and mechanical behavior	43

2.1	Effect of process parameters on fiber orientation and Young’s modulus of a PP-35GF	48
2.2	Natural fibers : variability of geometrical properties and orientation inside the composite	51
2.2.1	Natural fibers’ geometrical properties	52
2.2.2	Natural fibers’ orientation in injection-molded PP-30NF	54
2.3	Identification of the origins of composite’s Young modulus variability	57
2.4	Conclusion	63
3	Vibration response of PP-35GF and PP-30NF	65
3.1	Experimental study of PP-35GF and PP-30NF vibration response	67
3.1.1	Results of vibration study	68
3.1.2	Correlation between natural frequency and microstructure	71
3.2	Numerical study of vibration response of PP-35GF and PP-30NF	73
3.3	Conclusions	81
4	Mechanical response of SFRT under high-strain-rate loading	83
4.1	Characterization of mechanical behaviors	86
4.1.1	Viscoelastic parameters of matrix materials	86
4.1.2	Viscoplastic parameters of matrix materials	90
4.1.3	Fibers and matrix / fiber interface parameters	96
4.1.4	Model validation	103
4.2	Investigation of SFRT’s failure behavior	104
4.2.1	Failure of notched tensile specimens	106
4.2.2	SFRT’s failure behavior during bulge tests	111
4.3	Towards a failure criterion	115
4.4	Conclusion	124
	Conclusions and outlook	125
	Bibliography	131
	Abstract	147

List of Figures

1	Ashby diagram [1]	2
2	Tensile behavior of polypropylene matrix and 35% wt. short-glass-fiber-reinforced polypropylene tested at 10 mm/min	3
3	Fibers' classification [2]	3
1.1	Microstructure of a flax fiber [3]	10
1.2	Injection molding machine	11
1.3	Influence of weld line on the tensile strength of injected specimens [4]	12
1.4	Skin shell core structure	13
1.5	Temperature dependency for polyamide based semi-crystalline thermoplastic ©2016 Serban DA. Published in [5] under CC BY 3.0 license. Available from: http://dx.doi.org/10.5772/64563	15
1.6	(a) Maxwell model (b) Generalized Maxwell model	15
1.7	Schematic representation of a creep test and the response of a thermoplastic material	16
1.8	(a) untreated and (b) plasma-treated flax fibers [6]	18
1.9	Example of natural fiber cross-section [7]	19
1.10	Comparison between "by hand" measurement and measurement made with a software for (a) fibers' length and (b) fibers' aspect ratio [8]	20
1.11	Young's modulus of flax fiber [9]	22
1.12	Evolution of the fiber orientation through thickness. The bold triangles represent parts with thickness of 1.1 mm, the empty triangles for 1.7mm, the circles for 3mm and the squares for 5mm [10]	24
1.13	Tensile test of glass fiber reinforced polypropylene [11]	24
1.14	Example of fuzzy membership function [12]	27
1.15	Image and 5 mm x 5 mm x 2.5 mm volumes of PPNF and PPGF reconstructed with Fiji, at same rezolution, see table 1.4	38
1.16	Extraction of plans (here 10%wt. PPNF)	39
1.17	Example of natural fibers' porosities	40
1.18	Schematic representation of the post-treatment of each scan	41
2.1	Orientation of quasi-statique tensile specimens, the scanned zones are in red	46

2.2	Example of cutting at 0° of dynamic specimens	46
2.3	Specimens for the experimental vibration analysis	47
2.4	Dimensions of quasi-static and dynamic tensile specimens	47
2.5	Mean orientation measured for each configuration	48
2.6	Results of tensile test for the different configurations	49
2.7	Fibers geometrical properties distributions for specimens with a 30° cutting angle; dashed lines represent the log-normal distribution used	52
2.8	Effect of variable parameters on fibers' axial stress	53
2.9	Fibers' orientation distributions for specimens with a 30° cutting angle	54
2.10	Skin-shell-core structure through thickness of specimens (left is the PPGF and right is the PPNF)	55
2.11	Fibers' orientation of each subvolume of barrels n°3 and N°7	56
2.12	Mean orientation for all subvolume of each specimen	57
2.13	Three tensile tests for the PPGF matrix and five tensile tests for the PPNF matrix all tested at $5.5 \cdot 10^{-3} \text{ s}^{-1}$	58
2.14	Tensile behavior of PPGF	59
2.15	Tensile tests for the PPNF with same cutting angle	60
2.16	Results of tensile test at different cutting angles for both materials	62
3.1	Experimental set-up (a) for the plates and (b) for the barrels	67
3.2	First natural frequency of whole plates (injection or opposite side refers to clamping edge)	68
3.3	Origin of the variabilities measured for both materials	71
3.4	Mean fibers' orientation versus first natural frequency	72
3.5	Technical data sheet of (a) PPGF (b) PPNF	73
3.6	Mesh used for the numerical simulations	74
3.7	Moldex3D rheological mesh	76
3.8	Mesh of the whole plate with barrels' location	77
3.9	Histogram of fibers' orientation for the subvolume 1	78
3.10	Schematic representation of the time cost of each method compared to their precision	81
4.1	Tensile behavior of PPGF and PPNF	84
4.2	Results of the DMA for the matrix of PPNF	89
4.3	Results of the DMA for the matrix of PPGF	89
4.4	Tensile specimens geometry	91
4.5	Mechanical behavior of both matrices measured by DIC	92
4.6	Behavior laws obtained with the $SE\dot{E}$ method for the matrix of the PPGF	93

4.7	Results of compression tests for both matrices	93
4.8	Stress-strain curve for PPNF matrix during cyclic tests	94
4.9	Evolution of damage in function of cumulated viscoplastic strain	95
4.10	Correlation between numerical and experimental results for both matrix; straight lines represent experimental values and dashed lines represent numerical values	96
4.11	PPNF fibers' discretized orientation distributions	97
4.12	Nominal axial stress and strain results of PPGF tensile tests	98
4.13	Nominal axial stress and strain results of PPNF tensile tests	99
4.14	Comparison between experimental results and numerical results	100
4.15	Impact of the variation of a and b on δ	101
4.16	Evolution of δ according to two couple of a and b	102
4.17	Comparison of the mechanical behavior of the PPNF at 100 mm/s between different values of a and b	102
4.18	Correlation between experimental and numerical results for PPNF; straight lines are experimental values and dashed-lines are numerical values	103
4.19	Correlation between experimental and numerical results for PPGF; straight lines are experimental values and dashed-lines are numerical values	104
4.20	Percentage of use of various failure criteria in industrial context [13]	105
4.21	Cutting plan of notched tensile specimens	107
4.22	Noise measurement with the DIC	108
4.23	Localization of the mapping of ε_{yy} on a notched specimen	108
4.24	Mapping of ε_{yy} at the pre-crack step and evolution of ε_{yy} during tensile tests; numbers refers to the tensile specimen position in Figure 4.21	109
4.25	Boxplot of PPNF axial strain at break for notched specimens	110
4.26	Experimental set-up for the bulge tests	111
4.27	Plan of the perforated plates and schematic representation of fibers orientation (blue arrows) with respect to load direction (red arrows)	112
4.28	Load vs punch displacement during bulge tests for both materials	112
4.29	Example of order of appearance of cracks of one plate for both materials	113
4.30	Example of PPNF crack	115
4.31	Mesh of notched tensile specimen	117
4.32	Comparison between numerical and experimental results	117
4.33	Sectional view of PPNF numerical axial strain	118
4.34	Identification of time step at break initiation according to experimental axial strain	118
4.35	Identification of τ_{LF} at break	119
4.36	Mesh of the plate for numerical bulge test	120
4.37	Axial displacement during numerical bulge test	121

4.38	Evolution of D vs punch displacement for the 4 sides	121
4.39	Evolution of τ_{LF} vs punch displacement for the 4 sides	122
4.40	Evolution of τ_{LF} vs punch displacement for east and south sides	122
4.41	Schematic representation of the formation of a weld line	129

List of Tables

1.1	Summary of the different sources of uncertainty enumerated in subsection 1.3.1 .	25
1.2	Summary of the different way to model the uncertainty enumerated in sub-section 1.3.2	28
1.3	Summary of the different way to propagate and to manage the uncertainty enumerated in sub-section 1.3.3	31
1.4	Parameters used during the micro-computed tomography	38
2.1	Parameters used during the injection molded process for a) PPNF and b) PPGF	45
2.2	Young' modulus calculated for each different injection molding configurations . .	50
2.3	Effect of variable parameters on fibers orientation and composites' Young modulus	51
2.4	Young' moduli calculated for each matrix tensile test	58
2.5	Young' modulus calculated for each PPGF tensile test	59
2.6	Young' modulus calculated for each PPNF tensile test	60
2.7	Young' modulus calculated for each PPNF tensile test with different cutting angles	61
2.8	Young' modulus calculated for each PPGF tensile test with different cutting angles	61
3.1	Measurement uncertainty for the three first natural frequency of PPNF specimens (specimen numbers refer to cutting locations indicated in Figure 2.3) . . .	69
3.2	First natural frequencies (in Hertz) obtained for barrels of PPNF and PPGF (specimen numbers refer to cutting locations indicated in Figure 2.3)	70
3.3	Min and max first natural frequencies obtained during experimental investigation and first natural frequency measured with numerical simulations	74
3.4	Comparison between method 2 results and experimental first natural frequency .	75
3.5	First natural frequencies obtained for the simulated barrels	77
3.6	Relative error calculated for the method 2 compared to values obtained during experimentations with clamping on injection and opposite side	78
3.7	Young's modulus calculated for each sub-volume for barrel 1	79
3.8	First natural frequency for PP-30NF barrel number 1, comparison between numerical and experimental values	79
3.9	Homogeneous method mixed VUMAT method	80

4.1	Frequency used during the DMA	86
4.2	Identified viscoelastic parameters for both matrices	88
4.3	Strain rate and camera frame rate	90
4.4	Viscoplastic parameters	93
4.5	Debonding parameters for both materials	101
4.6	Mean value of axial strain, ε_{yy} , at failure initiation in surface for both materials and with a 0° cutting angle	110
4.7	Crack order for both materials obtained during bulge tests; N = north, S = south, E = east, W = west and X is for none	114
4.8	Experimental min and max values and mean value of axial strain at break for the three cutting angles	118
4.9	Debonded fibers length ratio at break for the three cutting angles (with a=0.05 and b=2)	119
4.10	Min., max. and mean values of D for the 3 cutting angles	119
4.11	Numerical punch displacement according to values of τ_{LF}	123
4.12	Experimental punch displacement at first crack initiation in surface	123
4.13	Crack order for PPGF with welding line	129
4.14	Crack order for PPNF with welding line	130

General Introduction

In today's society, polymer materials are used for a very wide range of applications, from toothbrushes to bridges. The main advantages of this type of material are a low fabrication cost and high strength to density ratio. Polymers are large molecules resulting from the assembly of repeated units of monomers. In case of different types of monomers, it is talked about co-polymers. The conformation of polymeric chains is defined by the order of succession of different monomers (in case of copolymers) and/or by spatial configuration of monomers all along the chains. Polymers are divided into three distinct groups: thermoplastics, thermosets and elastomers, depending on chain organization, which are characterized by different mechanical properties:

- **Thermoplastics** can be split into two groups: amorphous and semi-crystallin. Amorphous thermoplastics' structure is randomly organized making them easily thermoformed. On the contrary, in addition to amorphous phase, semi-crystallin thermoplastics also present a phase with ordered structure giving them higher mechanical resistance than amorphous thermoplastics. Thanks to their particular microstructure, both types of thermoplastics are reformable upon successive heating and cooling phases, giving them the advantage of being recyclable;
- **Thermosets**' structure is generally amorphous but characterized by crosslinking forming three-dimensional networks, which confers them higher strength and rigidity than thermoplastics. Contrary to thermoplastics, once thermosets are cooled the microstructure is fixed and cannot change, even when re-subjected to heat;
- **Elastomers**' structure is also characterized by crosslinking forming three-dimensional networks but with weak intermolecular forces. This structure gives elastomers hyperelastic properties, characterized by a high level of elastic strain before failure.

Since the 1960s, the automotive industry uses thermoplastic parts for both interior and exterior of vehicles in replacement of more and more metal parts. Indeed, their lightweight compared to metal (Figure1) allows a reduction of mass of vehicles and therefore a decrease of their energy consumption, and of greenhouse gaz emission in case of thermal engines. In

addition, the capacity of thermoplastics to be heated up to a viscous fluid state without degradation allows the easy manufacturing of parts of any shape and size (from oil filler caps to oil pan) by injection molding.

One of the main disadvantages of thermoplastics is that they have low mechanical properties compared to metallic materials (Young modulus of 1.5 GPa for polypropylene against ~ 210 GPa for steel, for instance). In addition to their weak mechanical properties, they also have a complex behavior. Indeed, thermoplastic materials are characterized by viscoelastic and viscoplastic behavior, plastic flow, hydrostatic pressure dependency and strain-rate dependency (details can be found in 1.2.1).

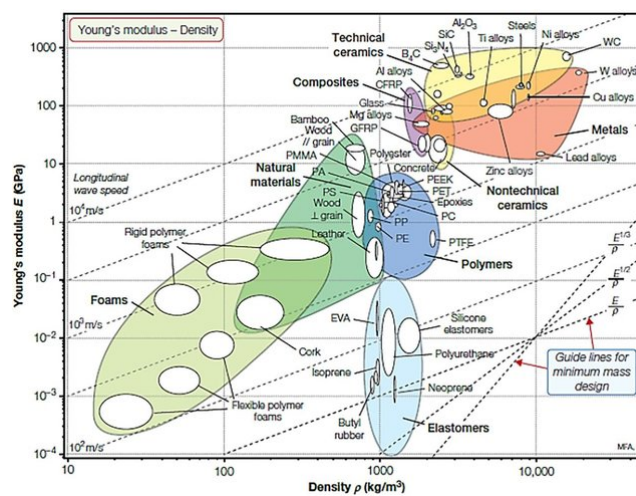


FIGURE 1: Ashby diagram [1]

In order to improve the "weak" properties of thermoplastics, reinforcements are added. The reinforcements used can be particles (talc, carbon, ...), fibers (short, long, natural, ...) or nanotubes (carbon, halloysite, ...) and are characterized by a higher Young modulus than the matrices in which they are embedded. In the case of fiber reinforced thermoplastics, short fibers and long fibers (i.e. continuous or almost fibers) are to be distinguished. Long-fibers-reinforced materials generally offer the highest mechanical properties but are not suitable for injection molding process and mass production. Therefore, apart from a few exceptions, short fibers reinforced thermoplastics are used in the automotive sector, with a fiber length generally in the range of tenths of μm to 1mm, after injection molding. Today, mineral fibers are the most used. They present simple geometries with low variability, which allows to master their mechanical response, and high Young modulus compared to polymeric matrices (e.g. about ~ 76 GPa for short glass fibers).

The mechanical behavior of Short-Fiber-Reinforced Thermoplastics (SFRT) is complex. First, it is logically governed by fiber content but also fiber aspect ratio and local orientation with respect to loading direction, in particular. Indeed, the load applied to the composite is

transferred from the matrix to the fibers by a shear-transfer process at fiber/matrix interface. The efficiency of fibers is maximized when the loading direction is oriented along fibers' axis. More globally, the addition of short fibers leads to a complexification of the microstructure whose impact on SFRT mechanical response must be considered, in addition to specificities of thermoplastic matrix behavior. Thus, adding fibers to thermoplastics highly improves their mechanical behavior but also makes it anisotropic (Figure 2). The anisotropic behavior appears because fibers' orientation is induced by melt flow and vary across parts during the injection molding. The latter phenomenon is illustrated by Figure 2. When increasing the angle between load direction and fibers orientation, the composite loses rigidity but in return becomes less brittle.

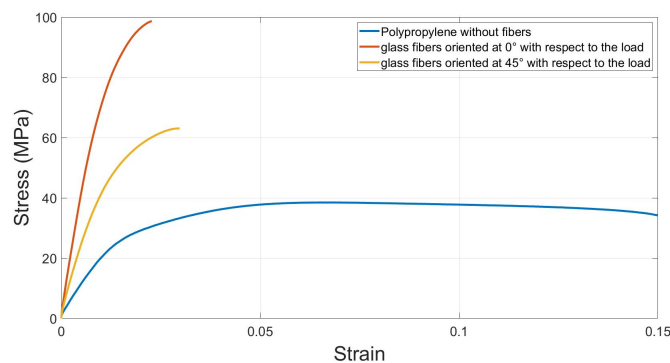


FIGURE 2: Tensile behavior of polypropylene matrix and 35% wt. short-glass-fiber-reinforced polypropylene tested at 10 mm/min

In today's society, governments and the European parliament encourage industries to increase their use of reusable or recyclable materials ([14]). It is important to note that mineral fibers require a lot of energy to be produced and that these fibers are not easily recyclable. Therefore, in order to increase the use of environmentally friendly materials, natural fibers (mostly plant fibers) are studied to replace mineral fibers. Many types of natural fibers can be considered (Figure 3) but they are all complex materials defined by a complex structure.

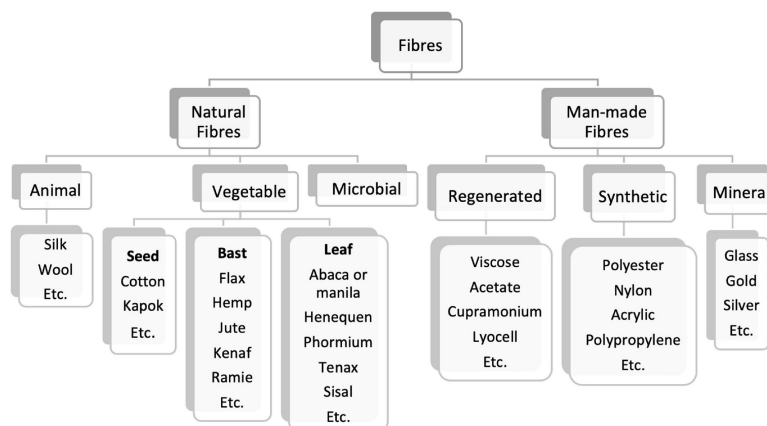


FIGURE 3: Fibers' classification [2]

This type of fibers present variabilities at different layers which, once cumulated, generate a variability of technical fibers geometrical properties (length, shape and area of cross-section...). The mechanical behavior of short-natural-fibers-reinforced composites is directly impacted by the high variability related to plant fibers and therefore becomes difficult to predict.

It is within this context that the automotive supplier Novares seeks to improve the precision of its numerical simulations in order to improve the confidence in the use of vegetable fibers. For instance, to simulate the vibration response of SFRT, Novares' protocol is to remain careful. To do so, pessimistic Young's modulus are used, leading to under-estimated mechanical results. Therefore, in order to meet customer requirements (eigenfrequencies, weight of parts...), nerves may be added or parts oversized, unnecessarily.

In this PhD thesis work, two industrial thermoplastics reinforced with short-glass-fibers or short-natural-fibers are studied. The aim of this research is to better understand the variability/uncertainties of such materials by analyzing the relations between the microstructure and the mechanical behavior for two situations, a vibration analysis and an impact behavior. More details can be found in the following outlines.

Outlines

In order to give an answer to the objectives presented previously, this work is structured in five chapters.

Chapter 1 is divided into two parts. The first part introduces basic knowledges related to the injection molding process and SFRT's microstructure after injection molding. The structure of natural fibers is studied in order to better understand the difficulties associated with their use. General aspects of the complex mechanical behavior of SFRT are studied. Finally, the inclusion of sources of variability for the prediction of composite mechanical behavior is reviewed. The second part of this chapter quickly describes the model used to simulate SFRT's behavior and then the realization of the microtomographic scans and their post-processing.

Chapter 2 deals with the origin of SFRT macroscopic behavior variability. The microstructure of both materials is therefore studied using microcomputed tomography. First, the impact of variable injection molding process parameters on short glass fibers orientation is analysed and then linked to SFRT' macroscopic behavior. In the second part, the variability of natural fibers geometrical properties as well as their orientation are studied. Finally, the origin of Young's modulus variability is linked to a growing uncertainty level.

Chapter 3 is related to the study of variable SFRT vibration behavior. In the first part, experimental investigations are performed to quantify the vibration response of SFRT in correlation with microstructure properties of natural-fiber-reinforced polypropylene. The second part confronts the experimental results with numerical simulations. The first simulations are made using the industrial procedure, then, by increasing the amount of variability taken into account, the accuracy of the simulations is increased.

In **Chapter 4**, the failure behavior of SFRT is under investigation. Both materials are first characterized in order to numerically model their mechanical behavior. Then, tensile tests are performed on notched tensile specimens to set a failure criterion based on experimental observations and damage behaviors. Finally, bulge tests are performed on perforated plates and numerical simulations are done in order to assess the relevancy of previously defined failure criterion.

Chapter 5 is the concluding chapter of this thesis. This chapter also gives perspectives to improve the present work.

Chapter 1

State of the art

Contents

1.1	Investigation of short-fiber-reinforced thermoplastics' microstructure	8
1.1.1	Short fibers	8
1.1.2	Basic concept of injection molding process	10
1.1.3	Microstructure of short-fiber-reinforced thermoplastics after injection molding	12
1.2	Thermo-mechanical behavior of short-fiber-reinforced thermoplastics	14
1.2.1	Behavior of thermoplastic polymers	14
1.2.2	Matrix fiber interface and fibers orientation measurement	17
1.3	Sources of uncertainty of composite mechanical behavior	19
1.3.1	Uncertainty quantification for composite materials from fibers to injection molded process	21
1.3.2	Modeling uncertainty of composite materials	25
1.3.3	Uncertainty propagation and uncertainty management	28
1.4	Description of existing tools in the laboratory	33
1.4.1	VE-VP-damage behavior model for SFRT	33
1.4.2	Realization and post-treatment of microtomographic scans	37
1.5	Conclusions	41

This work was already published in the article [15].

Injection-molded short-fiber-reinforced thermoplastics (SFRT) are widely used in today's industry, especially with short mineral fibers. Nevertheless, their mechanical behavior is difficult to predict, in particular because of thermoplastics' specificities and strong anisotropy induced by complex fibers' distributions of orientation. More recently, environmental concerns oblige industrials to switch to more eco-friendly materials [16]. Since mid of 1970s [17], researchers are interested in the mechanical properties of plant fibers aiming at using them instead of mineral fibers in injection-molded parts. However, the intrinsic variability of plant fibers' properties leads to an even more complex behavior than with mineral fibers and also increases the uncertainty for behavior prediction of SFRT materials.

The aim of this Chapter is to do a state of the art about the characterization of uncertainties of injection molded short(-plant)-fiber-reinforced thermoplastics behavior, focusing on variability induced by both injection-molded process and natural variability of plant fibers properties. To achieve this goal, it is important to understand the microstructure differences between short-mineral-fibers and short-natural-fibers-reinforced thermoplastics processed by injection molding. Then, the complex mechanical behavior of SFRT is exposed. The third part deals with uncertainty quantification, modeling and propagation for prediction of SFRT mechanical behavior. Finally the last two sections describe the existing tools in LAMIIH that will be used during this PhD thesis work for numerical prediction of SFRT behavior (Abaqus VUMAT) and microstructure analysis with microcomputed tomography (μ CT).

1.1 Investigation of short-fiber-reinforced thermoplastics' microstructure

As explained, SFRT are complex materials. Their mechanical behavior is influenced by several factors from their microstructure to their manufacturing process. The following subsection discusses the specificities related to short fibers.

1.1.1 Short fibers

Mineral fibers are part of the man-made fibers family. Their shape can be described using a cylindrical representation with a ratio length over diameter (e.g. aspect ratio, L/D) much

greater than one. In general, their length is lower than one millimeter in injection molded short-fiber-reinforced composites and their behavior is assumed linear elastic and isotropic (sometimes orthotropic). One of the main advantages of these man-made fibers is their mastered geometrical properties. The most commonly used mineral fibers are glass and carbon fibers.

Compared to mineral fibers, natural fibers have relatively low cost, low density, are issued from renewable sources and are biodegradable [16]. While mineral fibers generally have simple and repeatable properties, natural fibers are characterized by variable properties. For example, contrary to glass fibers, natural fibers' geometrical parameters vary widely between the same batch and from one batch to another. This variability is directly induced by the complex structure of natural fibers (Figure 1.1). In fact, this structure is divided into different scales with variable morphological parameters. At nanoscopic scale, cell walls are made up with lamellae. These lamellae mainly consist of cellulose fibrils embedded in hemicellulose and pectin. Their number and their orientation angle are both important nanoscopic parameters for the mechanical behavior of fibers [18]. For example, Page et al. [19] have shown the importance of the angle between microfibrils and the stem on the mechanical properties of fibers. The reorientation of these microfibrils in tension is one of the causes of the non-linear behavior in tension of natural fibers. This complex organization makes natural fibers' mechanical behavior no longer linear elastic, as mineral fibers, but viscoelastic [20–22].

The next scale is composed of primary and secondary cell wall. The primary cell wall (located on the outskirts) is thin and mainly composed by pectin. The secondary cell wall is composed by cellulose, hemicellulose and lignin and is divided into three sublayers called S1, S2 and S3. Among them, the sublayer S2 is the larger (around 80% of cell wall thickness) and is the key point of mechanical strength of natural fibers. This sublayer is composed of the previous microfibrils [18].

Elementary fibers are glued together by pectic cement to form bundles (or technical fibers) to form technical fibers. Thus, the number of elementary fibers per technical fibers is variable, leading to variable technical fibers' section, in particular. Finally, fibers bundles are found in the stem of plants in variable number and with variable dimensions.

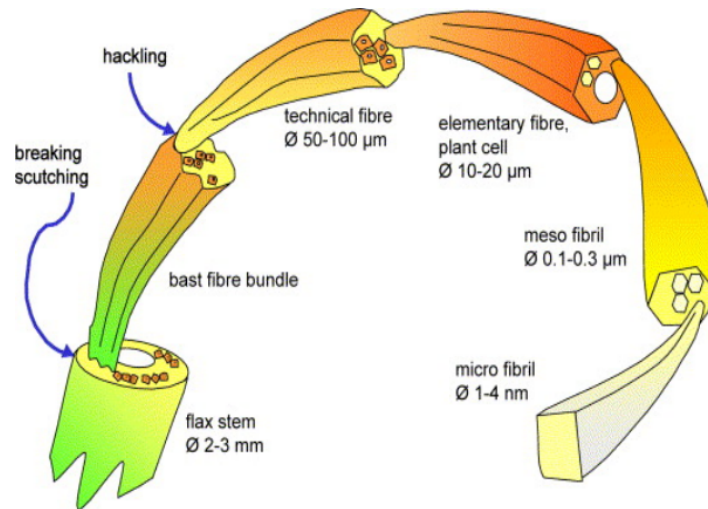


FIGURE 1.1: Microstructure of a flax fiber [3]

It has been seen that fibers' morphological properties, in particular natural fibers, may present significant variability. These morphological variabilities impact natural fibers mechanical properties. For example, Placet et al. [23] have shown the impact of fibers diameters and lumen size of flax fibers Young modulus. It has been seen that fibers Young modulus decreases while lumen size increases. According to Richely et al. [24], the value of flax fibers Young modulus may vary from 45 to 70 MPa because of variable biochemical composition and/or morphological variabilities. Thus, at the composite scale, microstructural fibers' organisation is an additional source of variability of mechanical behavior and especially in the case of natural fibers. However, this variability is strongly dependent on the manufacturing process, here injection molding, as presented in the following section.

1.1.2 Basic concept of injection molding process

The injection molding process is a reversible process which allows manufacturing thermoplastic parts of any shape, possible at high production rate, that makes this process particularly appealing for automotive industry. Figure 1.2 is a schematic representation of the injection molding machine.

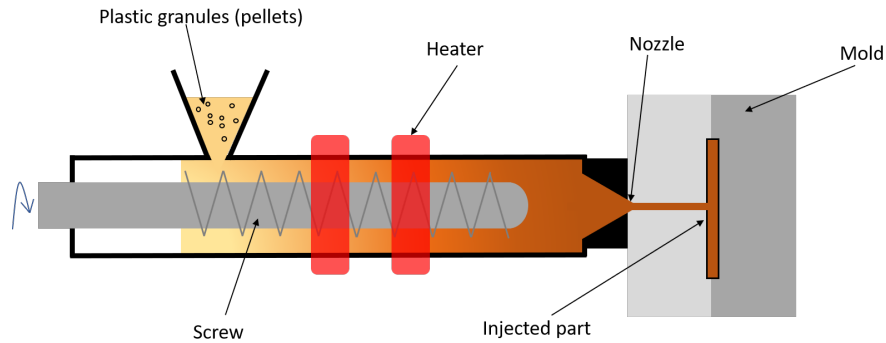


FIGURE 1.2: Injection molding machine

The injection process is divided into four main phases [25] :

1) The material granules (pellets) are first placed in a hopper above the injection machine. In the case of fiber-reinforced materials, the granules are composed of polymeric matrix and fibers. The granules are heated up to polymer melt temperature and homogenized all along their progress over the rotating screw. The mold, which is closed before the injection, is also heated up to a given temperature;

2) Once the material reaches the end of the screw, the injection can start. The material is injected under pressure into the mold through a gate due to the transverse displacement of the screw. During the filling, the forced flow implies a complex organization of fibers in the material;

3) When the mold is almost filled, a small quantity of melt material continues to be injected to increase the pressure in the mold cavity. A high pressure is then also maintained on both faces of the mold: this is the packing stage. The aim of this stage is to avoid warpage, by homogenizing polymer shrinkage upon cooling in the part;

4) The final stage consists of cooling the part while maintaining the pressure on both faces of the mold. When the freezing point is attained, the mold is opened and the part is ejected.

The link between the mold entrance(s) and the nozzle is made with pipes and different kinds of gates. For the injection of the same part, it is possible to change the number of gates [26]. By increasing the number of gates, several melt flows are created and may eventually encounter each other. As a consequence, the multiple-gate injection process will lead to the apparition of weld lines at the junctions of the flows stemmed from different gates [27]. Weld lines are also encountered if the flow arises from a unique gate but is split in different arms, when it encounters an obstacle in the mold cavity and is then reunited, e.g. [28]. Weld lines may have detrimental effects on the aesthetic of parts but also on their mechanical properties. For example, Oh et

al. [4] have analyzed the impact of a weld line in tensile specimen on properties of a short-glass-fibers composite. To do that, tensile specimens were injection-molded using a single-gate (no weld line) or two-gates process (weld line at the center of the specimen, perpendicular to the loading axis). The Figure 1.3 shows composite tensile strength at different fiber contents with and without weld line. In the case of one-gate process (no weld line), one can notice the increase of the tensile strength while increasing the fiber content. Whereas in the case of two-gates process, the tensile strength is the same even if the fiber content is increased. This suggests that weld line weakens the parts regardless of the fiber content. Moreover, the weld line seems to drastically weaken the PPGF which presents mechanical properties even lower than those of the unreinforced matrix.

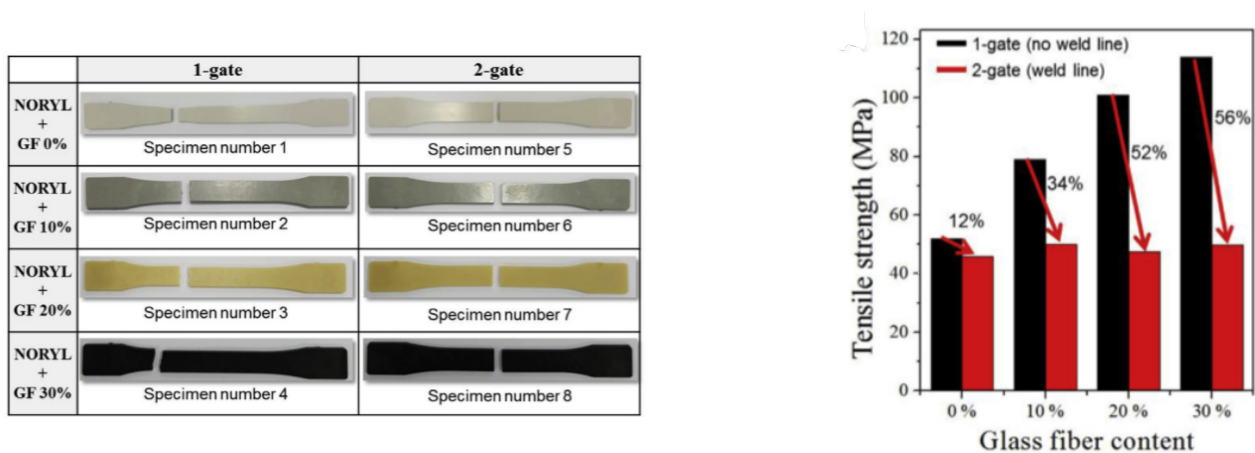


FIGURE 1.3: Influence of weld line on the tensile strength of injected specimens [4]

The presence of weld lines is an aspect of the injection molding process. More globally, the organisation of the microstructure of SFRT strongly depends on injection-molding process parameters, as highlighted in the next paragraph.

1.1.3 Microstructure of short-fiber-reinforced thermoplastics after injection molding

After injection molding, SFRT show very complex microstructure, in particular because of the high discrepancy of fiber orientation arising from the forced viscous flow. This discrepancy is governed by material properties (e.g. fiber fraction and geometry), process parameters (injection speed, injection temperature, ...) and part shape.

Yet, mechanical properties of the injected part highly depend on the organization of the microstructure. It is therefore essential to understand the link between parameters of injection process and the microstructure, for given material and part shape, to be able to optimize the process in order to reach targeted mechanical properties. Actually, injection molding process

parameters highly impact the organization of fibers in composite microstructure because fibers are reoriented in the mold cavity following a velocity vector induced by the injected flow. Two types of flow have a significant impact on the orientation of the fibers [29]. When the material is injected within divergent or convergent geometry into the part, a stretching flow happens and the fibers tend to be perpendicular to the flow. Then, as the material is going through the part, a shear flow happens. This flow allows fibers to reorient themselves parallelly to the injection flow direction. The effect of the shear flow decreases with the distance between the fibers and the mold walls. It means that fibers at the center of the part (core layer) are less affected by the shear flow and stay therefore mainly oriented transversaly to the injection flow direction.

In addition to those two flows, fountain effect must also be considered. This effect was first noticed with mercury in a glass tube [30] and is characterized by a shear flow induced by the displacement of the flow front between solid walls [31, 32]. The viscous flow is then projected from the central plane of the mold cavity to the walls with a significant impact on the orientation of the fibers [33, 34]. Indeed, the cold temperature of the mold, compared to that of the flow, together with fountain effect are responsible for the creation of a thin layer near the mold walls where fibers are randomly oriented (skin areas).

These mechanisms lead to a particularity of SFRT: the “skin-shell-core” structure (Figure 1.4), which traduces a strong heterogeneity of fiber orientation through a part thickness. A lot of researchers have described this structure [35–41]. The main difference is the number of layers that are considered. For Kenig et al. [38] there are nine layers placed symmetrically, while for Bay and Tucker [39, 40] the number of layers is seven. Yet, usually, for injection of thin parts between parallel walls, the most encountered description is a five- (or three-) layers structure, also called "skin-shell-core structure" [36]. In the case of a three-layers structure, the skin layer is not considered because of its negligible size relatively to part thickness.

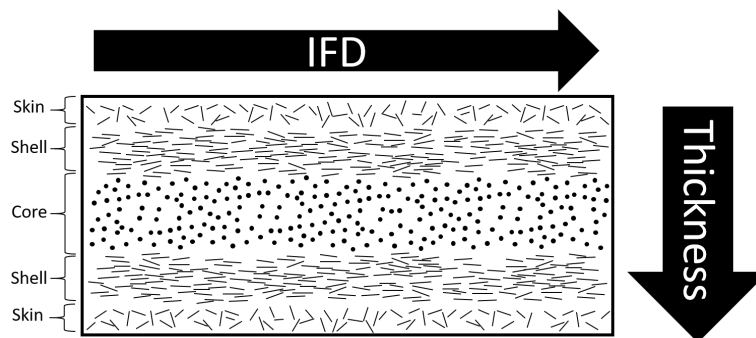


FIGURE 1.4: Skin shell core structure

As mentioned before, the fountain effect and the process parameters have a huge impact on fiber orientation. To summarize, the fountain effect projects the melted blend against the

relatively cold mold walls where fibers are quickly frozen within the polymer and adopt more or less random orientation in the skin layers. The shell (or shear) layers are composed of fibers mainly oriented parallel to the flow velocity vector, due to the shear effect. Finally, a nearly null shear effect in the middle of the part thickness and the previous stretching flow will make the fibers oriented perpendicular to the velocity vector, in the core layer. Concerning the process parameters, the impact of the mold temperature, the melt temperature and the injection speed are further discussed in section 1.3.1.

This kind of microstructure heterogeneity, directly stemming from the injection molding process, is common to all SFRT, whatever the nature of the fibers. This particular microstructure coupled with the specificities of thermoplastics mechanical behavior makes the SFRT's mechanical behavior even more complex as seen in the following section.

1.2 Thermo-mechanical behavior of short-fiber-reinforced thermoplastics

In order to understand all the specificities of SFRT, the behavior of thermoplastic matrices is introduced in Section 1.2.1. Then, the fibers' behavior studied previously is governed by their orientation within the composite, therefore, their orientation must be taken into account. Thus, Section 1.2.2 discusses about the interface between fibers and matrix and also about the measurement of fibers orientation inside composites.

1.2.1 Behavior of thermoplastic polymers

The macroscopic behavior of thermoplastics results from the behavior of the amorphous phase and, if present, of the crystalline phase. As a consequence, the crystallinity ratio governs the behavior of thermoplastic. The behavior of thermoplastic polymers highly depends on temperature [5]. Above melt temperature, thermoplastics behave as viscous liquids. Upon cooling, different transitions are characterized by specific temperatures. The crystalline phase thus appears below crystallization temperature, when chains begins to organize themselves. Dealing with the amorphous phase, the glass transition temperature T_g delimits the rubbery domain (at high temperature) and the glassy domain (below T_g). The rubbery domain is characterized by a low Young's modulus and a high elasticity whereas in the glassy domain the amorphous phase is more rigid and more brittle. Also, thermoplastics' behaviors present temperature dependency within rubbery or glassy domain. Serban et al. [5] have shown the temperature

dependency of polyamide-based semi-crystalline thermoplastic polymer. In Figure 1.5, it can be seen that increasing the temperature reduces the tensile strength of polyamide drastically (from 53MPa at -25°C to 18MPa at 50°C).

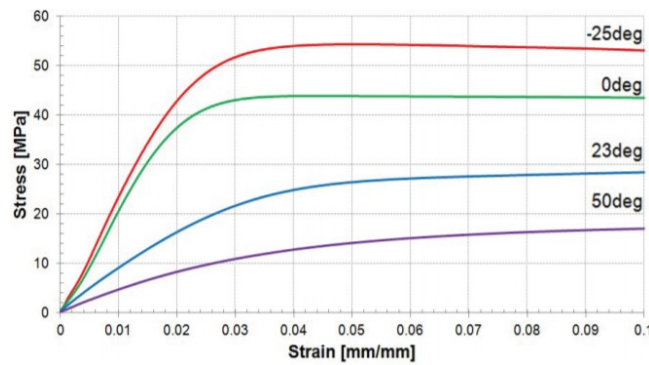


FIGURE 1.5: Temperature dependency for polyamide based semi-crystalline thermoplastic ©2016 Serban DA. Published in [5] under CC BY 3.0 license. Available from: <http://dx.doi.org/10.5772/64563>.

In the early strain stages, thermoplastics show a viscoelastic (VE) behavior, i.e. elastic behavior is time and strain-rate sensitive. Thus, during a tensile test, the apparent rigidity of a VE thermoplastic increases with the strain rate. If the plastic threshold is not reached, the tested specimen retrieves its initial form after more or less long time. It indicates that reversible strain does not vanish instantaneously, contrary to case of elastic behavior, but after a given duration, specific to each thermoplastic. The VE behavior can be represented using rheological models constituted of spring (elastic) and damper (viscous) elements. Several VE models exist like Maxwell model, Kelvin-Voigt model, Burgers model, etc [42]. The Maxwell model uses a viscous damper and an elastic spring connected in series whereas the generalized Maxwell model puts in parallel n Maxwell elements and an elastic spring (see Fig. 1.6).

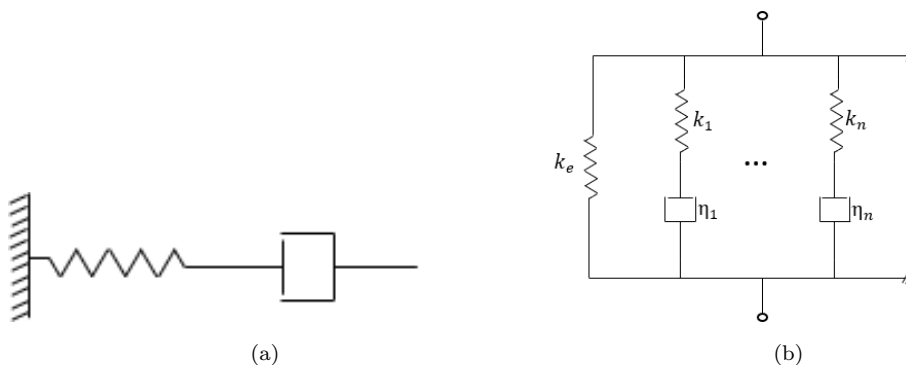


FIGURE 1.6: (a) Maxwell model (b) Generalized Maxwell model

In this model, k_e represent the infinite modulus, k_i represent the moduli and η_i the viscosities of each Maxwell element. Each viscous damper has its own characteristic time for strain dissipation. Therefore, the number of Maxwell elements will influence the kinetics of

recovery of viscoelastic strain. Accuracy of VE model can be assessed in particular for creep and relaxation tests. During creep tests the material is exposed to a constant stress and the strain response is measured over time. The Figure 1.7 shows schematically the differences when using Maxwell model (red dashed-line) or Generalized Maxwell model with a finite number of Maxwell elements (black line). As expected, a unique Maxwell element cannot give an accurate prediction of viscoelastic strain / recovery and therefore of creep behavior.

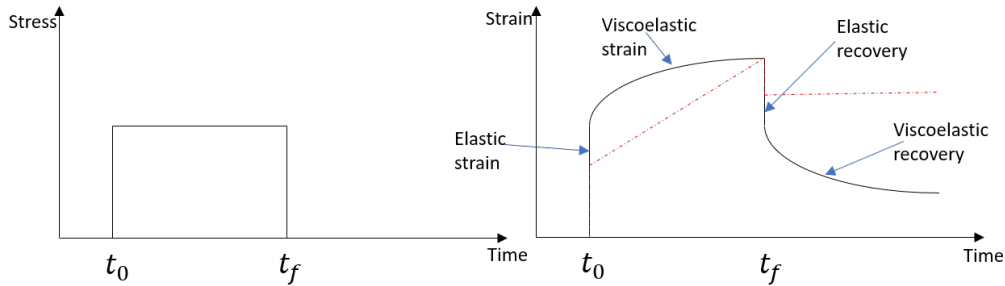


FIGURE 1.7: Schematic representation of a creep test and the response of a thermoplastic material

The behavior of thermoplastic materials is also sensitive to hydrostatic pressure [43–45]. Indeed, those materials show different responses in tension and in compression, in particular. As a consequence, the isotropic von Mises plasticity criterion is irrelevant to describe the yield surface of thermoplastics since it does not consider this sensitivity. On the contrary, the Raghava yield surface [46, 47], for example, takes the influence of hydrostatic pressure into account by involving the ratio between the initial yield stress in compression and in tension in its expression. Another important aspect of thermoplastics' behavior is the strain-rate dependency of plastic flow (i.e. viscoplasticity). For instance, Zhang et al. [48, 49] have studied the rate dependency of polyethylene (PE) by conducting several tensile tests at constant strain rate. Young modulus and strength of PE were shown to increase with strain rate.

In addition, thermoplastics generally show a strongly non-linear hardening behavior. This hardening behavior depends on microstructural factor but also environmental factors. At microstructural scale, the molecules align themselves in the loading direction thus increasing the stiffness and the strength of the materials. For the environmental factors, the temperature or even the loading conditions may impact the hardening behavior of thermoplastic materials. In addition, several studies [50–53] have shown the non-isochoric evolution of the plastic flow. For instance, with video-controlled tests, G'sell et al. have observed the volumetric strain for polyethylene terephthalate [51] and quantified the volumetric strain for polypropylene [50].

In this thesis, a model developed at LAMIH is used to model all the specificities of thermoplastics' behavior. The model is briefly presented in Section 1.4.1.

1.2.2 Matrix fiber interface and fibers orientation measurement

Mechanical behavior of short-fiber reinforced thermoplastics depends on the behavior of the two phases (thermoplastic matrix and embedded fibers) but also on the interaction between both phases, i.e. adhesion and behavior of fiber/matrix interface. The complex mechanical behavior of thermoplastic matrix was briefly described in Section 1.2.1. Naturally, all its specificities are also encountered in reinforced thermoplastics. For example, Mouhmid et al. [54] have studied the strain-rate sensitivity of glass fibers reinforced PA6.6. The authors have shown the same trend as the matrix without reinforcement, i.e. an increase of composite stress level with strain rate (see section 2.1). The case of high strain rate has been studied by Kim et al. [55]. Hopkinson pressure bars were used for the testing of glass fiber reinforced polypropylene. The temperature dependency has also been studied [5, 56]. Thanks to Eftekhari and Fatemi [56], one can see the same trend for the glass fiber reinforced thermoplastic composite than for the neat thermoplastic. Indeed, for both cases, the materials become softer with the increase of temperature and more brittle when the temperature decreases. Also, the impact of the variability of fibers on the reinforced material mechanical properties has been numerically studied by Notta-Cuvier et al. [57] for the case of a short-flax-fiber reinforced polypropylene.

As seen in Section 1.1.1, fibers have their own behavior that naturally impacts the behavior of the reinforced material. Adding fibers allows to transfer the load initially born by the matrix to the fibers by shear transfer. A lot of models, for instance shear-lag model initially developed by Bowyer and Bader [58], consider the interfacial shear strength (IFSS) to quantify the load transmission at fiber/matrix interface and so on to compute the average stress in a fiber. The IFSS obviously depends on the nature of both fibers and matrix. For instance, Yan and Cao [59] have analyzed the differences in microstructure between glass fiber reinforced polypropylene (GF/PP) and carbon fiber reinforced polypropylene (CF/PP). In this study, the IFSS values have been calculated and linked to fiber's length. It appears that IFSS increases while length decreases. This result agrees with the study of Fu and Lauke [60], the composite strength increases with fiber's length. In the case of natural fibers, the hydrophobicity of the thermoplastic matrix and the hydrophilicity of fibers lead to a poor interfacial adhesion. In order to improve the quality of the interface, chemical or physical treatments can be used. Enciso et al. [6] have studied the impact of plasma treatment on the interface between flax fiber and polyethylene matrix, Fig. 1.8.

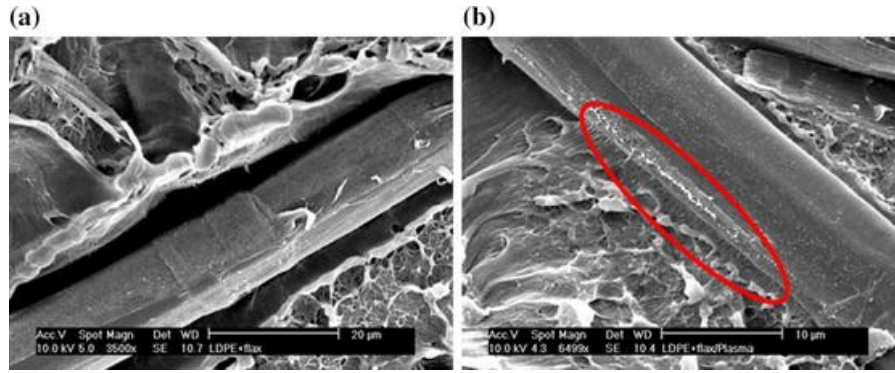


FIGURE 1.8: (a) untreated and (b) plasma-treated flax fibers [6]

They demonstrated that the adhesion was improved with plasma treatment, thus improving the mechanical properties of the composite [6] (e.g. increase of tensile strength). Other treatments have been studied, for example the use of coupling agents like graphene oxide and silane [61]. It is possible to use Maleic Anhydride (MA) grafting to enhance the interface between natural fibers and polypropylene matrix [62]. This treatment is different from other chemical treatments because it affects both fiber surface and matrix. Mishra et al. [63] have shown the increase of mechanical properties (Young's modulus, flexural modulus...) of short-plant-fiber (banana fiber, hemp fiber and sisal fiber) reinforced PP treated with MA (about +13% for tensile strength value).

Fibers load bearing capability is directly correlated with their orientation with respect to macroscopic loading direction, with a maximum when fibers are aligned with loading direction. Therefore, measuring fibers' orientation inside composite is an important step. There are several ways to measure the orientation of the fibers based on 2D or 3D analyses. The 2D observations can be done via Scanning Electron Microscopy (SEM) or optical microscopy. Special precautions must be taken with these methods, especially when preparing the specimens. As for metallic materials, it is essential to polish the specimen and use chemical attacks to enhance the contrast between fibers and matrix. By polishing specimens, there is a risk of degrading the initial cross-section through the grubbing-up of fibers but the main problem with this method is the 2D aspect. Indeed, if fibers were oriented perpendicularly to the plan, their representation with 2D analyses would be a circle. Yet, fibers tilt, with respect to observed plan, is actually variable. Thus, their cut in a 2D view is no longer a circle but an ellipse (Fig. 1.9). For example, Eberhardt et al. [7] have determined elliptical parameters for different fibers and highlighted the existing significant error induced by this method. They have compared the previous method with results from confocal technique. It has been seen that the error measured depends on fiber orientation and can reach up to 10 degrees of difference with respect to the real value. It is to note that the assumption of a circular fibers' cross-section

can only be made for glass fibers (or more generally for mineral fibers) but this method is not suitable for modeling natural fibers' cross-sections because of their particular shapes.

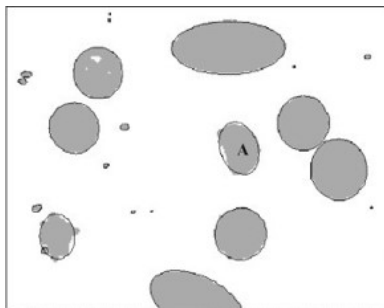


FIGURE 1.9: Example of natural fiber cross-section [7]

When possible, a 3D analysis is therefore preferable. In a growing number of cases, the 3D chosen method is micro-tomography [64]. This method is a non-destructive method, using x-ray scan over a rotating specimen, which allows a slice-by-slice reconstruction of the microstructure volume [65]. As a non-destructive method, it is possible to scan a specimen before testing it, aiming at correlating microstructure organization and mechanical properties. In this PhD thesis, micro-tomography is used to measure fibers geometrical properties as well as their orientation. More details about the measurement procedure are given in Section 1.4.2.

Through this section, the complex behavior of thermoplastics has been seen as well as the specificities of the interface between matrix and fibers. The case of thermoplastics reinforced with short fibers implies a good characterization of its microstructure. It is to note that fibers' specificities highlighted in Section 1.1.1 must be considered to master SFRT' behavior. Especially in the case of fibers' orientation and fibers' geometrical properties. The next section discusses about the quantification of the sources of variability of fibers' properties and about their propagation to composite mechanical behavior.

1.3 Sources of uncertainty of composite mechanical behavior

In science, studying uncertainty of a system means studying the variation of system's outputs (e.g. stress, strain, frequencies, ...) induced by the quantified variation of the system input parameters, such as fibers characteristics, Young's modulus, etc. In order to control these outputs, it is therefore relevant to know how to deal with uncertainty. First, uncertainty is divided into two classes: irreducible and reducible uncertainties. The difference between them is due to the unpredictable nature of the uncertainty. Indeed, for irreducible uncertainties, even

with a large number of data, some events remain unpredictable, on the contrary, reducible (or epistemic) uncertainties may be reduced when dealing with a large number of data. Then, three sources of uncertainty have been highlighted in the literature: measurement uncertainty, model uncertainty and physical variability [66]. Measurement uncertainties are induced by the data measurement stage. For example, it has been seen with Eberhardt et al. [7] that using 2D images for quantifying fiber orientation leads to significant error. This error can be reduced by using 3D measurement instead of 2D measurement (see Section 1.2.2 and fibers). Also, particular attention must be paid to the means of measurement for sources of uncertainty because it may influence significantly the results of the uncertainty quantification. Indeed, Le Moigne et al. [8] have obtained different results for the measurement of fiber's dimensional properties (e.g. length, cross-section) by using two measurement methods. The first method is purely manual: they have measured the length and aspect ratio (length / diameter) of fibers thanks to a numerical caliper. The second method is made by using a software developed by Microvision Instrument where the geometrical characteristics of the fibers are derived from the detection of the edges of the fibers. With the method "by hand" they measured 300 fibers whereas the software managed to measure 2.500 fibers (Figure 1.10). The distributions induced by these two methods are different, in the case of "by hand" measurements, small fibers ($< 60 \mu\text{m}$) are omitted because of limits of eye selection. On the contrary, the software is able to detect all fibers (even the smallest) and give more accurate distribution. Then, the model uncertainty is directly linked with the accuracy of the method. This uncertainty can be reduced by finding the best method to represent the studied case. For example, in their study, Cui et al. [67] have compared three different models and used the maximum likelihood estimation to identify the one in which the model uncertainty is the lowest. Finally, physical variability refers to variability induced by physical variables (e.g. material properties...), environmental conditions (e.g. temperature, humidity...), operational variations (e.g. loading conditions...) or manufacturing process (e.g. injection-molded process...).



FIGURE 1.10: Comparison between "by hand" measurement and measurement made with a software for (a) fibers' length and (b) fibers' aspect ratio [8]

The general procedure to deal with every source of uncertainty requires a first stage of uncertainty quantification and uncertainty modeling, these points are discussed in the next section.

1.3.1 Uncertainty quantification for composite materials from fibers to injection molded process

As seen in previous section, the mechanical behavior depends on both fibers properties and fibers' orientation which is directly induced by injection molded process. This section aims to quantify the uncertainty of SFRT microstructure and mechanical behavior induced by natural fibers properties and injection molded process.

Short natural fibers uncertainty quantification

In SFRT, the matrix is the component with the highest volume proportion. However, the uncertainty of its mechanical property does not have a significant impact on composite mechanical properties' uncertainty (see Section 2.3). On the contrary, with a lower volume proportion and depending on loading direction, fibers have more significant impact on composite uncertainty. Synthetic fibers (e.g. glass fibers) have globally constant geometrical and mechanical properties thanks to a controlled manufacturing process. On the contrary, plant fibers present much more variable characteristics leading to bigger uncertainty of composite's behavior. This uncertainty is induced by several aspects like chemical composition of fibers, itself influenced by numerous factors such as growing conditions of the stem, the morphology of the fiber, etc. Thuault [68] highlighted the importance of the cultivation conditions during the growth of the plant by comparing mechanical properties of flax cultivated in 2005 and in 2008. For the first one, climatic analyses have shown optimal temperature and sufficient water intake. For the second one, the same analyses have found a wet period during harvesting. The test highlighted better mechanical properties for the flax cultivated in 2005 (e.g. $E \approx 55 \pm 25$ GPa in 2005 and $E \approx 40 \pm 15$ GPa in 2008). Moreover, the location of the extraction of fibers inside the stem impacts the mechanical properties of plant fibers. Indeed, several studies have measured the variability of fibers' diameter over its length [69–71]. Charlet [71] has shown that extracting fibers from the middle of the stem leads to different fiber properties. For example, the mean diameter for flax fibers extracted from the middle of the stem is $12,4 \pm 3,2 \mu\text{m}$ against $16,5 \pm 5,1 \mu\text{m}$ for fibers extracted from the bottom of the stem. The difference is due to higher

amount of cellulose and pectic cement in the middle of the plant. Baley [9] has studied the importance of fiber diameter on the Young's modulus of flax fibers (Figure 1.11). The results correlate a decrease of the Young's modulus while fiber diameter increases. The same trend has been highlighted for fiber length by Anderson et al. [72], the strength increases while fiber length decreases. For authors, this phenomenon is linked to fiber defects content. Indeed, the longer the fibers are, the higher the occurrence of defects is.

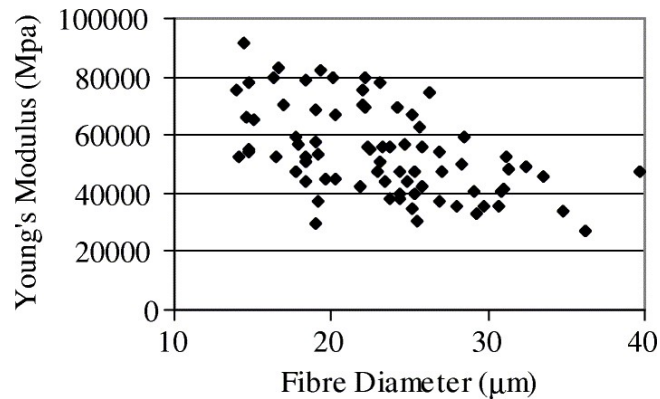


FIGURE 1.11: Young's modulus of flax fiber [9]

Also, the link between mechanical properties of the fibers and their composition has been pointed out by many studies [3, 8, 9, 73, 74]. Indeed, it has been noted that fiber strength increases as cellulose content increases.

For the morphology of fibers, the number of elementary fibers within a fiber bundle is also variable. Indeed, Mattrand et al. [75] have studied the number of elementary fibers included in flax technical fibers. They found that the minimum number of elementary fibers was two and the maximum was fifteen. The dimensions of elementary fibers are also to be considered. Because of their complex structure and geometry, it is difficult to define proper values for fiber cross-section (or diameter). Thomason et al. [69] have compared values of cross-section area directly measured on fiber bundles versus values of cross-section diameter calculated by assuming a circular shape for the cross-section of flax fiber bundles. According to the authors, the cross-section values obtained with this method are the double of values obtained when measuring the cross-section directly on fiber bundles. Therefore, the method assuming a circular fiber bundle cross-section is not an efficient method because it leads to wrong values of fibers' Young's modulus due to previous error.

Injection molded process uncertainty quantification

The orientation of fibers is set during the injection molded process (such as the five-layers structure, see Section 1.1.3) and may be influenced by several process parameters.

The gates directly impact the melt flow path into the mold and thus fiber orientation [10, 76]. The formation of the core layer, with fibers oriented transversely to the Injection Flow Direction (IFD), is made by a diverging flow induced by gating arrangements. However, film-gates or sprue-gates allow fibers in the core layer to be oriented parallelly to the IFD [77]. The injection speed has a direct effect on the thickness of the core layer, and thus on fibers' distribution of orientation through the thickness [78]. Actually, Gupta and Wang [35] have shown that decreasing the injection speed increases the thickness of the skin layers, then leading to a translation of the shear layers to the core, thus finally reducing the thickness of the core layer. On the contrary, increasing the injection speed increases the thickness of the core layer. Few studies have evaluated the impact of the packing stage but Shokri and Bhatnagar [79, 80] have shown that an insufficient packing stage duration leads to an increase of the core layer thickness.

Obviously, the mold temperature has a strong influence on the thickness of the skin layers. A high temperature gradient between mold walls and melted flow will quickly freeze the material near the walls. So, fibers do not have the time to re-orient themselves and adopt random orientation. It can be noted that the thickness of those skin layers increases with the gradient of temperature. However, with a low temperature gradient, the material near mold walls is slowly cooled and fibers can be re-oriented by the fountain effect [78, 81]. Also, the melt temperature impacts the shear rate and thus fiber's orientation [82, 83]. A reduction of this temperature induces an increase of the viscosity of the material and a faster solidification of the melt near the mold walls, thus increasing the shear rate. Therefore, fibers have time to re-orient themselves and the thickness of the shear layer increases, i.e. more fibers are oriented parallel to the IFD [84].

The studies of Vincent et al. [10] and of Gillespie et al. [85] highlight the dependency of the shear rate to the thickness of the pieces. According to Vincent et al. [10], the decrease of the part thickness leads to nearly uniform fibers' orientation due to high shear rate. This high value allows fibers to re-orient themselves parallelly to the IFD. On the contrary, when the thickness of pieces increases, fibers cannot be re-oriented parallelly to the IFD because of low shear rate. Figure 1.12 shows fiber's orientation throughout several thicknesses of injection molded plaques

(200mm x 40 mm). As it can be seen, by increasing the thickness of the pieces the core layer becomes larger with the increasing thickness (i.e. more fibers oriented perpendicularly to the IFD).

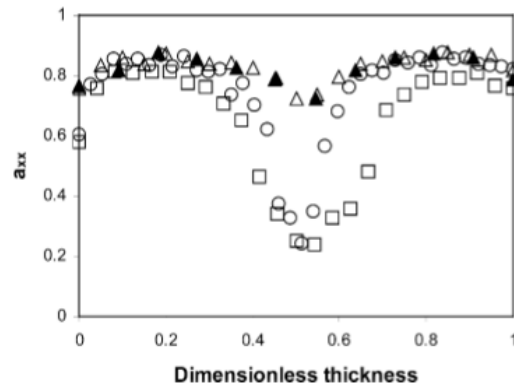


FIGURE 1.12: Evolution of the fiber orientation through thickness. The bold triangles represent parts with thickness of 1.1 mm, the empty triangles for 1.7mm, the circles for 3mm and the squares for 5mm [10]

Keeping in mind that fiber local orientations with respect to macroscopic loading direction have a great impact on SFRT tensile behavior, it is therefore crucial to be able to quantify the variability of fibers orientation. Indeed, the wide range of fibers orientation is responsible for an anisotropic behavior of the composite. Notta-Cuvier et al. [11, 86] have studied the variability of fiber orientation distributions using tensile specimens cut along the IFD (also loading direction), as illustrated by Figure 1.13. The aims are to quantify the variability on tensile behavior induced by the variable orientation distributions. One can see that the dispersion of tensile results (Figure 1.13 a) is directly linked with the orientation measured inside scanned volume (Figure 1.13 b).

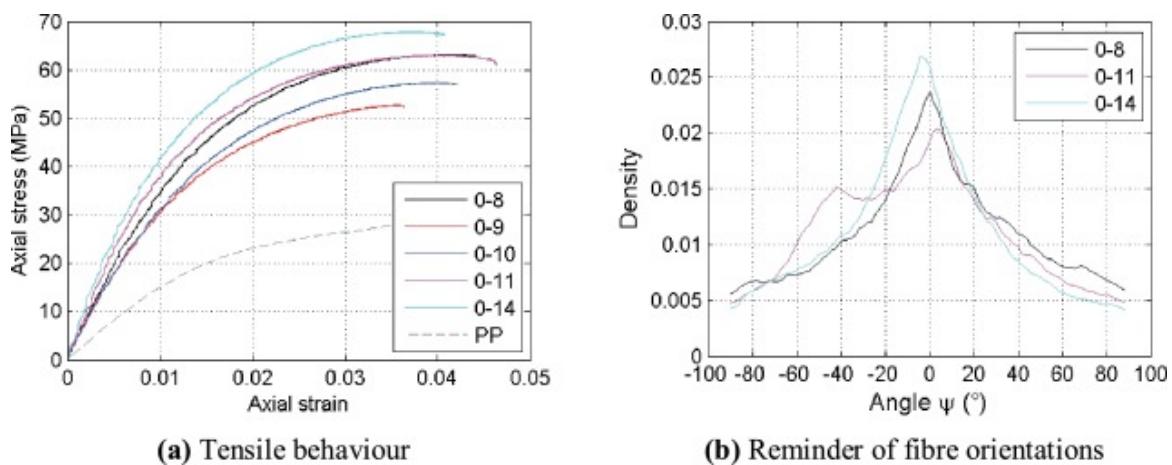


FIGURE 1.13: Tensile test of glass fiber reinforced polypropylene [11]

It is important to note that fibers variable properties also impact the fatigue behavior [67, 87, 88], the crash behavior [89–91] and the vibration response [92–94] of SFRT. However, according to authors, there are only few studies that quantify the impact of fiber variability on those behaviors, especially for their vibratory response and their crash behavior. This lack of study is an obstacle for automotive manufacturers for whom the vibration response and the crash behavior must be mastered to validate the design of parts. In the automotive field, eigenfrequency of parts must be comprised through specific bounds to avoid early breakkage, for instance. Concerning the crash behavior of parts, it is important for the industry to obtain reliable prediction of rupture initiation zones. Therefore, it is necessary to have a reliable model, taking into account all the behavior specifications and in particular damage mechanisms that can lead to failure. Thus, in this PhD thesis work, it is proposed to study the impact of natural fibers' variable properties on these two behaviors.

Table 1.1 summarizes the uncertainty found for composite materials seen in section 1.3.1.

Type	Uncertainty kind	References	Identified Uncertainty
Plant	Stem chemical composition	[69–71]	Fibers' mean diameter, Young's modulus
	Fiber geometrical properties	[9, 72]	Young's modulus
Process parameters	Gates design	[10, 76, 77]	Fiber orientation in core layer
	Injection speed	[35, 78]	Thickness of the core layer
	Packing stage duration	[79, 80]	Thickness of the core layer
	Mold temperature	[78, 81]	Thickness of the skin layer
	Melt temperature	[82–84]	Rheology of the material
Material characteristics	Rheology of the material	[82, 83]	Material velocity profile during injection
	Fiber content	[60, 95–97]	Thickness of the core layer
Other	Means of measurement	[69]	Precision of values
	Thickness of the pieces	[10, 85]	Shear rate

TABLE 1.1: Summary of the different sources of uncertainty enumerated in subsection 1.3.1

1.3.2 Modeling uncertainty of composite materials

After identifying the sources of uncertainty for composite materials, the next stage is to model them. This step consists in converting scattered experimental data into non-deterministic quantities. To achieve this aim, several theories and methods are used. Probabilistic theories, interval theories and fuzzy sets theories are traditionally the most used in mechanical engineering. For composite problematics, authors have mainly investigated the probabilistic way

by defining a probability density function from experimental data. Two probabilistic methods can be found in the literature, namely parametric and non-parametric. In the case of parametric probabilistic approaches, the aim is to quantify the uncertainty of the variable parameters such as material properties, for example fibers' Young's modulus. To do so, random variables are associated to each uncertain parameters. For example, Hohe et al. [98] used this way for long fiber reinforced thermoplastic and showed the variation of the material response induced by the uncertainty of fiber orientation and local fiber content. In the case of non-parametric probabilistic approaches, the matrices governing the problem are considered uncertain to define the uncertainty of the whole system. In their study, Piovan et al. [99] have used both parametric and non-parametric approaches for a dynamic study with thin-walled beams defined with a graphite-epoxy composite (AS4/3501-6). For the parametric probabilistic approach, the authors have considered the parameters related to the elastic properties as variable whereas uncertain stiffness and damping matrices of the model are defined for the non-parametric approach. One conclusion of their study is the presence of areas that are more sensitive to the variation of parameters (parametric approach) and/or to the variation of the model (non-parametric approach). Hessman et al. [100] developed a toolbox in order to extract probability density function for fibers' properties (e.g. Gaussian distribution for fiber radius). Also, Moigne et al. [8] tried to find the most suitable probability density function between Weibull distribution and log-normal distribution for flax and sisal fiber length. Both distributions were evaluated with P-value analysis. The aim of this evaluation is to characterize the likeness between experimental data and the chosen distribution. According to the authors, Weibull distribution shows best fitted results in that case. Also, Sala et al. [101] uses the Anderson-Darling statistic test in order to evaluate the correspondence between mechanical properties of a woven hemp fabric-reinforced GreenPox composite and distribution laws modeling these mechanical behaviors. It has been seen that for some parameters, such as strength and ultimate strain, Weibull distributions are the distributions that fit the best the results.

In the case of sparse data, the definition of probability distribution is questionable. Indeed, in numerous articles, authors have arbitrarily chosen uniform laws to model the input uncertainty. In this context, non-probabilistic approaches, for example fuzzy or interval theories [12, 102] are considered. In this case, the variability is defined by an interval or a set of intervals. For the fuzzy set theory, the reference method is the Zadeh's Extension Principle (ZEP). The aim is to build the membership functions of output data as a function to those of input data. Fuzzy set theory is an extension of ordinary set theory, in which each object either belongs to a set or does not. Fuzzy set theory introduces the notion of degree of membership, using a membership function (triangular, trapezoidal...) to describe, for each element in the domain, the degree of membership in the fuzzy set. This function can take different forms,

depending on the user's perception of the input's imprecision. Dey et al. [12] used the fuzzy theory for the representation of ply orientation angle, graphite-epoxy elastic modulus and shear modulus. Naskar et al. [103] have worked on a fuzzy representative volume element in order to add the spatial variation of parameters such as ply orientation. Babuska et al. [104] have developed a hybrid fuzzy method which combines the traditional fuzzy moments with random fields. This new method aims to predict the uncertainty of fiber composites (more broadly in multiscale models). From these studies, it can be seen that the general representation, or at least the most used, for the fuzzy membership function is a triangular function. This function usually associates the mean value with the apex of the triangle and the extremities of it with the standard deviation of the measured data (see Figure 1.14). Therefore, it is legitimate to ask if this representation is the most relevant. Indeed, as the measured data are part of the samples, their value from the membership function could be equal to one, instead of a decreasing value from one to zero. Then, the uncertainty added by the measuring stage, the model used, etc, should be taken into account by adding unmeasured values. This inclusion is made with the membership function, by decreasing the values of this function with a user-defined slope. A trapezoidal function is created by doing this method [105]. The fuzzy logic used by Sodoke et al. [106], aims to accommodate the Young's modulus measured with different test rig (tensile test, bending test and acoustic impulse). During the test rigs, the material used was a flax-epoxy natural fiber composite.

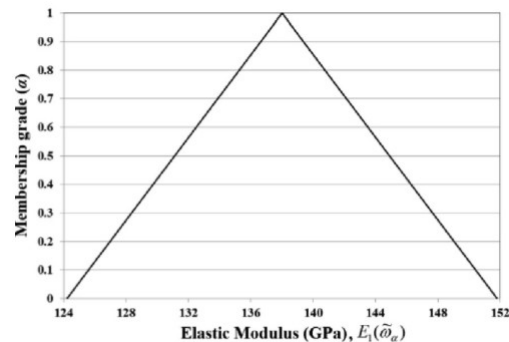


FIGURE 1.14: Example of fuzzy membership function [12]

Some authors have studied the results given by different types of uncertainty-based methods. Alazwari and Rao [107] have studied model uncertainty for stress distribution through thickness of laminates composites by using probabilistic approach, interval analysis and universal grey theory in order to compare the results. In universal grey system theory the arithmetic operations are different from interval theory. The aim of this method is to avoid the dependency problem encountered by the interval theory which leads to more accurate results [108]. It can be seen that in this case, the confidence interval given by the probabilistic approach is

more accurate than the one given by interval analysis and universal grey theory. This accuracy is provided by a better precision of the probability distributions used in the probabilistic approach.

Table 1.2 summarizes the different methods to model the uncertainty for composite materials seen in section 1.3.2

Model	Type of approach	References	Comments
Probabilistic	Parametric	[98, 99]	Graphite epoxy composite, Short-glass-fiber-reinforced polyamide
	Non-parametric	[99]	Graphite epoxy composite Short-glass-fiber-reinforced thermoplastic,
	PDF extraction	[8, 100, 107]	Natural-fiber-reinforced composite
Fuzzy Logic	General Fuzzy Logic	[12, 106]	Triangular function, Young's modulus measurement
Fuzzy	Fuzzy representative volume element	[103]	Aim to add spatial variation Combination of fuzzy logic and random fields
	Fuzzy-stochastic	[104]	
Interval	Interval theory	[107, 108]	
Other	Universal Grey Theory	[107]	

TABLE 1.2: Summary of the different way to model the uncertainty enumerated in subsection 1.3.2

After modeling the uncertainties, the next stage is to propagate the uncertainty of the input to the output. This last stage is depicted in the following section.

1.3.3 Uncertainty propagation and uncertainty management

Like in other domains, the aim of uncertainty propagation step in mechanics is to transfer the uncertainty associated to input variables (material properties, fibers' geometrical properties, ...) towards the output (displacement, strain, stress, failure, frequency, ...). The link between the inputs and outputs is made by a "transfer function", which directly traduces the studied case and so the mathematical problem to be solved. This transfert function can be analytical, numeric or a succession of linear or nonlinear stages, integrating for example finite element simulations.

For the uncertainty propagation, Monte-Carlo Simulation (MCS) is the reference probabilistic

method. The sampling MCS is widely used with finite element method [109–111]. The principle is to evaluate the “transfer function” for a large number of samples of the studied model while applying a FEM simulation. The used values for input variables are randomly extracted through associated Cumulative Density Functions (CDF). For example, Lee et al. [112] and Zhou et al. [113] have respectively estimated mechanical properties of glass fiber reinforced composite and simulated tensile failure process of carbon reinforced composite. Next, Jeong et al. [114] used MCS to investigate tensile failure process of fiber reinforced plastic laminated plates. However, to achieve a convergence for the mean or the variance of outputs and guarantee a good level of calculation, the number of samples must necessarily be very important and so the method becomes time-consuming.

To overcome the computing time problem, alternative approaches have been proposed in the literature. On one side, Sudret [115, 116] distinguishes two probabilistic models, intrusive and non-intrusive methods. The first one requires a modification of the computing code and the definition of a new mathematical problem to identify the unknowns of the proposed algorithms. On the contrary, the second one makes reference to a way where the initial code is not modified and is used to generate a training set. In the literature, many authors used non-intrusive methods. Indeed, for Carrere et al. [117] non-intrusive methods are the answer of a large number of applications, such as industrial problems, in which the computing code cannot be modified. Two methods stand out, the Reduced Order Models (ROM) and the surrogate models, either directly integrated in the alternative method (for example in the case of Polynomial Chaos Expansion, PCE, with polynomial series), or coupled with the reference method (for example a kriging with MCS). The idea of the ROM is to reduce the initial database (e.g. orthogonal decomposition). Then, the aim of surrogate models is to replace the initial problem by an efficient approximation of output solutions (e.g. PCE, kriging). These last years, PCE methods have been widely used and especially the generalized PCE. The principle of this method is to project stochastic solutions of the initial model onto polynomials orthogonal base [118]. According to the Askey scheme, the type of polynomial series is defined by the type of the variable (for example, for Gaussian variables, Hermite polynomials are used [119]). In their study, Thapa et al. [120] proposed a non-intrusive PCE method, which relies on an automatic differentiation to facilitate the calculation of sensitivities of the stochastic response and the expansion terms with regard to the uncertain input parameters. This proposed method was exploited to investigate multi-scale buckling in the case of carbon fiber reinforced composites.

The most efficient alternative methods are firstly based on the decomposition of the input membership functions into intervals according to α -cut level. Secondly, each interval problem is transformed into a min-max optimization problem and a surrogate [121], or a ROM [122], is integrated at each iteration. This strategy has been successfully used by Massa et al. for

different mechanical problems (static [123], modal [105, 121], frequency responses [121], stability analysis [122]). Dey et al. [12] used a new fuzzy propagation method based on the work of Chowdurry et al. [124], for dynamic characterization of a laminated composite (first three natural frequencies).

In order to better understand the behavior of model output(s) throughout variation of input parameter(s), sensitivity analyses are classically used. These analyses quantify the weight of each input parameters by using results from Uncertainty Quantification (UQ) and Uncertainty Propagation (UP) stages. Global sensitivity analysis allows to simulate simultaneous variation for each parameter during the analysis. On the contrary, during local sensitivity analysis the variation of parameters is made one by one and does not include interactions between parameters. In order to find the key parameters (i.e. parameters having the greatest impact), it is essential to compare simultaneously multiple input parameters and therefore to use global sensitivity analysis. Del Mastro et al. [125] have conducted a numerical analysis study in order to find parameters with the biggest impact for flax and hemp fibers mechanical properties. At the beginning of the study, twenty-six different parameters were selected (such as fiber diameter, viscoelastic parameters, elastic moduli of fibers' constituents...) and then, with two sensitivity analyses, they managed to reduce to seven key parameters. For the first sensitivity analysis, they used Morris screening method. This method evaluates the impact of one input parameters at a time on the output. This method is usually used for models with numerous input parameters. The aim is to reduce the dimension of the problem with a first selection made by calculating a sensitivity index (i.e. elementary effect). Then, the second sensitivity analysis used is the Fourier Amplitude Sensitivity Test (FAST). The latter is a variance-based method, it means that the variance of input parameter(s) is used to determine the sensitivity indices. Therefore, attention must be paid to the estimation of inputs' variance.

Ghauch et al. [126] combined PCE with Sobol indices to achieve sensitivity analysis with the injection of fiber composite materials. They have studied the impact of 74 parameters to identify those which are the most critical during the injection process. This study leads to a better understanding of the injection process and makes possible its optimization. Sobol indices are ANOVA based methods (ANalysis Of VARIance). The aim is to decompose the total variance of the output(s) into indices that reflect the impact of each input on the output(s) and also the interaction between inputs. Omairey et al. [127] have made sensitivity analysis in order to analyze the effect of multi-scale uncertainty on reliability of the composite. They used Sobol indices for the sensitivity analyses and linked composite mechanical properties (Young's modulus, shear moduli and Poisson's ratio) to material and geometrical (both fiber and matrix) uncertainties. For example, it has been shown that the longitudinal Young's modulus is mainly affected by fiber's stiffness and that the shear moduli are mainly affected by matrix stiffness.

This result agrees with the assumption made and verified in Section 2.2: fibers efficiency is maximized if they are loaded in their axis direction.

Another way to manage the uncertainty is to use the Robust Design Optimization (RDO). The aim of this method is to find the best compromise between characteristics of the system. The RDO method have been used by Antonio et al. [128] with angle-ply composite made of E-glass/epoxy. In their study, they wanted to optimize the couple performances of the system and its robustness. In addition to the RDO method, they used Pareto curves to determine the best couple. Also, Kalantari et al. [129] used the RDO in order to optimize the strength, the cost and the weight of carbon/glass fibers reinforced hybrid composite during flexural loading. In their study, they have used this method by considering the uncertainty induced by inputs parameters such as thickness, fibers' orientation.

Table 1.3 summarizes the different methods used to propagate and to manage the uncertainty for composite materials as seen in section 1.3.3

Model	Type of approach	References	Comments
Reference method	Monte Carlo simulation	[109–114, 130]	Reference method
Alternative methods	surrogate Intrusive / non intrusive methods	[118, 121] [115–117]	PCE or kriging min-max optimization problem and ROM
	Reduced order model Fuzzy propagation	[122] [12, 124]	dynamic characteization
Sensitivity analyses	Morris screening	[125]	flax and hemp fibers mechanical properties
	Fourier amplitude sensitivity test (FAST)	[125]	flax and hemp fibers mechanical properties
	Sobol indices	[126, 127]	ANOVA method
Optimization	Robust design optimization	[128, 129]	find the best compromise between characteristics

TABLE 1.3: Summary of the different way to propagate and to manage the uncertainty enumerated in sub-section 1.3.3

Through this section, different sources of uncertainty and different way of reporting this uncertainty have been seen. Also, the propagation of the uncertainty of different elements (such as fibers, process parameters...) to SFRT behavior has been reviewed. In this PhD thesis work, SFRT's mechanical behavior is modeled taking into account variable fibers' orientation and fibers geometrical properties. In view of this, the variable parameters of fibers (here orientation and geometrical properties) are quantified using micro-computed tomography, details are given

in Section 2. Beforehand, the next section of this state of the art aims to introduce two different tools used during this PhD thesis. The first one is the user-material subroutine (developed in LAMIH) that allows simulate the complex behavior of SFRT. The second one is the presentation of the principle of X-ray microtomography scanning and post-treatment method that allow to quantify fibers orientation and geometrical properties variability.

1.4 Description of existing tools in the laboratory

1.4.1 VE-VP-damage behavior model for SFRT

As seen in section 1.2, SFRT's behavior is complex because of numerous specificities. To allow its numerical prediction, especially for cases of high-strain-rate loadings, researchers of LAMIH have developed constitutive equations which are implemented in an Abaqus-explicit user-material subroutine (also called VUMAT), written in FORTRAN77 [86, 131, 132]. The aim of this subsection is to provide basic knowledges regarding this model (for more details readers may refer to [133, 134], e.g.). In order to simulate SFRT's behavior, this model considers matrix specificities (viscoelasticity, viscoplasticity,...), the complex characteristics of the reinforcement (such as fibers orientation and geometrical properties - possibly variable) and also damage mechanisms. The framework of small transformation is assumed. The matrix strain tensor is assumed to be equal to the composite strain tensor and the total strain is divided into a (visco)elastic strain ε^{ve} and a (visco)plastic strain ε^{vp} . Fibers are supposed to carry load only in their axis direction.

The composite material is split into one matrix medium and N fibers family, allowing to take into account various fibers properties (orientation, length, Young modulus...). As already stated, the total strain is split into two parts, as follow:

$$\varepsilon = \varepsilon^{ve} + \varepsilon^{vp} \quad (1.1)$$

To take the viscoelastic strain history into account, the viscoelastic behavior uses Boltzmann's hereditary integral to express the effective matrix Cauchy stress tensor:

$$\tilde{\sigma}_M(t) = \int_0^t Q(t-\xi) : \frac{\partial \varepsilon^{ve}(\xi)}{\partial \xi} d\xi \quad (1.2)$$

where Q is the 4th-order relaxation tensor. The viscoelastic modulus is expressed using Generalised Maxwell model (see Section 1.2.1), thus giving the following expression:

$$E(t) = E_\infty + \sum_{i=1}^N E_i(t) \exp\left(\frac{-t}{\tau_i}\right) \quad (1.3)$$

with E_∞ the infinite modulus, E_i the time dependant moduli and τ_i characteristic time of spring and damper, respectively, mounted in series for each branch i . The expression of the 4th-order relaxation tensor is given by:

$$Q_{ijkl}(t) = 2\mu(t) \delta_{ik} \delta_{jl} + \Lambda(t) \delta_{ij} \delta_{kl} \quad (1.4)$$

where δ is Kronecker symbol and $\mu(t) = \frac{E(t)}{2(1+\nu)}$ and $\Lambda(t) = \frac{E(t)\nu}{(1+\nu)(1-2\nu)}$, where ν is the matrix Poisson coefficient. Then, the decomposition into a linear (or infinite) part and several Maxwell (time dependant) parts leads to:

$$\left\{ \begin{array}{l} \mu(t) = \mu_\infty + \sum_i \mu_i \exp\left(\frac{-t}{\tau_i}\right) \\ \mu_\infty = \frac{E_\infty}{2(1+\nu)} \\ \mu_i = \frac{E_i}{2(1+\nu)}, \forall i \end{array} \right. \quad \text{and} \quad \left\{ \begin{array}{l} \Lambda(t) = \Lambda_\infty + \sum_i \Lambda_i \exp\left(\frac{-t}{\tau_i}\right) \\ \Lambda_\infty = \frac{E_\infty \nu}{(1+\nu)(1-2\nu)} \\ \Lambda_i = \frac{E_i \nu}{(1+\nu)(1-2\nu)}, \forall i \end{array} \right. \quad (1.5)$$

and therefore:

$$\left\{ \begin{array}{l} \tilde{\sigma}_M(t) = \tilde{\sigma}_{M\infty}(t) + \sum_i \tilde{\sigma}_{Mi}(t) \\ \tilde{\sigma}_{M\infty}(t) = 2\mu_\infty \varepsilon^{ve}(t) + \Lambda_\infty \text{tr}(\varepsilon^{ve}(t)) I \\ \tilde{\sigma}_{Mi}(t) = 2\mu_i \int_0^t \exp\left(\frac{-(t-\xi)}{\tau_i}\right) \frac{\partial \varepsilon^{ve}(\xi)}{\partial \xi} d\xi + \Lambda_i \int_0^t \exp\left(\frac{-(t-\xi)}{\tau_i}\right) \frac{\partial \text{tr}(\varepsilon^{ve}(\xi))}{\partial \xi} d\xi I \end{array} \right. \quad (1.6)$$

The yield criterion is defined by:

$$\tilde{\phi} = \frac{(\eta - 1) \tilde{I}_1 + \sqrt{(\eta - 1)^2 \tilde{I}_1^2 + 12\eta \tilde{I}_2}}{2\eta} \quad (1.7)$$

where $\eta = \sigma_{C0}/\sigma_{T0}$ is the ratio between the initial yield stress in compression and in tension, \tilde{I}_1 and \tilde{I}_2 are respectively the first and second invariant of matrix effective Cauchy stress tensor expressed by $\tilde{I}_1 = \frac{1}{3} \text{tr}(\tilde{\sigma}_M)$ and $\tilde{I}_2 = \frac{1}{2} \tilde{S}_M : \tilde{S}_M$, where \tilde{S}_M is the deviator of $\tilde{\sigma}_M$. This expression allows to consider the hydrostatic pressure sensitivity of plastic flow of thermoplastics materials.

The yield stress, $\tilde{\sigma}_{M,y}$, is given by $\tilde{\sigma}_{M,y} = \sigma_{T0} + R(\kappa)$, where R is the hardening law and κ is the hardening variable which is assimilated to the cumulated plastic strain κ . It is important to note that in this model, all types of hardening laws can be considered. In this PhD thesis work, the following hardening law is considered:

$$R(\kappa) = h_1 \exp(h_2 \kappa^2) (1 - \exp(-h_3 \kappa)) \quad (1.8)$$

where h_1 , h_2 and h_3 are material parameters.

Finally, the quasi-static yield surface \tilde{f} is expressed as follow:

$$\tilde{f} = \tilde{\phi}(\tilde{I}_1, \tilde{I}_2) - (\sigma_{T0} + R(\kappa)) \quad (1.9)$$

and is corrected by a viscoplastic multiplier to consider the dilatation of the yield surface, leading to:

$$\tilde{F} = \tilde{\phi}(\tilde{I}_1, \tilde{I}_2) - [\sigma_{T0} + R(\kappa)] \left(\frac{\dot{\kappa}}{\dot{\kappa}_0} \right)^{1/m} \quad (1.10)$$

where $\dot{\kappa}_0$ and m are material parameters.

In practice, a viscoelastic prediction and viscoplastic correction scheme is used to compute $\tilde{\sigma}_M$. The principle of the implementation is to compute all mechanical quantities at increment $n+1$, knowing quantities at increment n and total strain increment tensor, $\Delta\varepsilon$, between increments n and $n+1$. At first step, the viscoelastic prediction supposes that this tensor is purely viscoelastic. Then, in the second step, a viscoplastic correction is applied to calculate the real proportion of strain increment. That is done considering the normality rule, here in the framework of non-associate plasticity, that allows to express the viscoplastic strain rate tensor:

$$\dot{\varepsilon}^{vp} = \dot{\tilde{\lambda}} \frac{\partial \tilde{\psi}^{vp}}{\partial \tilde{\sigma}_M} = \dot{\tilde{\lambda}} \vec{n} \quad (1.11)$$

In which $\tilde{\lambda}$ is the plastic multiplier, \vec{n} is the direction of return to the yield surface and $\tilde{\psi}^{vp}$ is the viscoplastic part of the thermodynamic potential, $\psi = \psi^{ve-D} + \tilde{\psi}^{vp}$ and is expressed by:

$$\tilde{\psi}^{vp} = \sqrt{3\tilde{I}_2 + \frac{1}{3} \left(a^+ \langle \tilde{I}_1 \rangle^2 + a^- \langle \tilde{I}_1 \rangle^2 \right)} \quad (1.12)$$

In this Equation, a^+ and a^- are material parameters that represent the volume variation of the material depending on the sign of the hydrostatic pressure, since the Macaulay brackets $\langle \tilde{I}_1 \rangle$, give 0 if $\tilde{I}_1 \leq 0$, \tilde{I}_1 otherwise.

Once Delta $\dot{\varepsilon}^{vp}$ is computed by iterations using Equation 1.11, the increment of viscoelastic strain is updated and the value of $\tilde{\sigma}_M$ is computed from Equation 1.6 using the actual value of ε^{ve} .

In this model, as matrix damage is isotrope, it is therefore defined by a scalar damage variable D_n which depends on the cumulated plastic strain following the Lemaitre's theory [135]. At composite scale, the hypothesis is made that the presence of fibers prevents matrix damage

in their axis direction. However, in this model, fibers are defined by several fibers families with different orientations thus introducing anisotropic behavior and damage. Therefore, a 4th order damage tensor D is introduced:

$$\sigma_M = D\tilde{\sigma}_M \quad (1.13)$$

For more details, readers can refer to [86, 136].

In this model, fibers are distributed into N_{fam} families. Each family is characterized by its orientation vector \vec{a}^α , geometrical properties, Young modulus E_F^α and its volume fraction within the composite. An important assumption is made in which fibers are supposed to carry load only in their axis direction. The direct consequence is that the fibers only deform longitudinally. For each fibers' family, the transformation gradient tensor is defined by:

$$F_F^\alpha = F A^\alpha \quad \forall \alpha \in \{1, \dots, N_{fam}\} \quad (1.14)$$

in which $A^\alpha = \vec{a}^\alpha \otimes \vec{a}^\alpha$ is the orientation matrix of fibers family α . Fibers' axial strain is expressed by:

$$\varepsilon_F^{Axial, \alpha} = \frac{1}{2} \ln(\lambda_F^\alpha) \quad \forall \alpha \in \{1, \dots, N_{fam}\} \quad (1.15)$$

where λ_F^α is the unique eigenvalue of the right Cauchy-Green tensor defined for each fibers family:

$$C_F^\alpha = F_F^{\alpha T} F_F^\alpha = A^\alpha C A^\alpha \quad (1.16)$$

with $C = F^T F$ the composite right Cauchy-Green tensor.

A shear lag model adapted from work by Bowyer and Boder [58] is implemented to calculate fibers average axial stress, and:

$$\sigma_F^{Axial \alpha} = \begin{cases} \left(1 - \frac{E_F^\alpha r^\alpha}{2L^\alpha \tau^\alpha} \left| \varepsilon_F^{Axial \alpha} \right| \right) E_F^\alpha \varepsilon_F^{Axial \alpha} & \text{if } \left| \varepsilon_F^{Axial \alpha} \right| \leq \frac{L^\alpha \tau^\alpha}{r^\alpha E_F^\alpha} \\ \text{otherwise } \sigma_F^{Axial \alpha} = \text{sign} \left(\varepsilon_F^{Axial \alpha} \right) \frac{L^\alpha \tau^\alpha}{2r^\alpha} \end{cases} \quad (1.17)$$

where τ^α is the fiber/matrix interfacial shear strength (IFSS) of fibers' family α .

An interfacial debonding is implemented in the model. It is triggered when the axial strain of fibers reaches a threshold, noted ε_{th} . Then, a portion of fiber length, δ^α , from fiber tips, becomes unavailable for load transmission. Evolution law of δ^α is given by:

$$\begin{cases} \delta^\alpha = a \left(\frac{\varepsilon_F^{Axial,\alpha} - \varepsilon_{th}}{\varepsilon_{th}} \right)^b \frac{L^\alpha}{2}, & \text{if } \varepsilon_F^{Axial,\alpha} \geq \varepsilon_{th} \\ \delta^\alpha = 0, & \text{otherwise} \end{cases} \quad (1.18)$$

where a and b are material parameters.

The hypothesis of iso-stress with matrix is made to compute the others components of each fibers family stress tensor. Then, in order to switch fibers' 3D stress tensor from local coordinates, $\sigma_F^{0,\alpha}$, to global coordinates, σ_F^α a transition matrix, T^α , is used:

$$\sigma_F^\alpha = T^\alpha \sigma_F^{0,\alpha} T^{\alpha-1} \quad (1.19)$$

Finally, the composite stress tensor is given by the assembly of the behavior of all phases, and:

$$\sigma_C = v_m \sigma_m + \sum_{\alpha=1}^N v_F^\alpha \sigma_F^\alpha \quad (1.20)$$

1.4.2 Realization and post-treatment of microtomographic scans

The Section 1.2.2 briefly discusses about 2D and 3D measurements of fibers geometrical properties as well as their orientation. In this PhD thesis work, micro-computed tomography is used to measure fibers' orientation and fibers' geometrical properties (cross section and length). This scanning method, quite similar to the medical imaging, uses X-ray to project cross-sections of a rotating object at high resolution. By superimposing each image of the cross-section, it is possible to reconstruct the volume of the scanned specimen. Here, a short-natural-fiber-reinforced polypropylene (PP-30NF) and a short-glass-fiber-reinforced polypropylene (PP-35GF) are scanned, more details about the material considered can be found in Chapter 2 and the results are analyzed in Section 2.2.

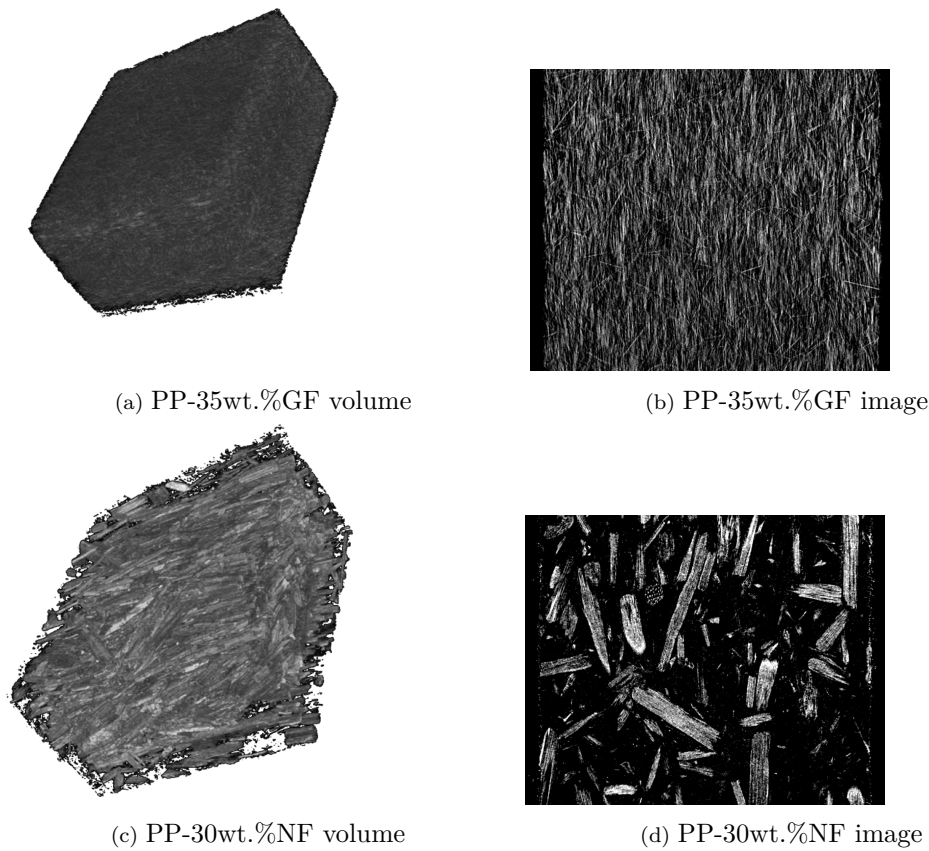


FIGURE 1.15: Image and 5 mm x 5 mm x 2.5 mm volumes of PPNF and PPGF reconstructed with Fiji, at same resolution, see table 1.4

In this work, different specimens have been scanned and two micro-tomographs have been used. The first one is a Skyscan 1172 X-ray and the second one is a high resolution Ultratom microtomograph from RX Solutions (Isis4D platform). The Skyscan 1172 X-ray micro-tomograph has been used to scan volumes of 5 mm x 5 mm x 2.5 mm in the center of some tensile specimens (see Fig. 1.15). The second microtomograph has been used to scan barrels of higher dimensions, here after designated as vibration specimens. The parameters used for both types of scans are summarized in Table 1.4.

	Tensile specimens	Vibration specimens
Source voltage [kV]	25	50
Source current [μ A]	44	110
Scan duration [minutes]	70	15
Volume scanned	5 mm x 5 mm x 2.5 mm	10 mm x 10 mm x 2.5 mm
Pixel size [μ m]	3.87	7.08
Number of scans	66	63

TABLE 1.4: Parameters used during the micro-computed tomography

It is important to note that because of the high content of glass fibers (see Figure 1.15), the

orientation of fibers (as well as their geometrical properties) could not be precisely measured and the results obtained were not exploitable. Thus, only the orientation of few glass fibers is measured through the thickness of PPGF. In the following, only the post-treatment procedure of PPNF scans is discussed.

After the scans are done, a threshold in grey level is applied in order to distinguish fibers from matrix. Each 3D scan is divided into two plans (Fig. 1.16). The first plan is used to measure fibers' orientation and length (red plan) and the second plan to measure fibers' cross-section (green plan). Both type of plans are post-treated with the same protocol.

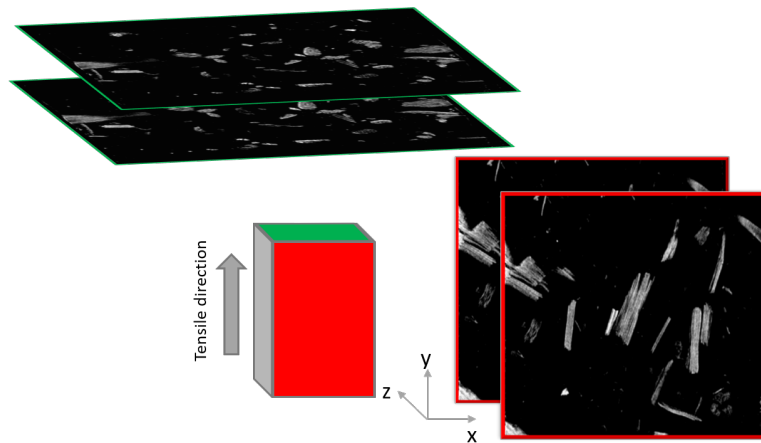


FIGURE 1.16: Extraction of plans (here 10%wt. PPNF)

The first stage is to turn each image into black and white images by applying a second threshold in grey level based on the Otsu method [137]. The aim is to smooth the fibers' boundaries by removing the grey variations. As stated in Section 1.1.1, technical fibers are composed of elementary fibers glued together by pectic cement. Also, the presence of a lumen may make elementary fibers hollow (see Figure 1.17). Because of these hollows, several small structures are detected instead of a single structure (technical fiber). Therefore, to remedy this situation, fibers' geometry is automatically reconstructed in the second stage by filling the hollows.

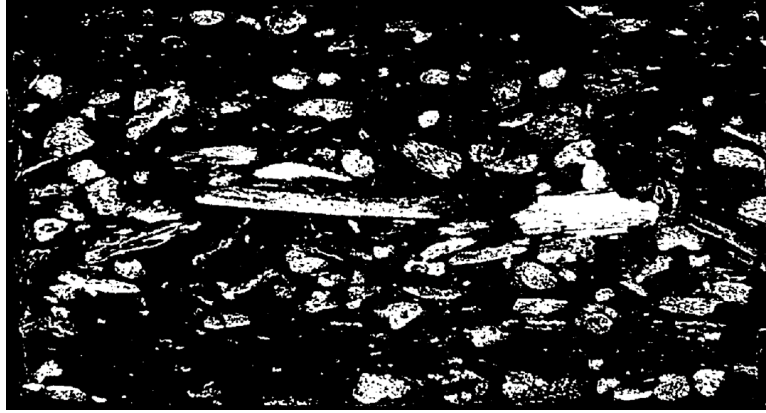


FIGURE 1.17: Example of natural fibers' porosities

The third stage aims to remove dust or small particles from each image in order to leave only the fibers. This is done by applying a size filter which removes particles with a length and/or diameter lower than 0.08 mm and 7 μm , respectively. These thresholds have been set after several measurements made on particles induced by the waterjet cuts (visible on the sides of the scans). Feret's diameters are used for the measurement of fibers' length and cross section [138–140]. Two diameters are measured, a minimum and a maximum for each particle. These diameters are the measure of two parallel lines that are tangential to the particle. For an elliptical shape, the maximum Feret diameter represents the major axis' length. On the contrary, the minimum Feret diameter represents the minor axis' length. Thus, in the case of vegetal fibers, the maximum Feret diameter represents fibers' length. For the cross section, the measured area is converted into square millimeters thanks to the voxel size. Concerning the fibers' orientation, a fictive line is drawn between the two farthest points of each detected fiber. The angle between this line and a fictive vertical line is considered as the fiber's orientation value. The vertical line is the same for each fiber and each scan which allows to measure fibers' orientation in the same system.

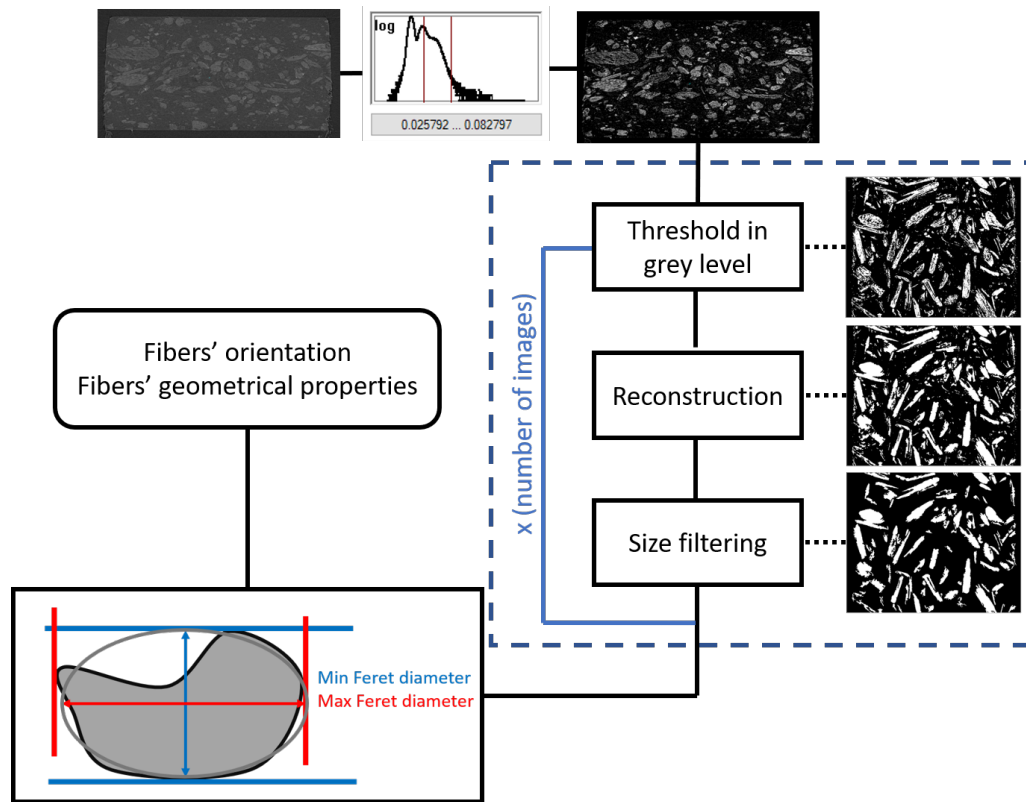


FIGURE 1.18: Schematic representation of the post-treatment of each scan

The volume fraction corresponding to fibers thus detected has been compared to theoretical volume fraction in the material, based on the knowledge of massic fraction and density of PP matrix and fibers. A difference between 3 and 8 % has been calculated. On the contrary, by removing the size filtering stage, the volume fraction detected for the fibers could exceed the real volume fraction of fibers (an excess of up to 4%). According to authors, removing the size filtering is a poor choice because it leads to the addition of wrong data and therefore overestimate the results linked to fibers' volume fraction.

1.5 Conclusions

In this chapter, the complex microstructure of SFRT has been studied and described.

Fibers' orientation is directly induced by the injection molding process. Fibers orientation depends on the choice of process parameters (injection speed, mold / melt temperature etc) and the geometry of injected parts (presence of holes, variable thicknesses etc) for both types type of fiber used. Fibers' properties obviously depend on fiber types. For example, glass fibers are man-made fibers whose mechanical and geometrical properties remain similar from one fiber to another. On the contrary, the complex structure of natural fibers makes their properties

(geometrical, mechanical, etc) more variable. From these microstructure specificities directly depends the mechanical behavior of composites. Indeed, it has been seen that geometrical properties and local orientation of fibers have a significant impact on SFRT behavior. Thus, using plant fibers increases the level of variability to be considered for the mechanical behavior of SFRT.

It has been seen that several tools are used to measure fibers variability (orientation of geometrical properties) inside the composites. Yet, the propagation of those variabilities on the mechanical response of SFRT with experimental cases is little studied, and in particular for the vibratory response of SFRT or their crash behavior. In view of this, in this PhD thesis work the propagation of fibers' variability to SFRT mechanical properties is studied. First, μ CT analyses are performed on short-natural-fibers-reinforced polypropylene in order to measure fibers' orientation and fibers' geometrical properties variabilities inside composites. Then, the impact of different sources of variability on the elastic behavior of SFRT is investigated by gradually increasing the number of sources of variability. Vibratory tests are performed on this material as well as on PP-35GF to measure the impact of the injection molding process variabilities and fibers geometrical properties variabilities on the vibration response of SFRT. Finally, bulge tests are carried out to investigate the propagation of fiber variabilities to the crash behavior of SFRT.

The next chapter aims to quantify the sources of variability of SFRTs' microstructure and to propagate them to SFRTs' Young modulus. In view of this, tensile specimens are cut into injection molded plates and each tensile specimens are scanned using a μ CT before tensile tests.

Chapter 2

Analyses of SFRTs' microstructure and mechanical behavior

Contents

2.1	Effect of process parameters on fiber orientation and Young's modulus of a PP-35GF	48
2.2	Natural fibers : variability of geometrical properties and orientation inside the composite	51
2.2.1	Natural fibers' geometrical properties	52
2.2.2	Natural fibers' orientation in injection-molded PP-30NF	54
2.3	Identification of the origins of composite's Young modulus variability	57
2.4	Conclusion	63

The previous chapter highlights the different sources of variability of SFRT. It has been reported that short fibers introduce intrinsic variability into microstructure and mechanical behavior of SFRT, which nature and importance depend on fiber types (natural or synthetic). Moreover, variable process parameters (nature and location of melt entrance zones, mold and melt temperature, injection speed, etc) can modify the organization of fibers in SFRT microstructure and so on composite's mechanical behavior. In industrial context, the accurate knowledge of the Young's modulus of materials is crucial to design parts, especially in case of vibration analysis. In view of this, in the first part of this chapter, the impact of process parameters on the orientation of short glass fibers and on the Young modulus of

PP-35GF is studied. To do so, tensile specimens are cut into plates produced by injection molding, with different sets of process parameters. The microstructure in the central volume of each specimen is analyzed by μ CT before tensile tests. It is then assessed whether a variation of injection speed, melt and/or mold temperature has an impact on composite's microstructure and Young modulus.

Another challenge for automotive suppliers is to meet the growing demand for use of bio-based materials in parts. In that context, Novares wishes to increase the use of short natural fibers in their composite materials. However, Chapter 1 shows that natural fibers have variable geometrical properties, in particular, thus introducing additional sources of variability in the composite than those related to complex fiber orientations. Thus, in the second part of this chapter, μ CT analyses are performed on PP-30NF specimens to quantify the variability of natural fibers' geometrical properties and orientations (with constant process parameters).

Finally, results allow to establish the origins of Young's modulus variability and highlight a growing uncertainty level (from unreinforced PP matrix to PP reinforced with natural fibers), as exposed in the third part of this chapter.

Injection molded plates and cutting of specimens

In this PhD thesis, 30 wt.% short-natural-fiber-reinforced polypropylene and 35 wt.% short-glass-fiber-reinforced polypropylene (commercial name Thermo l HP F711X99) are studied. For reasons of confidentiality, the type of natural fibers cannot be specified. For both materials, plates of dimensions 200 mm x 140 mm x 5 mm have been injection molded. A fan gate has been used during the injection. A direct consequence is that fibers are oriented in the principal plan and mainly along plate length (Injection Flow Direction, IFD). For PPNF, the same process parameters are always used (see Table 2.1). For PPGF the injection speed, the melt temperature and the mold temperature may vary (see Table 2.1). For both temperature parameters, the software Moldex 3D has been used to determine the extremes according to the recommendations of material suppliers.

	PPNF
Injection time [s]	3.34
Melt temperature [°C]	185
Mold temperature [°C]	50

(a) PPNF process parameters

	Config 1 (reference)	Config 2	Config 3	Config 4	Config 5
Injection time [s]	2.58	2.59	2.55	0.6	4.8
Melt temperature [°C]	210	210	230	210	210
Mold temperature [°C]	50	30	50	50	50

(b) PPGF process parameters

TABLE 2.1: Parameters used during the injection molded process for a) PPNF and b) PPGF

For both materials, three specimen geometries have been cut by water jet into plates. First, quasi-static tensile specimens (ISO527, Figure 2.4) have been cut at four different angles with respect to IFD (0°, 30°, 45° and 90°) and at locations shown in Figure 2.1. Also, the central volume of specimens is scanned (with micro-tomograph) and in the case of PPNF, fibers' geometrical properties and orientation are studied. The different cutting angles allow to highlight the anisotropic tensile behavior of both materials. The second type is dynamic tensile specimens depicted in Figure 2.2, also cut with different angles with respect to IFD (0°, 30°, 45° and 90°). The dimensions of both quasi-static tensile specimens and dynamic tensile specimens are given in Figure 2.4. Finally, the third specimen type is barrel devoted to vibration analysis. It is to note that all barrels are oriented along IFD (see Figure 2.3). Barrels from a same plate are scanned in order to analyze longitudinal and transversal variability of fibers' orientation within the plate.

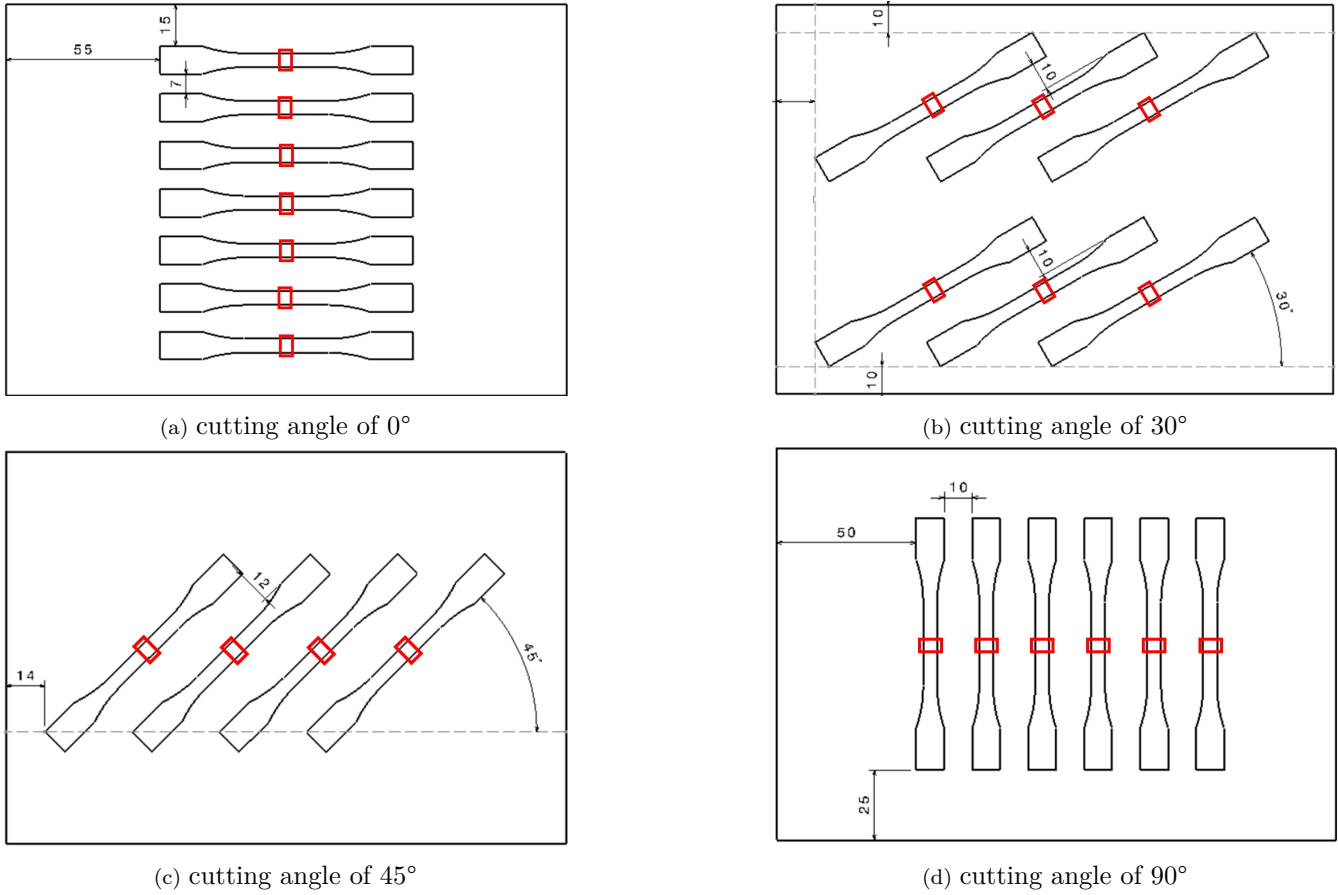


FIGURE 2.1: Orientation of quasi-static tensile specimens, the scanned zones are in red

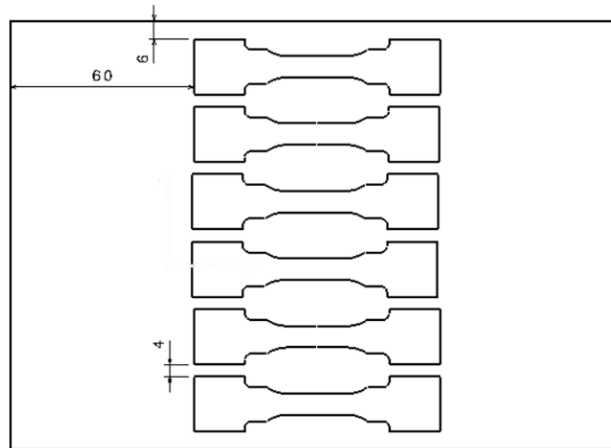


FIGURE 2.2: Example of cutting at 0° of dynamic specimens

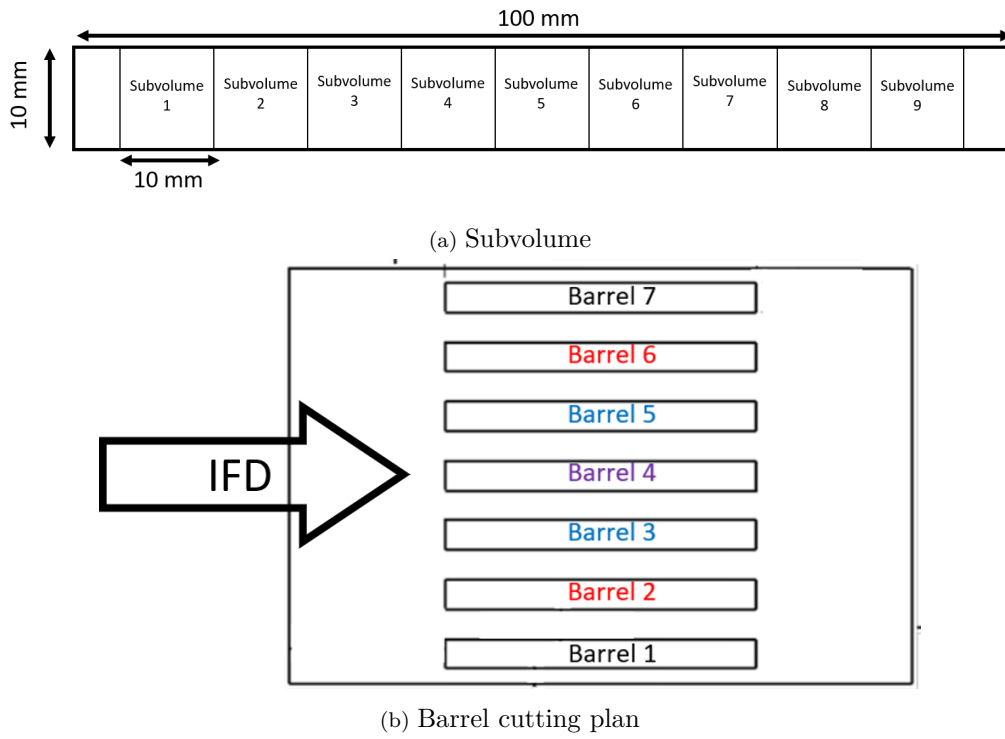


FIGURE 2.3: Specimens for the experimental vibration analysis

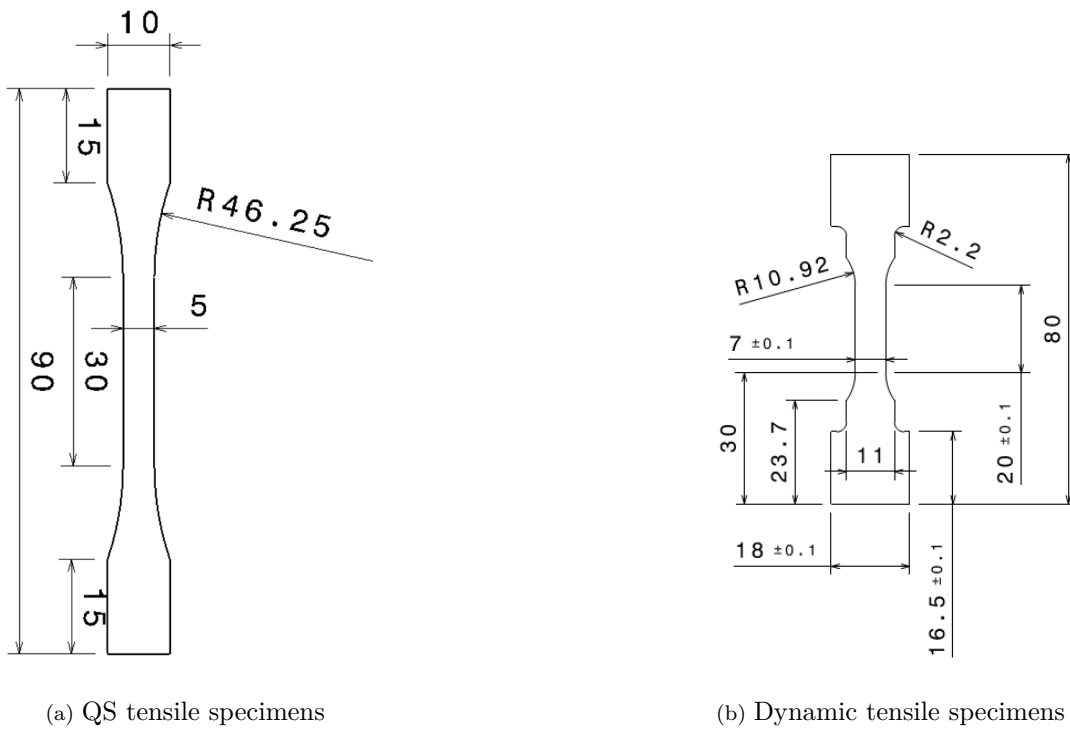


FIGURE 2.4: Dimensions of quasi-static and dynamic tensile specimens

2.1 Effect of process parameters on fiber orientation and Young's modulus of a PP-35GF

The aim of this section is to quantify the impact of variable process parameters on both fibers' orientation inside PP-35GF composite and its Young modulus. To do so, several plates have been injection molded with different process parameters as detailed in Table 2.1. A specimen per plate is then cut, at a constant location, in the center of the plate. Indeed, it has been seen in previous paragraph that fiber orientation vary depending on location on the plate. Studying the impact of process parameters on fiber orientation therefore requires to fix the location of specimen extraction. It is then expected that variable process parameters are the main, nor unique, sources of variability of fibers' orientations. The center of each tensile specimen is first scanned using μ -CT and then each specimen is tested in tension. It is to note that during tensile tests, the loading direction is parallel to the IFD and thus to preferential fibers' orientation. Also, it is important to remind that PP-35GF microstructure is not precisely analyzed because of too high fiber content (see Figure 2.10). Indeed, because of too high density of fibers, it is not possible to isolate each fiber and so on to extract geometrical properties of individual fibers. Thus, a mean orientation is measured from few fibers for each image of the scans instead of a precise measure of each fiber.

In this study, configuration 1 in Table 2.1 is the reference. The mold temperature has been changed for configuration 2, the melt temperature for configuration 3 and the injection time for configuration 4 and 5. The mean orientation for each configuration is plotted in Figure 2.5, with an orientation of 0° corresponding to an orientation along IFD.

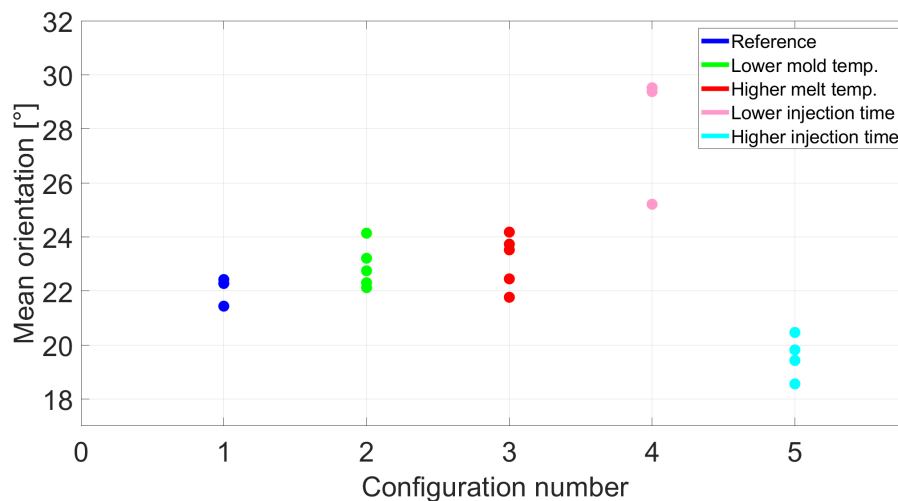


FIGURE 2.5: Mean orientation measured for each configuration

Except for configuration 4 (increased injection speed), few variation of mean orientation are measured for a given configuration. The mean orientation slightly increases for configuration

2 and 3 and more significantly for configuration 4, with respect to reference configuration. Concerning the configuration 4, the increase is justified by the decrease of the injection time (increase injection speed). Indeed, as explained in Section 1.3.1, increasing the injection speed increases the core layer thickness and therefore the proportion of fibers oriented perpendicular to the IFD. Both configuration 2 and 3 have a temperature gradient between the melt and the mold equal to 180°C ($210^{\circ} - 30^{\circ}$ for configuration 2 and $230^{\circ} - 50^{\circ}$ for configuration 3). This gradient impacts the fountain flow and increases the core layer thickness. This translates into an increase of the number of fibers oriented perpendicular to the IFD (i.e. 90°) and thus into an increase of the mean fibers' orientation.

After analysing the variation of glass fibers' orientation according to variable process parameters, the variation of the Young modulus has to be quantified. In view of this, the previously scanned specimens are tested in tension. At least four specimens have been tested for each configuration. Each specimen is tested at the same strain rate, $5.5 \cdot 10^{-3} \text{ s}^{-1}$, and at room temperature. A RUDOLPH ZS16D-50 extensometer has been used to measure tensile specimen elongation with a precision of $3\mu\text{m}$. The nominal axial strain is calculated as the ratio between the axial elongation measured with the extensometer by ROI's initial length of 30 mm and the nominal axial stress is calculated as the ratio between the load and the initial cross-section of the specimens. Young moduli have been calculated following ISO 527-1 norm, that is to say as the slope of the stress-strain curve in the axial strain interval between $\varepsilon_1 = 0.05 \%$ and $\varepsilon_2 = 0.25 \%$. The tensile behavior of specimens of all configurations are plotted in Figure 2.6 and the Young modulus calculated are summarized in Table 2.2.

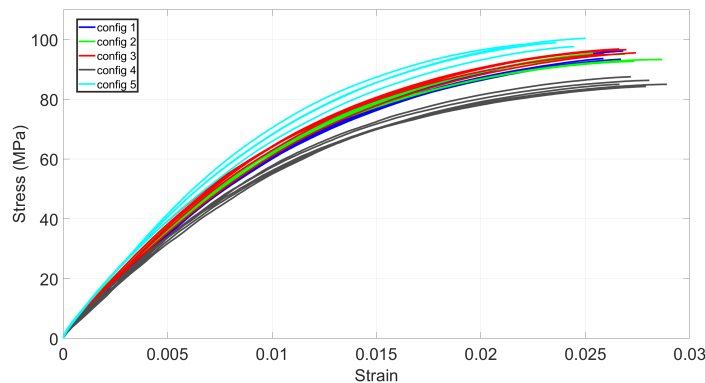


FIGURE 2.6: Results of tensile test for the different configurations

	Config 1 (reference)	Config 2	Config 3	Config 4	Config 5
E [MPa]	7020.9	7253.2	7910.0	6472.3	8026.2
	7110.9	7187.3	7165.8	6637.6	8366.8
	7139.2	7733.5	8334.7	6764.2	8330.7
	7370.6	7491.7	7486.8	6505.6	8080.8
	7124.5	7655.8	7489.4	6715.3	X
Mean E [MPa]	7153	7464	7677	6619	8201
Standard deviation [MPa]	129	240	452	127	172
Coefficient of variation (cov)	1.8%	3.2%	5.9%	1.9%	2.1%

TABLE 2.2: Young' modulus calculated for each different injection molding configurations

For each configuration the Coefficient Of Variation (COV) has been calculated (ratio between standard deviation and average value). Even though the material used for the five configurations is the same, differences are measured for the mean Young modulus, from 6619 MPa for configuration 4 to 8201 MPa for configuration 5, i.e. an increase of almost 25%. As already explained, this increase is due to variation of microstructure of the composite. Indeed, increasing the injection speed (i.e. decreasing the injection time as in configuration 4) increases the thickness of the core layer [35]. As fibers are mainly oriented perpendicular to the IFD in the core layer, the injection molded parts present less fibers oriented parallel to the IFD than parts with lower injection speed, thus explaining the significant difference between Young's modulus. Indeed, reinforcement efficiency of fiber decreased as their orientation with respect to loading direction (here equal to IFD) increases. Range of discrepancy is not the same depending on process configuration. For instance, if considering variation of temperatures, the COV of the Young modulus increases to 3.2% for configuration 2 and up to 5.9% for configuration 3. This variability may be explained by an increased difficulty to maintain the temperature of the mold / melt. On the contrary, the COV measured while changing the injection time is equal to 1.9 % and 2.1% for configuration 4 and 5 respectively which are in the range of the variability of configuration 1 (i.e. 1.8%). Thus, increasing the temperature gradient between the mold and the melt increases the Young modulus of the specimens but also increases its variability. Increasing the injection time significantly increases the tensile properties of specimens but without impacting the variability measured.

Table 2.3 compares the results (mean fibers' orientation, Young modulus) obtained in this subsection for each configuration with the results of the reference configuration.

	Mean orientation	Mean E	Variability of E	other / remark
Config 2 Lower mold temp.	↗	↗	↗	Less energy spent
Config 3 Higher melt temp.	↗	↗	↗	More energy spent
Config 4 Lower injection time	↗↗	↘	=	Increase the injection molding time cycle
Config 5 Higher injection time	↘	↗↗	=	Decrease the injection molding time cycle

TABLE 2.3: Effect of variable parameters on fibers orientation and composites' Young modulus

With this table, it is easy to understand the importance of choosing the right injection parameters to obtain the best compromise. For example, the configuration 5 highly increases the mean Young modulus but decreases the injection molding time cycle. Therefore, production rate is decreased. It is important to note that the increase of the mean orientation for configurations 2 and 3 is a slight increase. Also, the increase of the mean Young modulus could be due to the temperature gradient. The variability of injection parameters is not the only sources of variability for SFRT. In the next section, natural fibers geometrical properties and orientation are measured in the composite. In this case, process parameters are fixed as seen in Table 2.1.

2.2 Natural fibers : variability of geometrical properties and orientation inside the composite

In this section, the geometrical properties of fibers and their orientation inside the central volume (5 mm x 5 mm x 2.5 mm) of quasi-static tensile specimens and barrels are studied using micro-computed tomography. The aim is to measure each fiber individually in order to analyze distributions of fibers' geometrical properties and orientation by using the protocol described in Section 1.4.2. For the QS tensile specimens, different locations have been scanned, according to Figure 2.1. In this way, the variability of fibers' properties along IFD but also along plate width is measured. The repeatability of the results is analysed by measuring the microstructure of 66 specimens from different plates (between 2 and 4 plates). For the barrels, each subvolume of 7 barrels have been scanned (Figure 2.3). Thus the direct evolution of fibers' orientation is measured.

2.2.1 Natural fibers' geometrical properties

As similar trends are observed for the four cutting angles (0° , 30° , 45° and 90°), focus will be put on the quasi-static tensile specimens with a cutting angle of 30° with respect to IFD (6 specimens per plate, see Figure 2.1). Figure 2.7 shows the 18 fibers' length and cross-section distributions obtained in the central volume of six specimens cut into 3 different plates of PPNF.

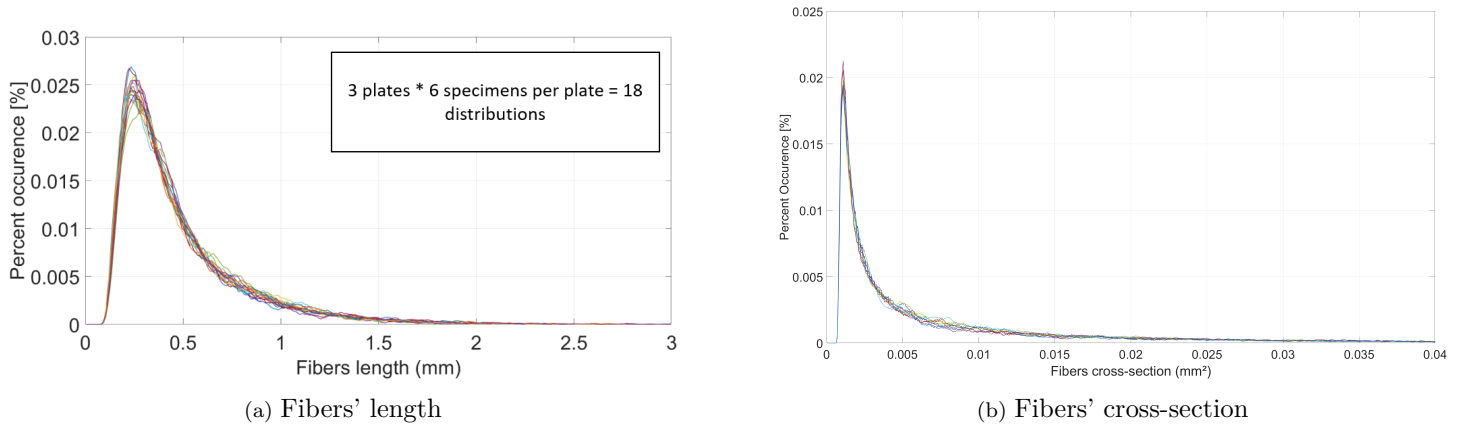


FIGURE 2.7: Fibers geometrical properties distributions for specimens with a 30° cutting angle; dashed lines represent the log-normal distribution used

It can be observed that within a given sample, fibers' length varies significantly, from 0.07 mm to 2 mm. However, similar trends are observed for the distributions obtained in different localizations in a plate, and different plates. The same observations are made with fibers' cross-section.

The impact of fibers geometrical properties, Young modulus and IFSS on average fibers axial stress computed using modified shear-lag model (Equation 1.17) has been studied. Distributions depicted in Figure 2.7 have been used to model the variability of fiber length and cross-section area and values from the literature [141–143] have been used for the Young modulus and for the IFSS. It is important to specify that due to a lack of information in the literature, the value of the IFSS corresponds a different couple of matrix/natural fiber. Four cases are considered, for each case, only one parameter is modified and the value of the 3 others is set to its mean value (reference value). In this computation, fibers' axial strain varies from 0 to 0.1. Fibers axial stress for each set of parameters is plotted in Figure 2.8.

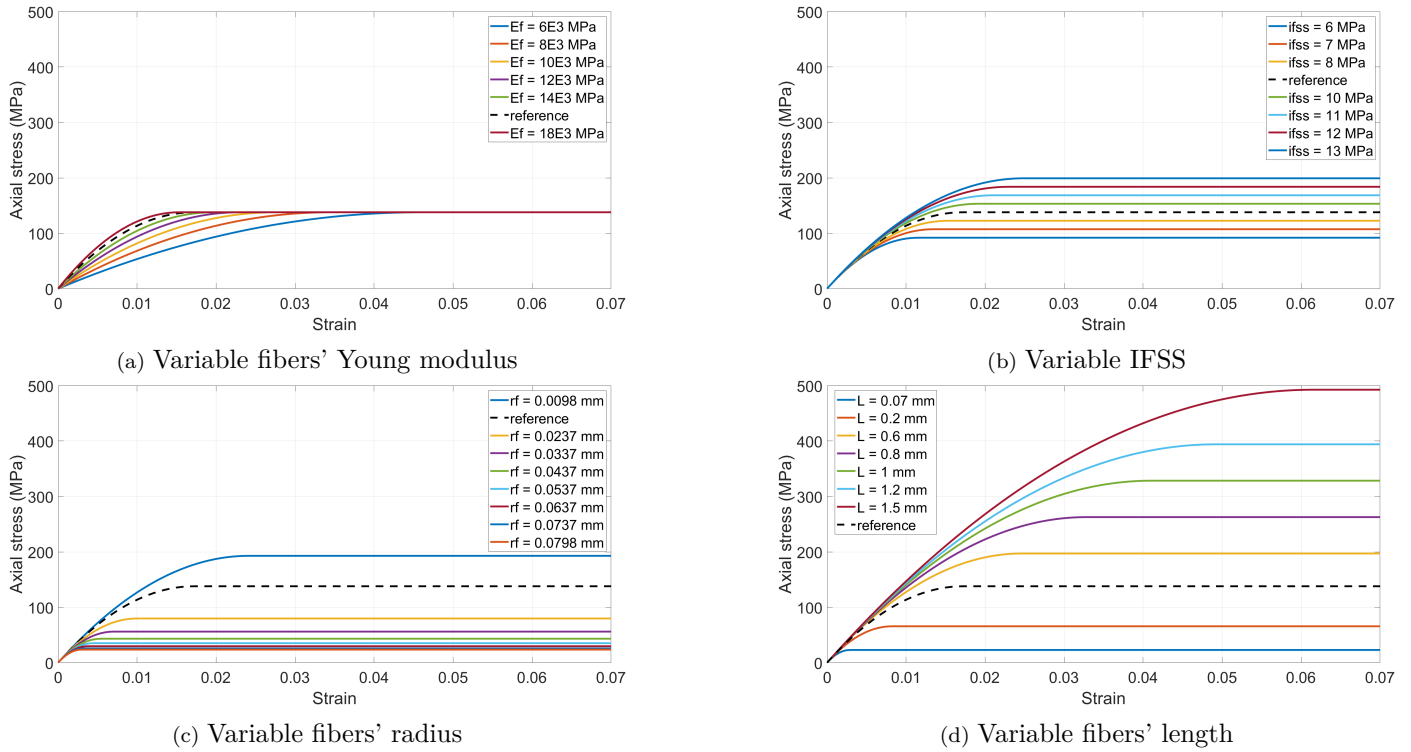


FIGURE 2.8: Effect of variable parameters on fibers' axial stress

With this modelisation of fibers axial stress, one can see that the Young modulus of fibers do not impact fibers maximum axial stress. It is worth reminding that those values of IFSS are maybe not representative of present materials, so its impact on fiber axial stress is shown here for information only. For geometrical parameters, one can see the important variation of fiber maximum axial stress while varying fibers' length or fibers' radius. In the case of fibers' length, fibers maximum axial stress vary from 23 MPa for shorter fibers to 490 MPa for longer fibers, which represent 21.3 times the results obtained for shorter fibers. The length variation between the longest and shortest fibers is $1.5/0.07 = 21.4$. In the case of fibers' radius, fibers maximum axial stress vary from 23 MPa for broader fibers to 193 MPa for thinner fibers which represent 8.4 times the results obtained for broader fibers. The radius variation between the broader and thinner fibers is $0.0798/0.0098 = 8.1$. Thus, one can see that for both geometrical parameters, a variation of A % induces a variation of A % on fibers' maximum axial stress. This study highlights the importance of fibers' geometrical parameters on fibers' axial stress. Thus, mastering the processing of natural fibers may helps to reduce significantly the variability of natural fibers reinforced composites.

2.2.2 Natural fibers' orientation in injection-molded PP-30NF

In this section, natural fibers' orientation in injection-molded composite is measured. As for fibers' geometrical parameters, fibers' orientation has a wide range of variation with the occurrence peak located in the range of cutting angle (here 30°), which confirms that fibers are mainly oriented along IFD. However, by superimposing all distributions obtained, variable orientation distributions are observed from one analyzed volume to another inside a given plate (Figure 2.9). On the contrary, distributions of fibers' orientation obtained in the same cutting zone but in different plates show good repeatability.

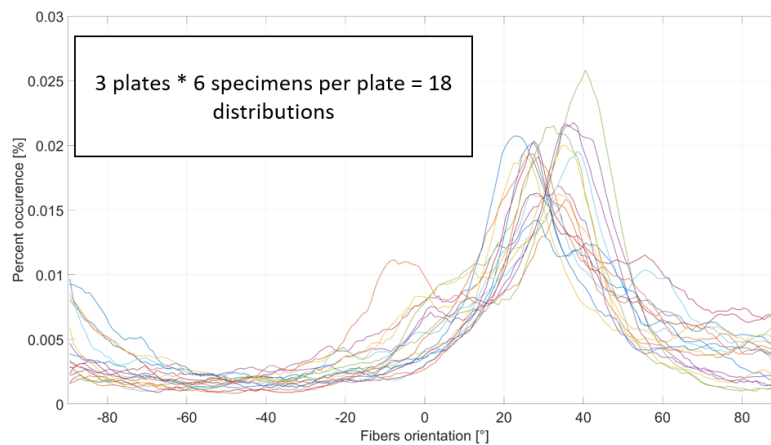


FIGURE 2.9: Fibers' orientation distributions for specimens with a 30° cutting angle

The skin-shell-core structure may be observed with micro-tomograph scans, considering images extracted through the thickness of the specimens (see Figure 2.10). Indeed, random fibers' orientation are measured in the skin layer, fibers orientation mostly parallel to the IFD are measured in the shell layer and mostly transversal to the IFD in the core layer. As explained in Section 1.1.3, this particular structure is directly induced by the injection molding process and more specifically by the fountain flow and the shear flow. It is worth noting that even in case of natural fibers, this particular structure can be observed. Also, as the scale and the size of the six images of Figure 2.10 are the same, the difference of fibers' geometrical properties between PPNF and PPGF is obvious.

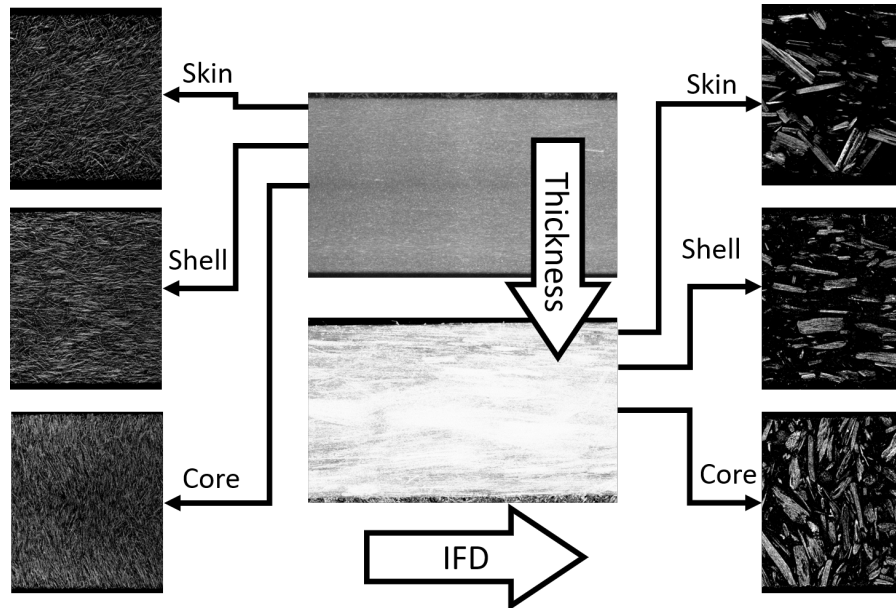


FIGURE 2.10: Skin-shell-core structure through thickness of specimens (left is the PPGF and right is the PPNF)

Fiber orientation in vibration barrels is then analyzed for the PPNF. Figure 2.11 shows fibers' orientation measured in each delimited subvolume of barrel number 3, located near the center of the plate, and barrel number 7, located at the edge of the plate (Figure 2.1). Subvolume 1 is the closest to the injection side and subvolume 9 is the farthest. The peak of maximum occurrence (here near 0°) becomes broader as the distance to the injection side increases. This result means that fibers are more oriented parallelly to the injection flow direction at the end of the plate than near the gate. It is worth noting that barrel number 7 shows distributions with higher occurrence near 0° . The gap between the fibers' orientation distributions from the different sub-volumes is narrowing when compared to the results of barrels number 3. It suggests that fibers' orientation is variable within the IFD but also in the width of the plates.

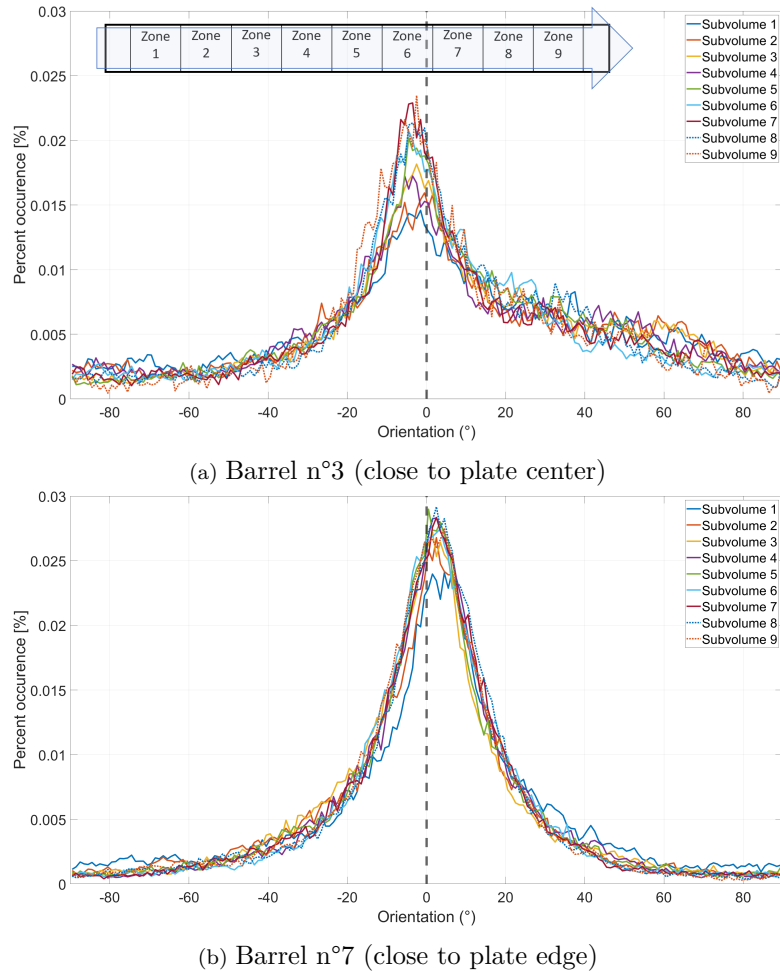


FIGURE 2.11: Fibers' orientation of each subvolume of barrels n°3 and N°7

The previous conclusion is validated when looking at the results for all 7 barrels, see Figure 2.12. Indeed, there is a progressive decrease in fibers' means orientation between the side close to the gate (subvolume 1) and the opposite side. A result related to this observation is that the barrel in which the fibers are least oriented parallel to the IFD is the barrel cut at the center of the plates. Also, a symmetry is observed relatively to the mid-width plane of the plate. Indeed, for example, both barrels cut at the edge of the plate (number 1 and number 7) have similar fibers' orientation. This observation is also valid for barrels number 2 and number 6 and barrels number 3 and number 5.

In this subsection, the variability of natural fibers geometrical properties and orientation has been studied. It has been seen that fibers' geometrical properties have a wide range of variation and also this variation remains quite similar from one tensile specimen to another. On the contrary, fibers orientation is very different from one tensile specimen to another. Transversal variability has been measured with an axial symmetry in the center of the plate. Longitudinal variability has also been measured but without symmetry.

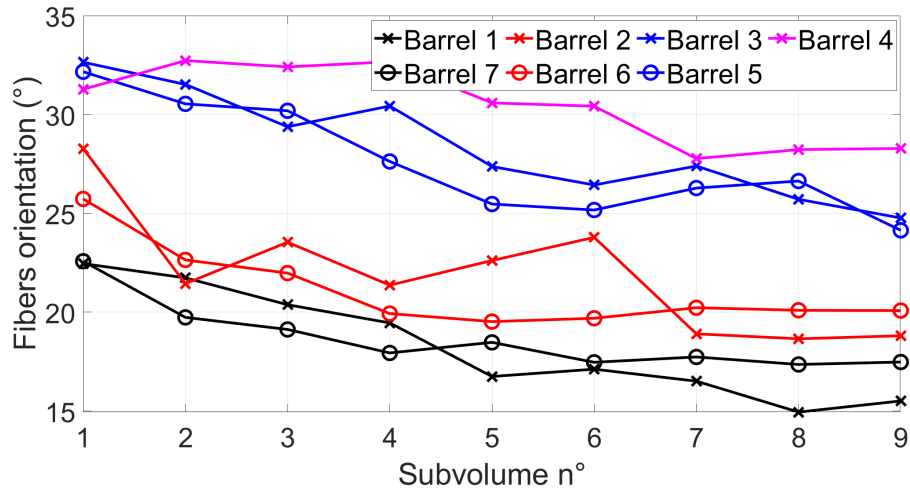


FIGURE 2.12: Mean orientation for all subvolume of each specimen

The next section of this chapter aims to identify the sources of variability for the Young modulus of SFRTs by studying different uncertainty scale.

2.3 Identification of the origins of composite's Young modulus variability

In this section, the variability of materials Young modulus is investigated. In view of this, different levels of uncertainty are defined and their impact on the Young's modulus of the materials is measured. The first level of uncertainty concerns the variation of Young modulus of unreinforced matrices, here two polypropylenes. Addition of glass fibers into PP matrix is then responsible for the second level of uncertainty, related to fiber orientation. Thus, in a first step, the tensile behavior of specimens from different plates but cut in the same cutting area is studied. In a second step, the case of specimens cut from different zones and different plates is studied. It is to note that unless otherwise stated, the loading direction is the same as the IFD (i.e. 0° cutting angle). The last level of uncertainty aims to study the addition of variable geometrical properties on the Young's modulus of composites. In view of this, glass fibers are replaced by natural fibers which present variable length and cross-section. For unbiased comparisons, all tensile tests are performed at the same strain rate, $5.5 \cdot 10^{-3} \text{ s}^{-1}$, at room temperature and several specimens are tested for each configuration. Also, the same optical extensometer has been used for all tensile tests such as the same post-treatment procedure. Young moduli have been calculated following ISO 527-1 norm, that is to say as the slope of the stress-strain curve in the strain interval between $\varepsilon_1 = 0.05 \%$ and $\varepsilon_2 = 0.25 \%$.

Variability of matrices' Young modulus

The first configuration that has been tested is matrix without fibers. In this case, at least three tensile specimens of both matrices have been tested. Results are plotted in Figure 2.13 and the computed Young modulus are summarized in Table 2.4.

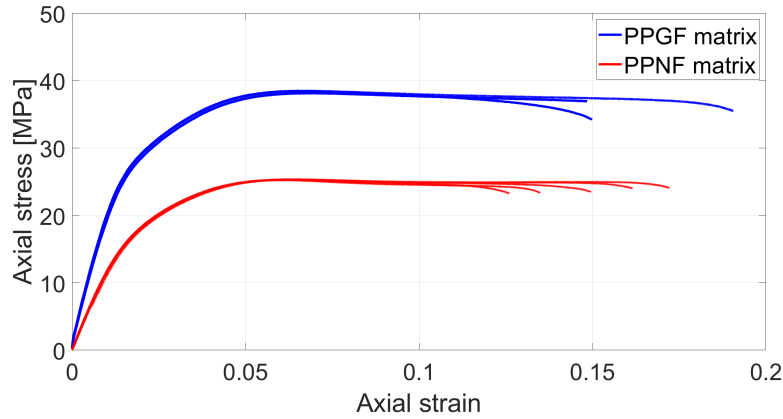


FIGURE 2.13: Three tensile tests for the PPGF matrix and five tensile tests for the PPNF matrix all tested at $5.5 \cdot 10^{-3} \text{ s}^{-1}$

	Matrix of PPGF	Matrix of PPNF
E [MPa]	2072.9	1288.7
	2158.7	1324.2
	2158.4	1248.7
	X	1245.9
	X	1293.4
Mean E [MPa]	2130.0	1280.2
Standard deviation [MPa]	49.6	33.2
Coefficient of variation (cov)	2.3%	2.6%

TABLE 2.4: Young' moduli calculated for each matrix tensile test

The tensile response and the Young moduli measured for both matrices are hardly variable. Indeed, from Table 2.4 one can see that the COV for the modulus is equal to 2.3 % for the matrix of the PPGF and equal to 2.6 % for the matrix of the PPNF.

Variability of PP-35GF's Young modulus

Then, the second stage is the quantification of the variable Young's modulus of glass fiber reinforced polymers. It is to note that all tensile specimens considered hereafter have been cut in plates processed by injection molding, with the same process parameters. Two cases are studied. In the first one, only tensile specimens that have been cut in the same cutting zone (center of each plate) are tested (Figure 2.14a) and in the second one, specimens that have

been cut in different zones are tested. Results are plotted in Figure 2.14 and the Young moduli calculated are summarized in Table 2.5.

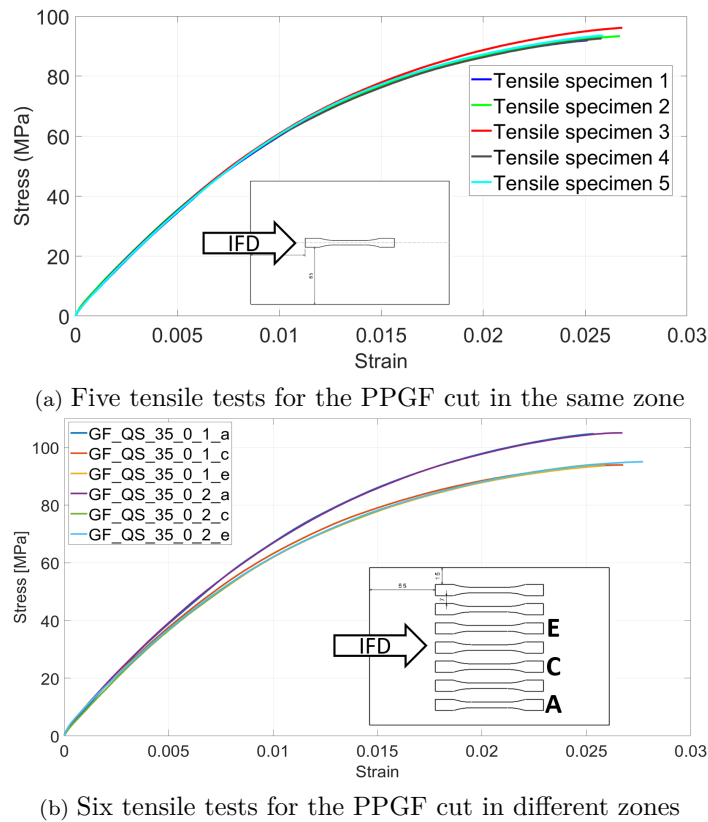


FIGURE 2.14: Tensile behavior of PPGF

	Different plates, same cutting zone	Same plate, different cutting zones
E [MPa]	7020.9	8104.3
	7110.9	7708.5
	7139.2	7550.6
	7370.7	8100.0
	7124.6	7563.6
	X	7416.4
Mean E [MPa]	7153.3	7740.6
Standard deviation [MPa]	129.9	295.1
Coefficient of variation (cov)	1.8%	3.8%

TABLE 2.5: Young' modulus calculated for each PPGF tensile test

By testing specimens cut only in center of plate but in different plates, a COV of 1.8% is calculated for the Young's modulus. On the contrary, the specimens cut in different zones and in the same plate show more variable tensile responses. Indeed, the two specimens cut at the edge of the plates (zone A) show higher Young moduli than the two other zones (C and E, or from zone A). It is to note that in this case, a COV of 3.8% is calculated for the Young's modulus which is twice the variation measured for the case of specimens cut in different plates and in the center of plate. This difference within Young modulus is to be linked with the results

obtained in Section 2.2. By studying the microstructure of the plates, it has been seen that fibers' orientation distributions are different throughout the plates. Tensile specimens that have been cut near the edge of the plates present more fibers oriented parallelly to the IFD resulting in higher Young modulus.

Variability of PP-30NF's Young modulus

In the next step the PP-30NF is studied instead of the PP-35GF. Five tensile specimens from the same plate are tested. Results are plotted in Figure 2.15 and the Young modulus calculated are summarized in Table 2.6.

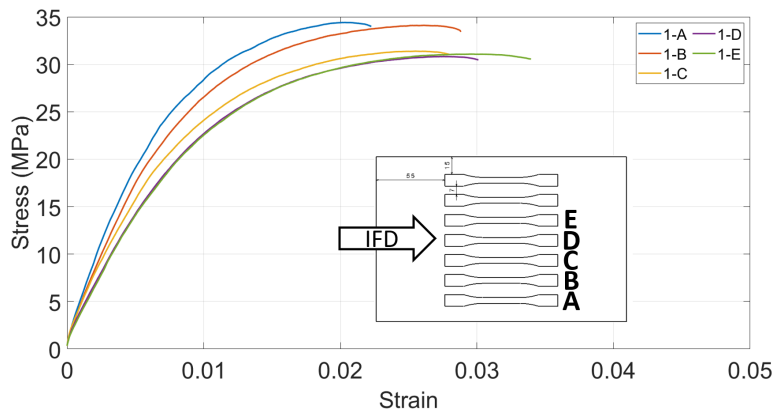


FIGURE 2.15: Tensile tests for the PPNF with same cutting angle

	PPNF
E [MPa]	4047.2
	3534.0
	3145.6
	2752.2
	2742.2
Mean E [MPa]	3244
Standard deviation [MPa]	555
Coefficient of variation (cov)	17.1%

TABLE 2.6: Young' modulus calculated for each PPNF tensile test

First, by comparing Figure 2.15 with Figure 2.14, one can easily see the wide dispersion of results for PPNF. The ultimate tensile strength varies between 30 MPa and 35 MPa, also the Young modulus varies between 2742 MPa and 4047 MPa. The COV calculated for the Young modulus is equal to 17.1%. In comparison with the same configuration but with the short glass fibers (variation of 3.8%), the variation measured is multiplied by more than four. To the variation induced by fibers' orientation distributions is added the variable fibers' geometrical properties. Also, the strain at break is more variable in case of the PPNF than PPGF. For

the PPNF specimens, the strain at break varies from 2.2 % to 3.3 %. On the contrary, for the PPGF the strain at break varies from 2.25 % to 2.77 % (Figure 2.14b). Several aspects of fibers variability may explain this variability. Among them, the nature of the fibers is to be considered. As presented in Section 1.1.1, natural fibers are composed of several elementary fibers glued together by pectic cement. This structure may break and introduce early breakage of the whole composite. It is important to specify that fibers variability is not the only reason for the variability of the strain at break.

Variability of materials' Young modulus regarding different cutting angles

Finally, the last stage compares the variability measured for different cutting angles with respect to the IFD. Both materials are studied here and four cutting angles are considered, 0°, 30°, 45° and 90°. Results are plotted in Figure 2.16 for both materials. The Young modulus calculated are summarized in Tables 2.7 for PPNF and 2.8 for PPGF.

Cutting angle	0°	30°	45°	90°
E [MPa]	4047.2	2959	2261	2260
	3534.0	2480	2009	2081
	3145.6	2448	2081	2231
	2752.2	2388	2613	2113
	2742.2	2551	2264	2118
Mean E [MPa]	3244	2565	2245	2160
Standard deviation [MPa]	555	227	233	79
Coefficient of variation (cov)	17.1%	8.8%	10.4%	3.6%

TABLE 2.7: Young' modulus calculated for each PPNF tensile test with different cutting angles

Cutting angle	0°	30°	45°	90°
E [MPa]	8104.3	5793.7	4971.6	4874.4
	7708.5	5477.0	4437.6	5118.4
	7550.6	5541.9	4530.1	4620.7
	8100.0	5272.5	4438.3	4628.1
	7563.6	5637.4	4687.4	4434.5
	7416.4	X	X	X
Mean E [MPa]	7740.6	5544	4613	4735
Standard deviation [MPa]	295.1	193	224	265
Coefficient of variation (cov)	3.8%	3.4%	4.8%	5.5%

TABLE 2.8: Young' modulus calculated for each PPGF tensile test with different cutting angles

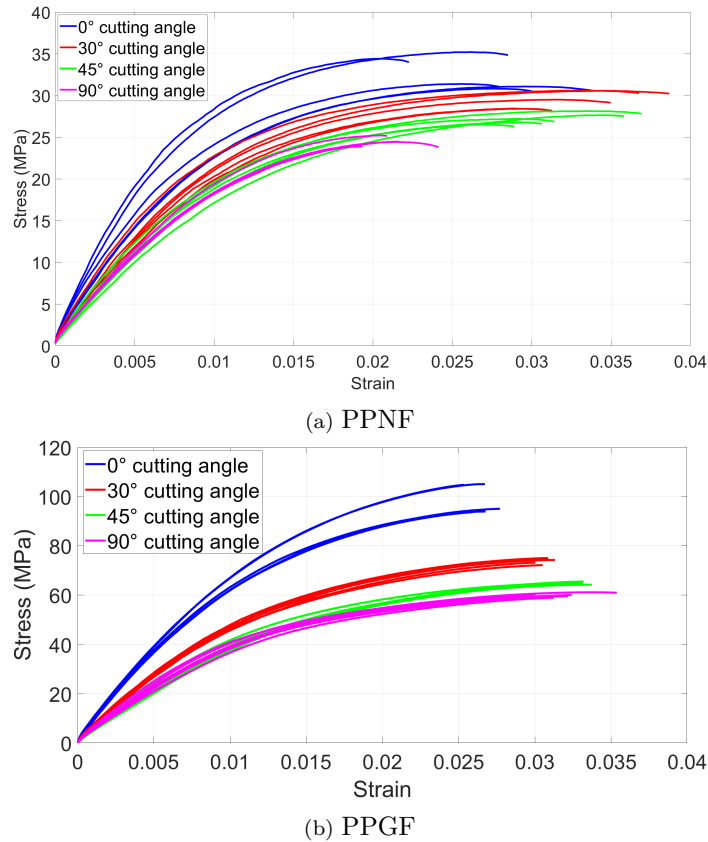


FIGURE 2.16: Results of tensile test at different cutting angles for both materials

For both materials, the results show an obvious decrease of the tensile response of the specimens while increasing their cutting angle. This phenomenon is more visible for the PPGF. In the case of the PPNF, changing the cutting angle from 0° to 90° decreases the average Young's modulus by 35% against 40% for the PPGF. Also, for the PPGF, the COV of their modulus slightly increases while increasing their cutting angle but remains reasonably low (from 3.8 % to 5.5 %, Table 2.8). On the contrary, the COV of PPNF Young modulus significantly decreases while increasing their cutting angle (from 17.1 % to 3.6 %). This is explained by a decrease in the solicitation of the fibers within the composite. Thus, the composite's behavior is less affected by the variable geometrical properties of natural fibers when angle of loading with respect to fiber preferential orientation (IFD) increases.

The variability of SFRT Young's modulus has been studied by progressively increasing the sources of variability. It has been seen that the COV of the Young modulus of the matrix is about 2.5%. Then, by adding glass fibers, the COV is equal to 1.8% for specimens cut in the center of the plates and the COV is equal to 3.8% for specimens cut from different zones of the plate. Finally, by switching to natural fibers, the COV of the young module increases to 17.1%. The variable properties of plant fibers is one of the reasons for this COV increase. As a reminder, with variable injection molding process parameters, the maximum COV measured for the Young modulus of the PPGF is 5.9%. Therefore, this study highlights that the variability

of fiber properties induces more variability on SFRT Young modulus than variable process parameters. Also, in the case of natural fibers, it has been seen that changing the cutting angle and thus fibers orientation with respect to loading direction, decreases the COV of the Young modulus significantly.

2.4 Conclusion

The first part of this chapter is linked to the variability induced by process parameters. It has been seen that the Young modulus is directly induced by fibers orientation which results from the choice of process parameters. Indeed, increasing the melt or mold temperature increases the variability of the Young modulus. Also, it has been seen that the lower the injection speed, the higher the young modulus of the injected part is.

The second part aims to study the variable geometrical properties of natural fibers as well as their orientation inside the composite. Micro-computed tomography has been used to measure fibers' properties. It has been seen that natural fibers' geometrical properties distributions are quite similar from one scanned volume to another and independently of sample' cutting zone. On the contrary, fibers' orientation is more variable. Indeed, this parameter depends on the studied location in an injected plate but remains relatively similar from one plate to another.

Finally, the third part aims to identify the origin of the sources of Young's modulus variability of matrix and composite materials. It has been seen that the addition of GF in PP matrix slightly increases the variability of the Young's modulus of the material. On the contrary, the uses of NF multiply by four Young's modulus COV (compared to PPGF) when the fibers are mostly aligned in the loading direction. This allows to understand the confidence problems of industrials towards the uses of PPNF. Also, it is interesting to note that by increasing the cutting angle of the specimens in the plates, the value of the COV decreases. At industrial part scale, fibers' orientation is usually very different from one area to another (depending on the complexity of part's design and the number of gates etc). Thus the average fibers' orientation at parts' scale may tend towards random orientation, reducing the variability of composite's Young's modulus.

In this chapter, the variability of PP-35GF and PP-30NF Young modulus have been studied because the vibration response is directly induced by the Young modulus. Yet, in the automotive sector, one of the main objective of part design is to ensure that their first natural frequency ranges in an admissible interval. To assess that point, Novares numerically simulates vibration experiments on parts to tune part design, and select the most appropriate material. Reliable and accurate knowledge of material mechanical properties is therefore crucial. It is within this

context that the next chapter aims to first study experimentally the vibration response of both materials and in a second part study numerically their vibration response.

Chapter 3

Vibration response of PP-35GF and PP-30NF

Contents

3.1	Experimental study of PP-35GF and PP-30NF vibration response	67
3.1.1	Results of vibration study	68
3.1.2	Correlation between natural frequency and microstructure	71
3.2	Numerical study of vibration response of PP-35GF and PP-30NF	73
3.3	Conclusions	81

The previous chapter has highlighted the variable Young modulus of SFRT. When designing automotive parts, suppliers must ensure that vibration response, directly governed by Young modulus, meet some requirements. In a first step, it is assessed using numerical simulation of part behavior. It is therefore crucial to dispose of reliable data for materials Young modulus, including eventual range of variation, to predict part behavior with maximal accuracy. Yet, choosing the most relevant Young modulus to model the complex behavior of SFRT is tricky. In order to avoid the early breakage of parts, Novares chooses to use a "protective" method by using a pessimistic modulus for numerical simulations. This strong underestimation of material mechanical properties may then leads to an overestimation of quantity of material needed for a part to meet the specifications or to the addition strengtheners, not always useful. Therefore, it is important to be able to identify more precisely the Young modulus, and especially the range of variation. Thus,

in the first part of this chapter, the variability of the vibration response is studied for both materials and a correlation with their microstructure is investigated. The second part of this chapter aims to compare different modeling strategy by searching the best compromise between easiness and cost of numerical simulation and accuracy of prediction of first natural frequency.

3.1 Experimental study of PP-35GF and PP-30NF vibration response

For both materials, two types of vibration experiments have been performed. For both types of experimentation, the specimens are tested in a clamped-free configuration. Injection-molding plates have been tested using an impact hammer and six accelerometers. Because of the low weight of barrels (dimensions of 100 mm x 10 mm x 2.5 mm), the same experimental set-up can not be used and a non-contact vibration measurement was required. Therefore, the barrels have been tested using a vibration shaker and two lasers vibrometers. The vibration shaker has been set to generate random vibrations on the frequency range [0 - 1000] Hz. In this case, the barrels are tested over a short period of time, thus avoiding self-heating effects. It has been seen in previous section that fibers orientation and composite's Young modulus are different depending on the area studied on the plates. Therefore, plates and barrels have been clamped on one side and then have been reversed. The experimental set-up are depicted in Figure 3.1. Five plates and 21 barrels from three different plates and cut in different locations (see Figure 2.3) have been tested for each material. It is recalled that all barrels have been cut along IFD.

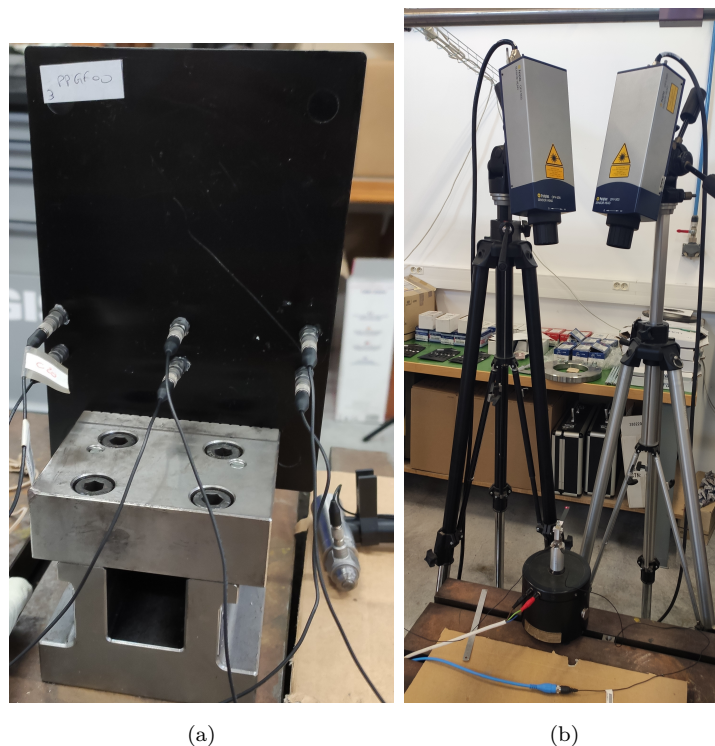


FIGURE 3.1: Experimental set-up (a) for the plates and (b) for the barrels

3.1.1 Results of vibration study

The first part of this section is dedicated to experiments on plates. First natural frequency measured on 5 plates, for both sides of clamping, are summarized in Figure 3.2.

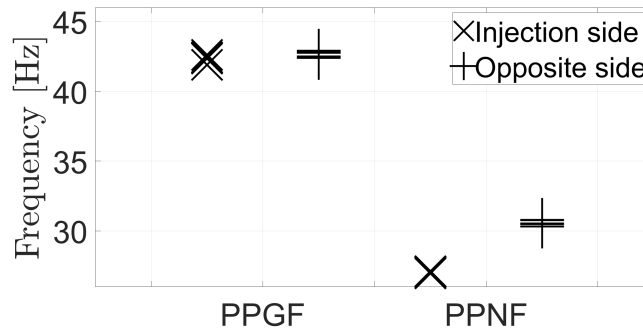


FIGURE 3.2: First natural frequency of whole plates (injection or opposite side refers to clamping edge)

Values of first natural frequency measured for different plates show few variations of only 0.52% (from 26.96 Hz to 27.1 Hz) in case of clamping on injection side against 1.54% (from 30.49 Hz to 30.79 Hz) for the opposite side of PPNF plates and 1.17% (from 41.89 Hz to 42.6 Hz) on the injection side against 1.68% (from 42.4 Hz to 42.9 Hz) for the opposite side of PPGF plates. Then, by comparing the frequencies obtained for a same plate but a different edge of clamping, one can notice higher variations of the frequency for the PPNF. Indeed, for the PPNF, a variation of up to 12% (26.96 Hz for the injection side against 30.49 Hz for the opposite side for plate NF30_1) is measured. On the contrary, for the PPGF, the average variability in this case is equal to 0.83%.

In the following, vibratory tests are carried out on barrels, cut along IFD in different areas of the plates to further investigate the difference between both materials in terms of first natural frequency.

First, in order to evaluate the measurement uncertainty, repeatability tests have been performed on the barrels. This experimental campaign has been spread over two days. Ten barrels have been randomly selected (three from plate one, four from plate two and three from plate three) and each barrel has been tested twice, in exactly the same configuration. Table 3.1 summarizes the results of this campaign in terms of variability between the two tests performed on the same barrel. It can be noted that the aim of this part is to evaluate measurement uncertainty, so only tests with clamping on the injection side were performed. Also, those preliminary tests only concerned PPNF specimens, as this material shows the highest variability of vibratory properties.

PPNF	Measurement uncertainty		
Plate 1	F1 [%]	F2 [%]	F3 [%]
Barrel 1	0.50%	0.48%	0.55%
Barrel 4	0.01%	0.58%	0.75%
Barrel 7	0.05%	0.65%	1.06%
	Measurement uncertainty		
Plate 2	F1 [%]	F2 [%]	F3 [%]
Barrel 1	0.94%	1.05%	0.90%
Barrel 4	0.39%	0.76%	0.83%
Barrel 5	0.88%	1.08%	1.65%
Barrel 7	0.30%	0.48%	0.61%
	Measurement uncertainty		
Plate 3	F1 [%]	F2 [%]	F3 [%]
Barrel 2	1.16%	1.62%	1.83%
Barrel 5	0.88%	0.91%	1.02%
Barrel 7	0.38%	0.39%	0.41%

TABLE 3.1: Measurement uncertainty for the three first natural frequency of PPNF specimens (specimen numbers refer to cutting locations indicated in Figure 2.3)

From Table 3.1, one can see that the maximum measurement variation is lower than 2% (1.86% for the third natural frequency of specimen 2 from plate 3).

First natural frequencies measured for PPNF and PPGF barrels for both localisations of clamping are summarized in Table 3.2.

Plate 1 PPNF	Localisation of clamping		Plate 1 PPGF	Localisation of clamping	
	Injection side	Opposite side		Injection side	Opposite side
Barrel 1	101.79	108.61	Barrel 1	145.85	148.66
Barrel 2	97.92	104.2	Barrel 2	141.95	141.2
Barrel 3	95.59	99.18	Barrel 3	138.34	142.15
Barrel 4	95.26	99.6	Barrel 4	138.15	143.48
Barrel 5	96.15	100.82	Barrel 5	139.8	142.99
Barrel 6	100.54	105.57	Barrel 6	144.09	146.44
Barrel 7	102.22	108.48	Barrel 7	147.28	149.95
Plate 2 PPNF	Localisation of clamping		Plate 2 PPGF	Localisation of clamping	
	Injection side	Opposite side		Injection side	Opposite side
Barrel 1	100	108.27	Barrel 1	144.02	146.83
Barrel 2	97.19	102.27	Barrel 2	140.11	139.19
Barrel 3	95.45	98.07	Barrel 3	135.88	139.6
Barrel 4	95.98	100.21	Barrel 4	136.07	141.89
Barrel 5	99.73	105.01	Barrel 5	136.6	139.97
Barrel 6	100.17	107.05	Barrel 6	141.67	142.1
Barrel 7	95.07	98.5	Barrel 7	148.53	149.8
Plate 3 PPNF	Localisation of clamping		Plate 3 PPGF	Localisation of clamping	
	Injection side	Opposite side		Injection side	Opposite side
Barrel 1	101.57	109.3	Barrel 1	146.13	148.27
Barrel 2	96.33	100.87	Barrel 2	140.51	139.02
Barrel 3	95.35	100.01	Barrel 3	138.6	141.04
Barrel 4	97.1	99.17	Barrel 4	137.05	141.7
Barrel 5	95.76	98.78	Barrel 5	139.2	141.65
Barrel 6	98.44	103.47	Barrel 6	145	144.52
Barrel 7	99.96	105.87	Barrel 7	151.55	153.46

TABLE 3.2: First natural frequencies (in Hertz) obtained for barrels of PPNF and PPGF (specimen numbers refer to cutting locations indicated in Figure 2.3)

For both materials, natural frequency is higher when the specimens are clamped on the opposite side to the injection gate (108.6 Hz on opposite side for specimen NF30 plate 1 specimen 1 against 101.79 Hz on injection side, e.g.). An average of 5% has been calculated for the variability of the first natural frequencies due to the clamping side (hereafter called longitudinal variability) for the PPNF against 1.8% for the PPGF. Also, one can notice the increase of values for specimens that have been cut near the edges of the plates (102.22 Hz for PPNF plate 1 barrel 7, against 95.26 Hz for PPNF plate 1 barrel 4, i.e. in the central part of the plate). An average of 8% variation on the first natural frequency is measured for both materials along the width of the plates (transversal variability). Finally, an average of 3% variation on the first natural frequency is observed when comparing barrels cut at same location but from different plates for PPNF against 1.9% for PPGF (Figure 3.3). The next section aims to link the microstructure of barrels to their first natural frequencies in order to understand the sources of those variabilities.

3.1.2 Correlation between natural frequency and microstructure

In this section, the relation between the micro-structure inside PPNF barrels and their vibration response is studied. First, in terms of variability and then by studying the correlation between fibers' orientation and the first natural frequency measured.

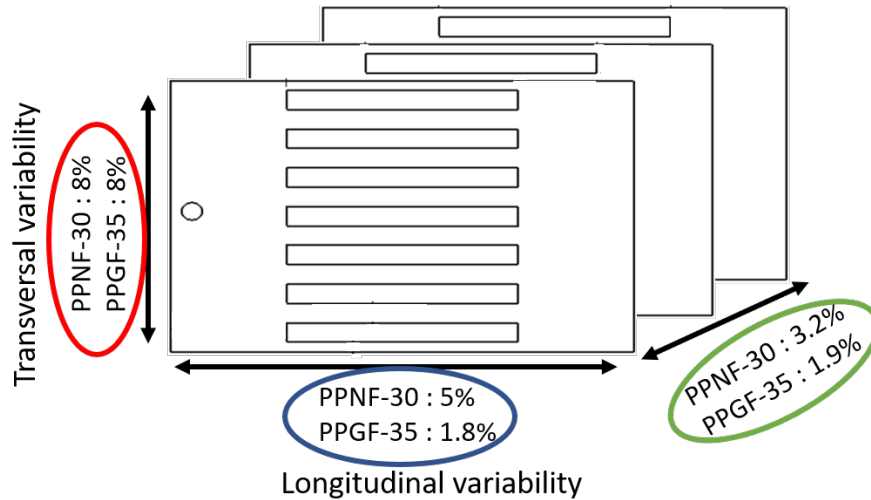


FIGURE 3.3: Origin of the variabilities measured for both materials

Figure 3.3 summarizes the results from Section 3.1.1 in terms of variability of first natural frequency depending on nature of material, location of specimens in the plate or from one plate to another (at same location). The variability measured from one plate to another is in the range of the measurement error for PPGF that seems indicate a good process mastering. The variation is a little bit higher for PPNF that may be explained by higher variation of fibers mechanical and geometrical properties. Then, the transversal variability of 8% may be due to the manufacturing process, here injection molding. This variability has been observed in the literature [11]. Dealing with longitudinal variability, a significant difference between materials has been measured. This difference is likely to be induced by the microstructure of both material. Indeed, as a reminder, natural fibers show different orientations depending on the location along the length of the plate, as highlighted by Figure 2.11. Those differences may explain the variability measured during vibration experiments for PPNF. On the contrary, for PPGF, the measured variability is in the range of the measurement error thus suggesting a significantly reduced orientation variability in this direction at least. Based on literature survey and present analyses, glass fibers generally show lower length than natural fibers (average length of $276 \mu\text{m}$ and varying from $50 \mu\text{m}$ to $600 \mu\text{m}$ for glass fibers [97]). Assuming that a higher length acts against the reorientation of fibers into injection flow direction could explain that natural fibers are less oriented in average along IFD near the gate than at the end of the plate (Figure 2.11), leading to the observed longitudinal variability. At the contrary, shorter glass

fibers are more easily reoriented and no significant variation of orientation along plate length is observed, and therefore no significant longitudinal variability.

In Figure 3.4, the first natural frequency measured for all specimens of PPNF plate 1, for both sides of clamping, is plotted against the average fiber orientation determined by μ -CT in subvolumes one (in case of clamping on the injection side) and nine (clamping at the opposite side), see Figure 2.3. It is indeed assumed that the vibratory response is governed by the material properties near the clamping zone.

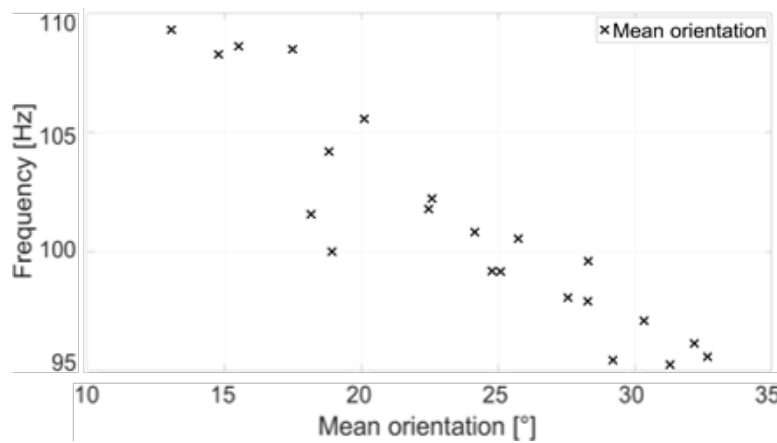


FIGURE 3.4: Mean fibers' orientation versus first natural frequency

One can notice the direct correlation between the mean fibers' orientation and the measured frequency. In particular, the highest frequencies are related to the lowest mean fibers' orientation (recalling that an orientation of 0° means that fibers are oriented along specimen axis, here equal to IFD in all barrels). As shown in Figure 2.11, for PPNF more fibers are oriented parallelly to the IFD in volume 9 (the farrest from injection gate) than in volume 1, resulting in higher first natural frequencies in volume 9 (Table 3.2). It means that the more fibers' are oriented parallelly to the injection flow direction i.e. along barrel length, the higher the first frequency is. On the contrary, the more the angle between fiber and barrel axes increases, the more the first natural frequency decreases. These results highlight the importance of taking into account the true microstructure in the prediction of the vibratory behavior instead of the simple consideration of a cutting angle. In this section, it has been seen that the variabilities measured for fibers properties (mostly fibers' orientation) are propagated to the vibration response of the parts. The next part of this chapter aims to discuss about different numerical strategies to simulate vibration response of injection molded parts.

3.2 Numerical study of vibration response of PP-35GF and PP-30NF

As an automotive supplier, Novares must meet specific customer requirements, such as avoiding some ranges for the first natural frequency of injected parts. To face ever shorter development times and avoid a maximum of experiments, being able to perform accurate numerical simulation of vibratory response is therefore crucial. In addition, numerical simulations must be easy to implement and take as best as possible the specificities of short-fiber reinforced thermoplastic materials into account.

In a fast but simplified approach, Novares engineers consider homogeneous material properties for the whole structure to be tested. More precisely, the lowest Young's modulus given by the supplier in the technical data sheet is selected. This is a pessimistic approach that ensures that material properties are never overestimated. For this research, two Young's modulus are given for both materials (Fig. 3.5).

Modulus E1 (First principal direction)	7.449e+10 (dyne/cm ²)
Modulus E2 (Second principal direction)	4.324e+10 (dyne/cm ²)

(a)

Modulus E1 (First principal direction)	3.249e+10 (dyne/cm ²)
Modulus E2 (Second principal direction)	1.878e+10 (dyne/cm ²)

(b)

FIGURE 3.5: Technical data sheet of (a) PPGF (b) PPNF

The first modulus is the highest modulus expected for this material and represent the case in which fibers are mainly oriented parallel to the loading axis. On the contrary, the second modulus is the most unfavorable modulus and represents the case in which fibers are mainly oriented perpendicular to the loading axis. Thus, for this first approach, the second modulus is considered. The experiments made on barrels are simulated using Abaqus software. The mesh used during the numerical simulations is depicted in Figure 3.6, all elements (C3D8R) have a size of 1 mm x 1 mm x 0.5 mm. Each barrel is successively clamped at the injection side, and then at the opposite side, as it has been done experimentally (1 cm of clamping).

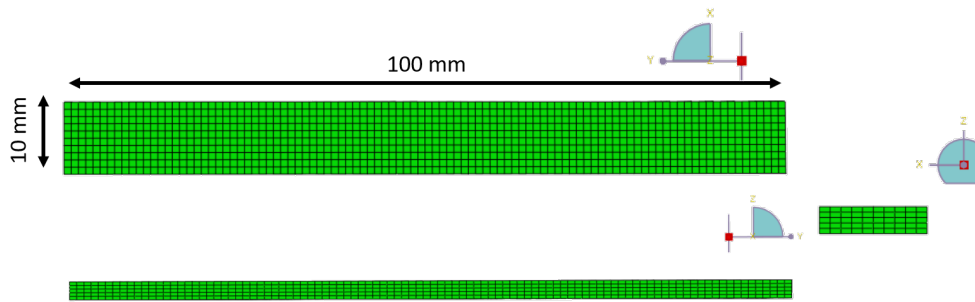


FIGURE 3.6: Mesh used for the numerical simulations

Results are summarized in Table 3.3 and compared to the first natural frequency measured during experiments for both materials with clamping on injection side and opposite side.

	First frequency value [Hz]			Relative error	
	Inj. side experimental	Opp. side experimental	Numerical	Min	Max
PPGF	135.88	153.46	99.45	-26.8%	-35.1%
PPNF	95.26	109.3	70.81	-25.7%	-35.2%

TABLE 3.3: Min and max first natural frequencies obtained during experimental investigation and first natural frequency measured with numerical simulations

As expected for this pessimistic approach, numerical frequencies are very low compared to experimental ones. The relative error has been calculated between the numerical values and values obtained experimentally. They are reduced by 27% and by 26% for the PPGF and PPNF respectively. It is important to note that for both materials, the relative error is quite similar thus showing the safety coefficient induced by this method. This method has the advantages of being easily and quickly carried out. On the other hand, material properties and thus part vibration response are highly underestimated. The Young modulus being homogeneous on whole barrel, the variations observed in previous chapter cannot be modeled. Thus, this method can not model both longitudinal and transversal variabilities of the first natural frequency depicted in Figure 3.3. Nevertheless, in order to meet the requirements of the specifications, the industrial have to increase the stiffness of the parts. It is done by oversizing the dimensions of the part or by ribbing them. Both solutions increase the quantity of material needed during the injection molded process, which increases weight but also cost. Thus, the aim of Novares is to improve the precision of their numerical simulations. In view of this, three different methods are studied with increasing number of sources of variability taken into account. For each method, result accuracy is compared to time cost.

The first method uses the local Young modulus measured during the tensile experimental campaigns. Contrary to the pessimistic method, this protocol allows to take into account a more realistic Young modulus for each materials. The vibration results obtained using Young moduli measured during quasi-static tensile tests performed on 0° cutting angle tensile specimens are

discussed. The second method aims to simulate the injection molding of the plates, with Moldex 3D software, in order to estimate local fibers orientation in the plates. Then the vibration response of a barrel extracted from a numerically injection-molded plate (i.e. with variable local orientation of fibers) is simulated using Abaqus. The third method uses the VUMAT to calculate Young's moduli of each subvolume of the barrels. Then, Young's moduli are associated to their corresponding subvolumes and a whole barrel is simulated.

As explained, the first method re-uses the principle of homogeneous Young's modulus used by Novares to simulate the vibration response of the parts. But, in this case, the Young's moduli used are those calculated during the quasi-static tensile tests at strain rate equal to $5.5 \cdot 10^{-3} \text{ s}^{-1}$ for a cutting angle of 0° . For both materials, results of the first natural frequencies calculated according to the measured Young moduli are summarized in Table 3.4 for both materials. Also, each first natural frequencies calculated with this method are compared to the minimum and maximum values obtained during the experimentations.

	Young modulus [MPa]	1st natural freq. [Hz]	Relative error with respect to	
			Min 1st freq.	Max 1st freq.
PPNF 1	4047	103.84	9.0%	-4.9%
PPNF 2	3534	97.03	1.9%	-11.2%
PPNF 3	3145	91.53	-3.9%	-16.3%
PPNF 4	2752	85.62	-10.1%	-21.7%
PPNF 5	2742	85.47	-10.3%	-21.8%
Mean	3244	93.06	-2.3%	-14.9%

(a) PP-30NF

	Young modulus [MPa]	1st natural freq. [Hz]	Relative error with respect to	
			Min 1st freq.	Max 1st freq.
PPGF 1	7021	126.56	-6.8%	-17.5%
PPGF 2	7111	127.37	-6.2%	-17.0%
PPGF 3	7139	127.63	-6.0%	-16.8%
PPGF 4	7371	129.68	-4.5%	-15.5%
PPGF 5	7125	127.49	-6.2%	-16.9%
Mean	7153	127.75	-5.9%	-16.7%

(b) PP-35GF

TABLE 3.4: Comparison between method 2 results and experimental first natural frequency

In this case, the value of the numerical first frequency is still slightly improved. Indeed, the relative error is on average 20% lower than with the previous method. It is important to note that the specimens used for the Young's modulus measurement have been cut at different positions in the width of the plates but in the same position in the length of the plates. Thus, the increase in the precision of the first natural frequency is due to a better choice of material Young's modulus which allows to better represent the vibratory behavior of the part. This method allows to model only the transversal variability because of the location of tensile

specimens. On the other hand, this method is more time consuming (experimental campaign) and more expensive than current industrial method. However, it should be noted that for this study, finding the solicited area is an easy step (simple geometry and simple experimental set-up), which is not always the case for industrial parts and thus, justifies the use of the pessimistic method.

Concerning the second method, the injection molding of the plate have first been simulated using the software Moldex3D (Figure 3.7). The aim is to calculate local fibers orientation in the injected plate. The same process parameters than during the real injection molding of plates are implemented. The same rheological mesh, validated by a specialist in rheology in Novares' team, is used for the simulation of injection-molded plates for both materials, Figure 3.7.

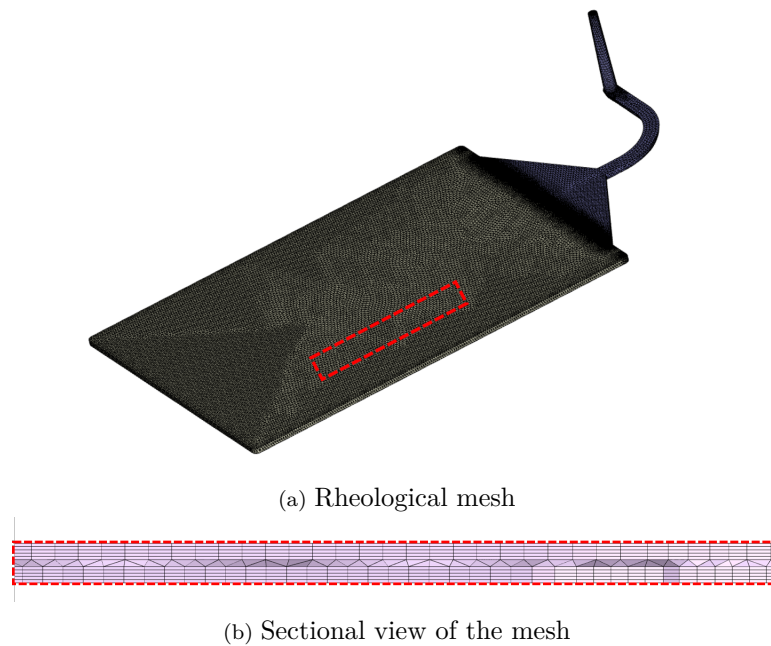


FIGURE 3.7: Moldex3D rheological mesh

Based on the calculated orientation of fibers, the software Moldex3D allows to export the stiffness tensor of each element of the rheological mesh [144, 145]. A mapping option is then used to extrapolate the results to finite element mesh (see Figure 3.8 same mesh parameters than for first FE analysis - Figure 3.6).



FIGURE 3.8: Mesh of the whole plate with barrels' location

The next step is the extraction of the barrels from the injection molded plates. To do so, the software Hypermesh has been used to create one file per barrel according to their cutting zone (Figure 3.8). Finally, the barrels are tested with the same conditions than for the tests using the pessimistic method. Results for both materials are summarized in Table 3.5 and their relative error with respect to experimental first natural frequency are calculated in Table 3.6.

Clamping on	First natural frequency [Hz]			
	Numerical		Experimental (Plate n°1)	
	Injection Side	Opposite side	Injection Side	Opposite side
Barrel 1	111.14	113.93	145.85	148.66
Barrel 2	111.53	113.44	141.95	141.2
Barrel 3	110.89	112.3	138.34	142.15
Barrel 4	112.76	113.12	138.15	143.48
Barrel 5	110.79	112.82	139.8	142.99
Barrel 6	111.14	113.86	144.09	146.44
Barrel 7	113.12	114.23	147.28	149.95

(a) PPGF

Clamping on	First natural frequency [Hz]			
	Numerical		Experimental (Plate n°1)	
	Injection Side	Opposite side	Injection Side	Opposite side
Barrel 1	85.71	89.95	101.79	108.61
Barrel 2	86.19	91.76	97.92	104.2
Barrel 3	88.57	89.67	95.59	99.18
Barrel 4	89.82	90.63	95.26	99.6
Barrel 5	89.51	90.44	96.15	100.82
Barrel 6	86.81	88.76	100.54	105.57
Barrel 7	86.31	89.58	102.22	108.48

(b) PPNF

TABLE 3.5: First natural frequencies obtained for the simulated barrels

	Relative error [%]	
	Injection side	Opposite side
Barrel 1	-10.0	-17.7
Barrel 2	-9.5	-16.0
Barrel 3	-7.0	-17.9
Barrel 4	-5.7	-17.0
Barrel 5	-6.0	-17.3
Barrel 6	-8.9	-18.8
Barrel 7	-9.4	-18.0

(a) PPNF

	Relative error [%]	
	Injection side	Opposite side
Barrel 1	-23.8	-23.3
Barrel 2	-21.4	-19.7
Barrel 3	-19.8	-21.0
Barrel 4	-18.3	-21.2
Barrel 5	-20.7	-21.1
Barrel 6	-22.9	-22.3
Barrel 7	-23.2	-23.8

(b) PPGF

TABLE 3.6: Relative error calculated for the method 2 compared to values obtained during experimentations with clamping on injection and opposite side

For both materials, the results calculated are lower than the results measured during the vibration tests. On the other hand, the results obtained with this method are logically closer to experiments than the results obtained with the pessimistic method. This increase is due to a consideration of the local properties of the material and its anisotropy. Indeed, in this case, composite's mechanical properties are correlated to local fibers' orientation calculated by Moldex3D. Fibers orientation is averaged in each element, thus it is impossible to obtain precise fibers orientation. For comparison, the distribution obtained for the subvolume 1 with Moldex3D is plotted in Figure 3.9.

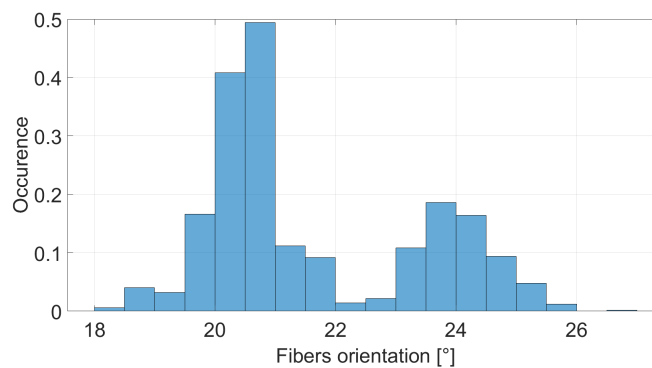


FIGURE 3.9: Histogram of fibers' orientation for the subvolume 1

In this case, fibers orientation is different from fibers' orientation measured in Section 2.2. Indeed, the obtained histogram does not present orientation higher than 30° , this is due to the averaged aspect of fibers' orientation for each element. On the other hand, the mean orientation measured by Moldex3D in the subvolume (i.e. for all element) is equal to 21.63° which is quite similar to the real mean orientation of this subvolume, 22.45° .

Both longitudinal and transversal variabilities of first natural frequency are simulated, but are lower than experimental ones. This difference is induced by the precision of injection molding simulations. Compared to the industrial method, when using Moldex3D to simulate

fibers' orientation, the method becomes more time consuming due to the injection molding simulation.

Finally, the last method concerns the PPNF barrels and uses local information regarding fibers' orientation. Indeed, as explained in Section 2.2.2, 7 barrels cut along IFD in the same plate, themselves divided in 9 subvolumes along their length have been scanned. Thus, fibers' orientation, length and cross-section into each subvolume have been measured. A local Young's modulus for each sub-volume is calculated using our VUMAT and considering local microstructure information (see Table 3.7). Again, the norm ISO 527-1 is used to calculate Young's moduli as the slope of the stress-strain curve in the strain interval between $\varepsilon_1 = 0.05$ % and $\varepsilon_2 = 0.25$ %.

	Young's modulus [MPa]
Subvolume 1	3352
Subvolume 2	3383
Subvolume 3	3408
Subvolume 4	3335
Subvolume 5	3469
Subvolume 6	3425
Subvolume 7	3467
Subvolume 8	3561
Subvolume 9	3540

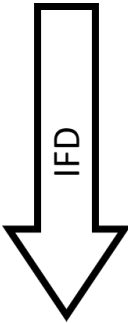


TABLE 3.7: Young's modulus calculated for each sub-volume for barrel 1

In simulation of barrel vibratory response, a different Young modulus is input in each subvolume 1 to 9, according to Table 3.7. Simulations of vibration tests are performed for both sides of clamping, similarly to experiments. The same mesh and the same conditions used with the pessimistic method are applied. Results are summarized in Table 3.8. In this Table, focus is made on barrel 1 from plate 1 because this barrel presents the most difference for first natural frequency between injection and opposite side.

Clamped on	Injection side	Opposite side
Experimental	101.79 Hz	108.61 Hz
Numerical	102.2 Hz	106.07 Hz
Relative error	0.4%	-2.3%

TABLE 3.8: First natural frequency for PP-30NF barrel number 1, comparison between numerical and experimental values

This method improves the prediction of the first frequency thanks to the uses of microstructural data. Indeed, with this method, the relative error is down to 0.4% for the injection side against 26.8% for the pessimistic protocol. The main problem of this method is the time spend for the determination of microstructural information (here fibers' orientation). In the previous

chapter, it has been seen that fibers' orientation depends on the type of fibers but also for process parameters. Thus, in order to use this method with different materials, a microstructural study must be done for each material and for each zone of interest of parts. This method is not applicable by Novares because it would require them to invest too many resources. Nevertheless, this study is important because it allows Novares to show their customers that it is possible to obtain very precise correlations between experimental results and numerical predictions.

Then, in order to reduce the resources needed, a mix between this method and the industrial method has been considered. That is to say, the Young modulus calculated for the closest subvolume to clamping location (i.e. subvolume 1 or 9 for clamping in injection or opposite side, respectively) are applied to the whole barrel to consider an homogeneous Young modulus (see Table 3.7). As a reminder, fibers' orientation distributions of both subvolume are plotted in Figure 2.11.

	Young modulus	First natural frequency	Experimental results	Relative error
Subvolume 1	3352 MPa	94.5 Hz	101.79 Hz	-7.2%
Subvolume 9	3540 MPa	97.2 Hz	108.61 Hz	-10.5%

TABLE 3.9: Homogeneous method mixed VUMAT method

One can see that these results are lower than experimental results but they are still more accurate than the results obtained with the pessimistic method. Also, using fibers' orientation of only one subvolume allows to drastically reduce the time required for the implementation of previous method because it requires less information about the micro-structure and thus fewer scans.

The Figure 3.10 schematically represent the time cost of each method compared to the accuracy of predicted vibratory properties. This schematic representation helps Novares to define their modeling strategy according to their expectations and development phases.

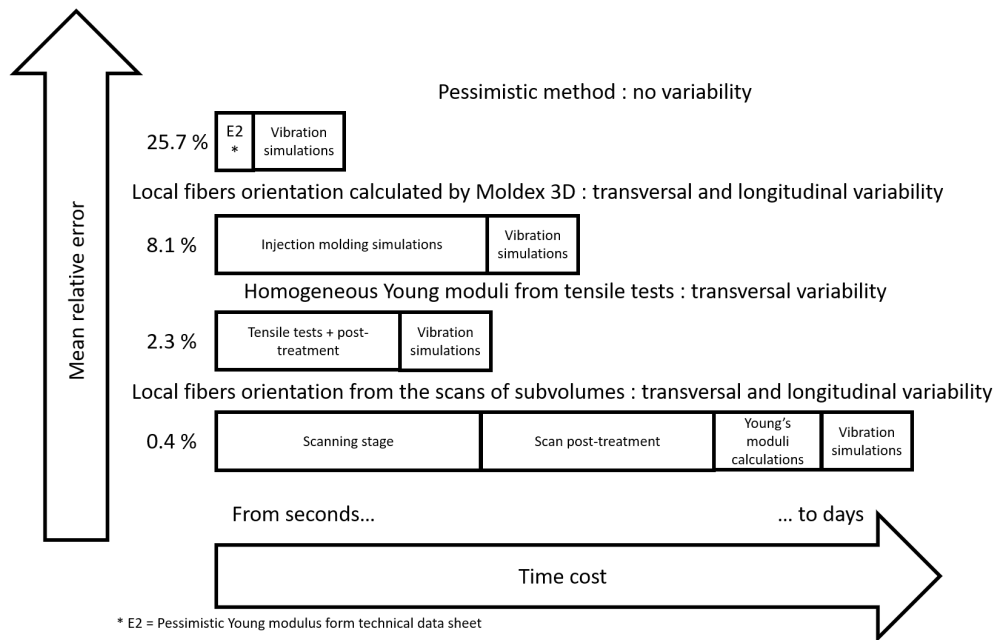


FIGURE 3.10: Schematic representation of the time cost of each method compared to their precision

3.3 Conclusions

In this chapter, the vibration response of SFRT has been studied. In view of this, the first part of this chapter has highlighted the variability of the vibration response of both PP-35GF and PP-30NF. The results from the experimental campaign show longitudinal and also transversal variability. This result is directly linked to the variability of the Young modulus and, in case of PP-30NF, to fibers' orientation measured in Chapter 2.2.2. Indeed, a direct correlation between first natural frequency and fibers' mean orientation has been pointed out. This variability is a problem for the choice of the Young modulus associated to the studied material. Indeed, the quality of the numerical prediction therefore depends on the knowledge of local material properties in a given part.

In the second part of this chapter, different methods for the simulation of the vibration response of barrels are discussed. It is shown that it is possible to obtain accurate numerical predictions but at the expense of experimental and/or numerical cost.

Thus, in this section the vibration response of SFRT and different modeling strategies have been studied. However, the vibration response is not the only behavior studied by car manufacturers. Indeed, in case of vehicle impact, Novares must guarantee the integrity of its parts even in extreme loading cases. In view of this, car manufacturers must master the dynamic behavior of materials and failure. That is why the following chapter aims to study

the modeling SFRTs using the VUMAT presented in Chapter 1.4.1 and then experimentally study SFRTs failure behavior.

Mechanical response of SFRT under high-strain-rate loading

Contents

4.1	Characterization of mechanical behaviors	86
4.1.1	Viscoelastic parameters of matrix materials	86
4.1.2	Viscoplastic parameters of matrix materials	90
4.1.3	Fibers and matrix / fiber interface parameters	96
4.1.4	Model validation	103
4.2	Investigation of SFRT's failure behavior	104
4.2.1	Failure of notched tensile specimens	106
4.2.2	SFRT's failure behavior during bulge tests	111
4.3	Towards a failure criterion	115
4.4	Conclusion	124

In the previous chapter, the variability of the vibration response of SFRT has been studied regarding the variability of fibers' orientation. It has been seen that results from numerical simulation may be more or less accurate depending on the level of details in modeling of fiber orientation variation/discrepancy.

However, vibration behavior is not the only issue encountered by automotive manufacturers. Indeed, in a vehicle crash, it is imperative that neither debris nor part of a vehicle component is lost and hits users. To achieve this, automotive suppliers must study the behavior of SFRT under high-strain-rate loading until failure to

predict the weakest zones of injection molded parts. Thus, in order to study the behavior of SFRT under high-strain-rate loading, it is necessary to investigate the viscoplastic behavior of SFRT and also the damage phenomena that can lead to part failure.

As a reminder, it has been seen in chapter 2 that SFRT's viscoelastic behavior is mainly governed by fibers orientation. This observation is also valid for the viscoplastic behavior, Figure 4.1.

Also, it is important to note that the strain-rate sensitivity of SFRT is mainly

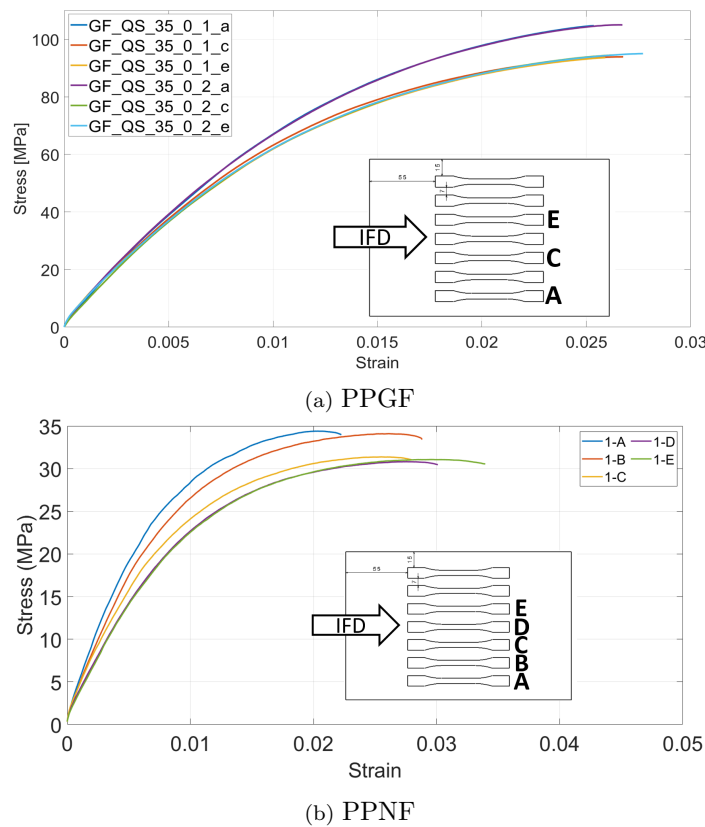


FIGURE 4.1: Tensile behavior of PPGF and PPNF

governed by that of the matrix and therefore decreases when fibers are mainly oriented parallel to the loading direction. The strain at break, and thus failure, is even more variable, and especially for the PPNF. By nature, the failure is directly governed by the microstructure properties. If the macroscopic VE/VP behavior of the SFRT can be globally predicted by microstructure properties averaged over a certain volume, rupture initiation is on the contrary directly dependent of local properties. Indeed, a local defect, a fibers bundle or a bad placement of a fiber regarding the loading direction can be sources of breakage initiation in the part. Thus, it is essential to control the microstructure of the SFRT in order to predict the failure zone.

Thus, after characterization of both materials VE-VP behavior, the aim of this

chapter is to present a first step of implementation of a failure criterion. Different damage mechanisms that may lead to rupture are examined. It has been seen that the most prevalent damage mechanism is matrix / fiber debonding. Thus the criterion is based on the damage coming from the matrix / fiber decohesion. The identification of the criterion is made with tensile tests on notched specimens and its accuracy is assessed with bulge tests.

4.1 Characterization of mechanical behaviors

4.1.1 Viscoelastic parameters of matrix materials

In order to predict the behavior of both materials, model parameters need to be identified. In the model proposed (see Chapter 1.4.1) SFRTs behavior is described by both matrix behavior and fibers characteristics (orientation, geometry,...). The first step therefore consists in the characterization of viscoelastic and viscoplastic behavior of matrix materials (PP).

Viscoelastic behavior is characterised by Dynamic Mechanical Analyses (DMA) for both matrices of PPNF and PPGF. A DISCOVERY DMA 850 is used with rectangular specimens (60 mm x 12 mm x 2.5 mm). A 3-Point bending test is performed with an imposed oscillating displacement of amplitude 40 μm , variable frequency and with a force equal to 2N. Thus, the expression of the imposed strain $\varepsilon(t)$ is given by :

$$\varepsilon(t) = \varepsilon_0 \cos(\omega t) = \varepsilon_0 R\{\exp(i\omega t)\} \quad (4.1)$$

with ω the angular frequency and ε_0 the strain amplitude.

During the DMA, the frequency of the oscillating displacement is progressively increased from 0.01 Hz to 150 Hz (see Table 4.1). The tests have been performed at room temperature.

Frequency (Hz)
0.01
0.05
0.1
0.5
1
2
5
10
25
50
75
100
150

TABLE 4.1: Frequency used during the DMA

First, let's remind the expression of the viscoelastic modulus using Generalised Maxwell model (see Chapter 1.4.1):

$$E(t) = E_{\infty} + \sum_{i=1}^N E_i(t) \exp\left(\frac{-t}{\tau_i}\right) \quad (4.2)$$

with E_{∞} the infinite modulus, E_i the time dependant moduli and τ_i characteristic times for each branch i . In order to extract the rigidity (or time dependant moduli) and the characteristic time (or relaxation time) of each Maxwell element, a complex modulus is calculated from the ratio between stress and strain measured during the DMA. This complex modulus is divided into an imaginary part, the loss modulus, and a real part, the storage modulus.

$$E^{\text{complex}} = E^{\text{storage}} + iE^{\text{loss}} \quad (4.3)$$

with:

$$\begin{aligned} E^{\text{storage}} &= \frac{\sigma_0}{\varepsilon_0} \cos(\delta) \\ E^{\text{loss}} &= \frac{\sigma_0}{\varepsilon_0} \sin(\delta) \\ \tan(\delta) &= \frac{E^{\text{loss}}}{E^{\text{storage}}} \end{aligned} \quad (4.4)$$

in which the parameter δ is the loss angle. The expression of the complex modulus is given by:

$$E^{\text{complex}}(\omega) = i\omega \int_0^{\infty} E(t) \exp(-i\omega t) dt \quad (4.5)$$

Then, with the expression of $E(t)$, given in Equation 4.2, the expression of the complex modulus is given by:

$$E^{\text{complex}}(\omega) = E_{\infty} + \sum_{i=1}^N E_i \frac{(\omega\tau_i)^2}{1 + (\omega\tau_i)^2} + i \sum_{i=1}^N E_i \frac{\omega\tau_i}{1 + (\omega\tau_i)^2} \quad (4.6)$$

by identification with the Equation 4.3, the storage modulus is expressed by:

$$E^{\text{storage}}(\omega) = E_{\infty} + \sum_{i=1}^N E_i \frac{(\omega\tau_i)^2}{1 + (\omega\tau_i)^2} \quad (4.7)$$

and the loss modulus by:

$$E^{\text{loss}}(\omega) = \sum_{i=1}^N E_i \frac{\omega\tau_i}{1 + (\omega\tau_i)^2} \quad (4.8)$$

Finally, the values of the relaxation times τ_i are fixed thus allowing to find the values of the time dependant moduli E_i by solving the following least square minimization:

$$\min_{E_i} \sum_{j=1}^M \left[\left(\frac{E^{storage}(\omega_j, E_j)}{E_j^{exp,storage}(\omega_j, E_j)} - 1 \right)^2 + \left(\frac{E^{loss}(\omega_j)}{E_j^{exp,loss}(\omega_j)} - 1 \right)^2 \right] \quad (4.9)$$

where M is the number of frequency imposed during the DMA tests and E_j^{exp} are values measured at the frequency ω_j .

In the present study, the viscoelastic model is composed of seven Maxwell elements. The results of the identification for both materials are summarized in Table 4.2. Also, Figures 4.2 and 4.3 compare the storage and loss moduli identified for both materials with the measured values during DMA tests.

E_i [MPa]	τ_i [s]	E_i [MPa]	τ_i [s]
440.89	1000	581.54	1000
181.51	100	276.52	100
156.41	10	205.29	10
103.63	1	135.58	1
77.69	0.1	110.089	0.1
70.3	0.01	116.85	0.01
118.46	0.001	218.82	0.001
E_∞ [MPa]	726.3	E_∞ [MPa]	895.66
(a) Matrix of PPNF		(b) Matrix of PPGF	

TABLE 4.2: Identified viscoelastic parameters for both matrices

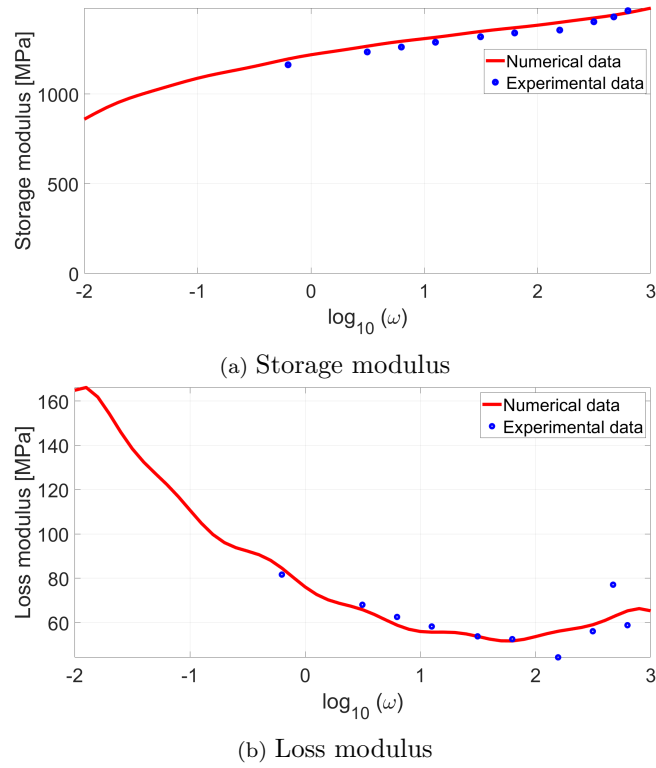


FIGURE 4.2: Results of the DMA for the matrix of PPNF

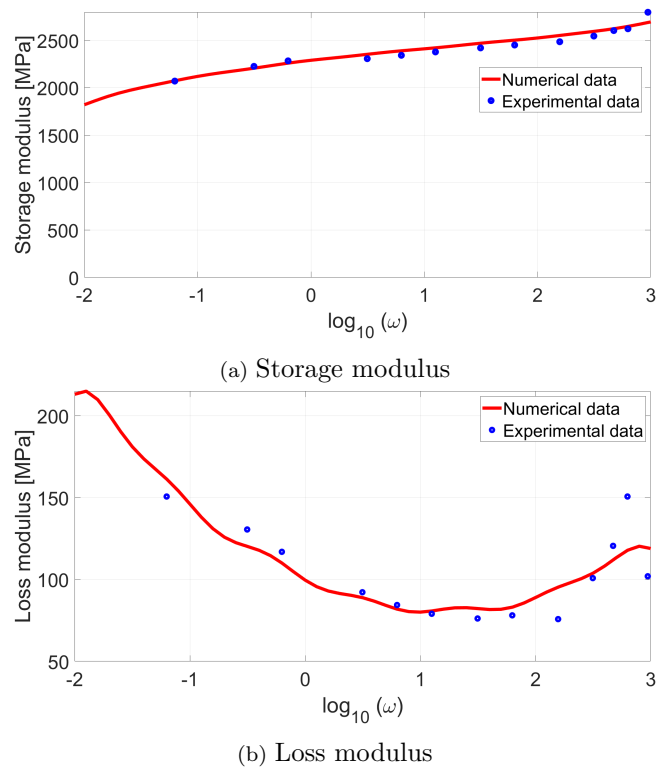


FIGURE 4.3: Results of the DMA for the matrix of PPGF

The next step is the determination of the viscoplastic parameters.

4.1.2 Viscoplastic parameters of matrix materials

In this section, viscoplastic parameters in the hardening law and viscoplastic correction (Equation 1.10) are characterized for both PP matrices. Monotonic tensile tests are performed at different strain rates, see Table 4.3. Two tensile devices have been used, an Instron E3000 with a 3kN cell force for the quasi-static tests (strain rate of $5.55 \cdot 10^{-4} \text{ s}^{-1}$ and $5.55 \cdot 10^{-3} \text{ s}^{-1}$) and an Instron 65/20 hydraulic jack for the dynamic tests (strain rate of 0.5, 5 and 50 s^{-1}). Figure 4.4 details the geometry of both tensile specimens used. The quasi-static tensile specimens geometry follows ISO527 norm. In the case of dynamic tests, to prevent specimen loading as long as imposed test velocity is not reached, the LAMIH has developed a specific set-up. Therefore, dynamic tensile specimens geometry is designed for this specific set-up. Tensile specimens are painted with a black and white speckle pattern. The Region Of Interest (ROI) is divided into several facets that are tracked using DIC. High-speed cameras are used to record each tensile test. Information concerning the camera frame rate are listed in Table 4.3.

Speed test [$\text{mm}\cdot\text{s}^{-1}$]	Strain rate [s^{-1}]	Camera frame rate [ips]
0.0167	$5.55 \cdot 10^{-4}$	0.2
0.167	$5.55 \cdot 10^{-3}$	2
10	0.5	600
100	5	6000
1000	50	30000

TABLE 4.3: Strain rate and camera frame rate

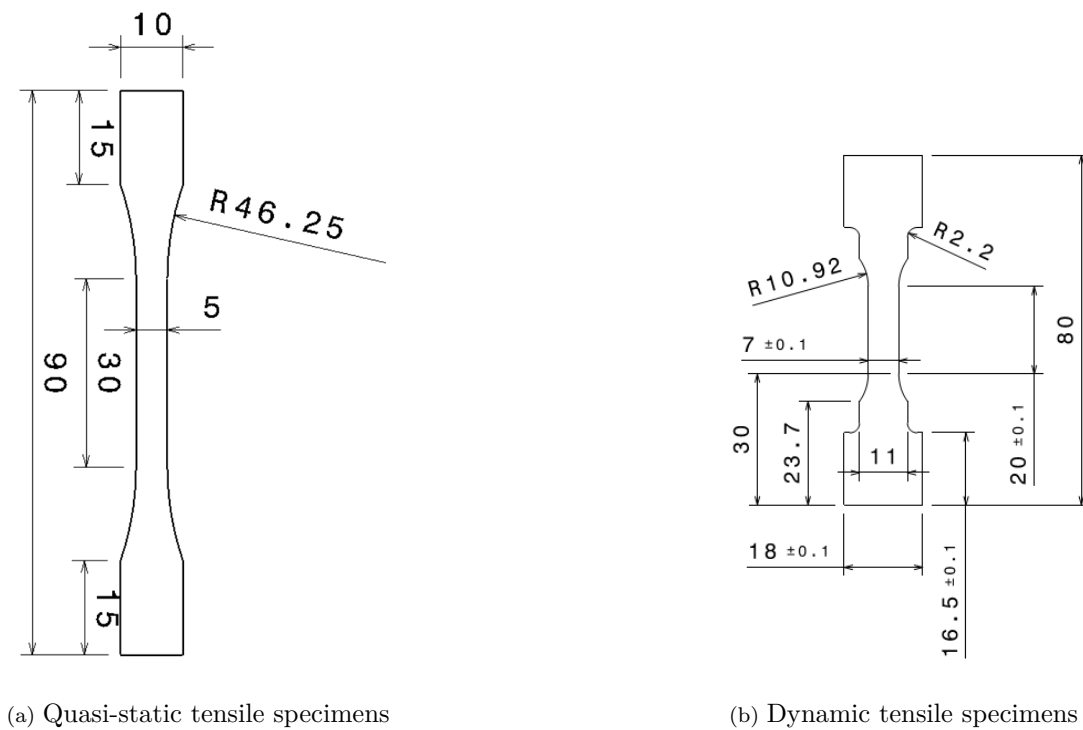


FIGURE 4.4: Tensile specimens geometry

For each tensile test, the ROI (height of 30 mm and 20 mm for quasi-static and dynamic specimens, respectively) is divided into facets to determine the local strain and local strain rate. Two different sizes of facets have been used, depending on the geometry of tensile specimens (15 x 15 pixels for dynamic tensile specimens and 29 x 29 pixels for QS tensile specimens). The nominal axial stress is computed by $\sigma = F/S_0$, with F the load measured by the cell force and S_0 the initial cross-section measured in the center of the ROI. By nature, the value of the nominal axial stress is the same in all facets over the ROI. Results are plotted in Figure 4.5. The strain-rate dependency of both matrices can be seen with a decreased strain at break and an increased rigidity when the strain rate increases.

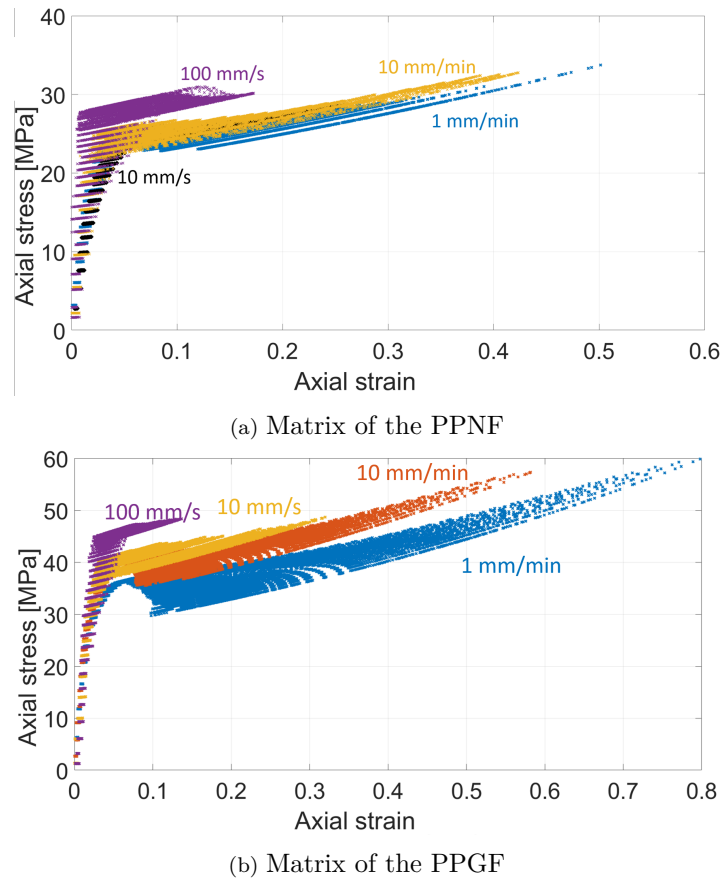
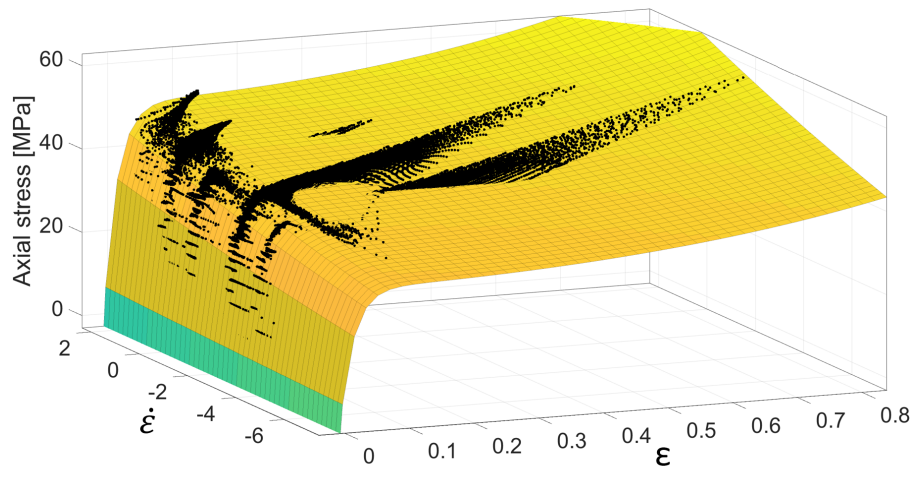


FIGURE 4.5: Mechanical behavior of both matrices measured by DIC

The value of the initial yield stress in tension σ_T is directly taken from the tensile behaviour curves, as the value of nominal stress from which the curve becomes non linear. In the case of the matrix of the PPGF, its value is equal to 8 MPa and 7 MPa for the the matrix of the PPNF. Then, DIC results can be exploited to characterized the viscoplastic behavior, using the $SE\dot{E}$ method, developed by Lauro et al. [146]. It is to note that this approach allows to take advantage of the non-homogeneity of the strain and strain rate over the ROI to enrich the identification process. With this method, the nominal stress, the local axial strain and the local strain rate are used to plot the material mechanical behavior. The fit of the $SE\dot{E}$ surface with the Equation 1.8 (see Figure 4.6) is performed using the curve fitting application of Matlab (sftool). It is done by fixing the value of $\dot{\kappa}_0$ equal to the lower strain rate imposed during experimental campaign and by fixing the value of σ_T . The values of the coefficients h_1 , h_2 , h_3 and m are determined and their values are summarized in Table 4.4.

FIGURE 4.6: Behavior laws obtained with the $SE\dot{E}$ method for the matrix of the PPGF

Parameters	Matrix of PPGF	Matrix of PPNF
σ_T [MPa]	8	7
h_1 [MPa]	23.35	9.97
h_2	0.338	1.104
h_3	47.92	60.88
m	0.021	0.039
$\dot{\kappa}_0$ [s^{-1}]	$5.5 \cdot 10^{-4}$	$5.5 \cdot 10^{-4}$

TABLE 4.4: Viscoplastic parameters

The pressure dependency parameter, η , of both matrices is calculated by dividing the initial compression yield stress by the tensile one, when measured at the same strain rate of $5.55 \cdot 10^{-4} s^{-1}$. Compression tests have been performed with the INSTRON E3000 on cylinders with a height of 2.5mm and a diameter of 5 mm. The results are plotted in Figure 4.7.

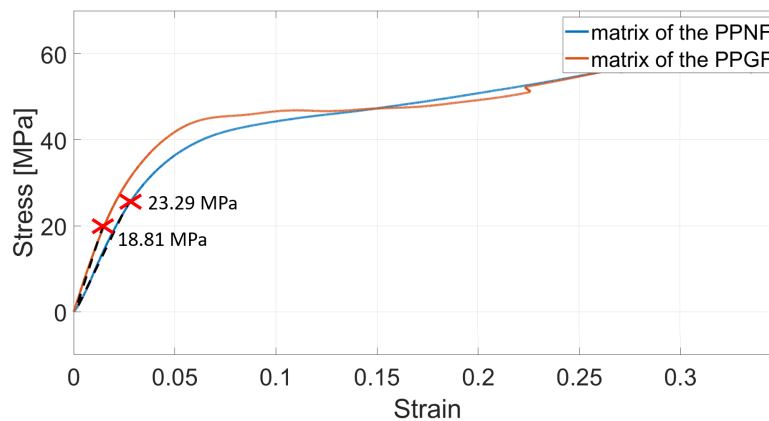


FIGURE 4.7: Results of compression tests for both matrices

Thus, the value of η for the matrix of the PPGF is equal to 2.4 and 3.3 in the case of the matrix of the PPNF.

The last matrix parameters to be identified are damage parameters. In view of this, cyclic loading / unloading tensile tests are performed and tracked by DIC. With the image correlation, it has been seen that the strain and so on damage become quickly localized and non-uniformly distributed. For that reason, the analysis is performed on the 9 first cycles for the PPNF and could not be done for the matrix of the PPGF. Figure 4.8 shows the stress-strain response of PPNF matrix during cyclic tests.

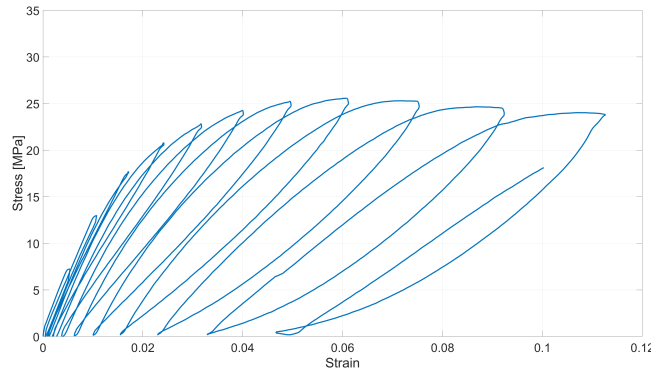


FIGURE 4.8: Stress-strain curve for PPNF matrix during cyclic tests

As stated in Subsection 1.4.1, the isotropic damage variable, D , depends on the cumulated plastic strain, κ , and:

$$\begin{cases} \dot{D} = \dot{\kappa} \frac{Y}{S} & \text{if } \kappa \geq \kappa_D \\ \dot{D} = 0 & \text{otherwise} \end{cases} \quad (4.10)$$

in which S is the material damage modulus, Y the strain energy density release rate and κ_D the material damage threshold.

During the cyclic tests, a volume variation has been observed. This variation is due to (visco)elastic Poisson effect, to non-isochoric plastic flow (modeled by plastic Poisson coefficient, v_P) and to voids induced by matrix damage. In those cyclic tests, the viscoelastic strain can be neglected compared to viscoplastic strain from the early cycles of loading and so on the volume variation by Poisson effect.

The true cross-section divided by the initial one is given by $\frac{s(t)}{s_0} = \exp(\varepsilon_{yy}(t) + \varepsilon_{zz}(t))$ when x is loading axis. Assuming transverse isotropy, $\varepsilon_{yy} \simeq \varepsilon_{zz}$ and $\frac{s(t)}{s_0} = \exp(2\varepsilon_{yy}(t))$. Note that the transverse strain, $\varepsilon_{yy}(t)$, is measured by DIC. Then, the effective cross-section, resulting from compressible plastic flow without damage can be expressed by:

$$\frac{\tilde{s}(t)}{s_0} = \exp(-2v_P \varepsilon_{xx}(t)) \quad (4.11)$$

recalling that $\varepsilon_{yy} = -v_P \varepsilon_{xx}$ by definition of v_P .

Finally, the isotropic damage variable can be expressed by:

$$D(t) = 1 - \frac{s(t)}{\tilde{s}(t)} = 1 - \frac{\exp(2\varepsilon_{yy}(t))}{\exp(-2v_P \varepsilon_{xx}(t))} \quad (4.12)$$

in which v_P is identified by plotting the ratio $\frac{\varepsilon_{yy}(t)}{\varepsilon_{xx}(t)}$ for the first 3 cycles and equals to 0.47.

Considering that viscous elastic strain vanishes during unloading, in-plane strains measured at the end of unloading phases are considered to be fully viscoplastic. Then, the cumulated plastic strain can be computed at the end of each unloading phase of cycle c , with:

$$\kappa_c = \sqrt{2/3} \sqrt{(\varepsilon_{xxUc})^2 + (\varepsilon_{yyUc})^2 + 2(\varepsilon_{xyUc})^2} \quad (4.13)$$

A second degree polynomial function is then used to approximate the D_c vs κ_c curve (Figure 4.9). The value of the polynomial function is given in Equation 4.14.

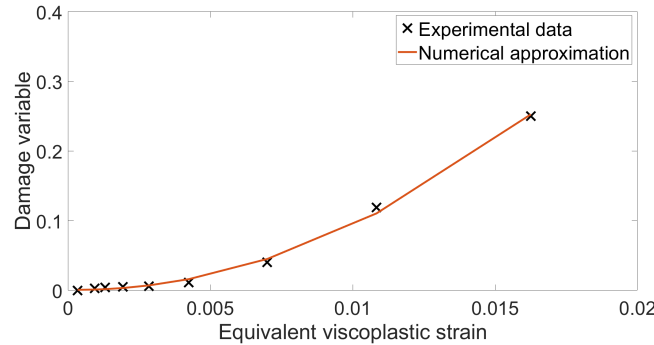


FIGURE 4.9: Evolution of damage in function of cumulated viscoplastic strain

$$D^{ft}(\kappa) = 992.01 * \kappa^2 - 0.63 * \kappa + 0.00086 \quad (4.14)$$

Finally, the identification of the parameter S from Equation 4.10 is made with a linear regression of the $\partial D / \partial \kappa$ vs Y curve. The values of Y at the end of unloading are calculated assuming a unidimensional stress state, and:

$$Y_c = \frac{(\sigma_{xx,c})^2}{2E_{\text{unload},c}(1 - D_c)^2} \quad (4.15)$$

in which E_{unload} is the Young modulus measured at the end of unloading phase of the c^{th} cycle. It should be noted that the expression of Y is true as long as there is no striction (i.e. no strain localization) in the specimen. The value of $\partial D/\partial \kappa$ is approximated by :

$$\partial D/\partial \kappa \approx [D^{ft}(\kappa_c + \delta\kappa) - D^{ft}(\kappa_c - \delta\kappa)] / 2\delta\kappa \quad (4.16)$$

with $\delta\kappa = 10^{-4}$. The curve $\partial D/\partial \kappa$ vs Y shows linear evolution with a slope equal to $1/S$. A linear regression leads to an identified value of S of 0.32 MPa for the matrix of the PPNF. The 4th cycle allows to calculate the matrix damage threshold and its value is equal to 0.0019.

After all matrix parameters have been identified, Figure 4.10 compares numerical and experimental results for both materials at high tensile speed (100 mm/s) and at low tensile speed (10 mm/min).

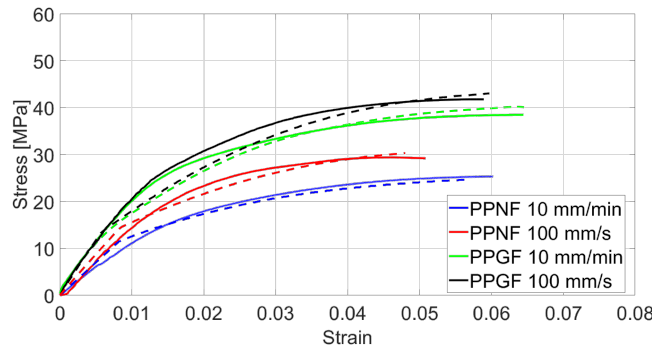


FIGURE 4.10: Correlation between numerical and experimental results for both matrix; straight lines represent experimental values and dashed lines represent numerical values

With Figure 4.10, one can see that the model gives quite accurate results and especially for the matrix of the PPNF. On the other hand, a gap is seen at the end of the viscoelastic behavior. This indicates that the initial yield stress is probably overestimated.

4.1.3 Fibers and matrix / fiber interface parameters

The data of fibers' orientation, length and cross-section extracted from microtomographic scans are input in the VUMAT in order to simulate the mechanical behavior of reinforced materials, PPNF and PPGF. As explained in previous section, the geometrical properties and orientation of natural fibers have been precisely measured. A mean value for the length has been identified at 0.42 mm with a standard deviation equal to 0.32 mm and for the diameter $3.74 \cdot 10^{-2}$ mm with a standard deviation equal to $9.5 \cdot 10^{-3}$ mm for the PPNF. Geometrical properties of glass fibers have been manually measured with the software ImageJ given a fibers' length equal to 0.3 mm

and a fibers' diameter equal to $6.4 \cdot 10^{-3}$ mm. In order to define fiber media in the VUMAT, fibers orientation distributions with respect to the IFD is discretized into 10 intervals, from 0 to 90° . The number of occurrences of fibers orientations in each interval is then calculated. This allows to define 10 families of fibers, with an orientation with respect to the IFD from 5° to 85° by step of 10° , and of volume fraction depending on number of occurrences reported to the total fiber volume fraction. Volume fraction for all fibers families thus defined for PPNF are plotted in Figure 4.11 for the cutting angle of 0° , 30° and 45° .

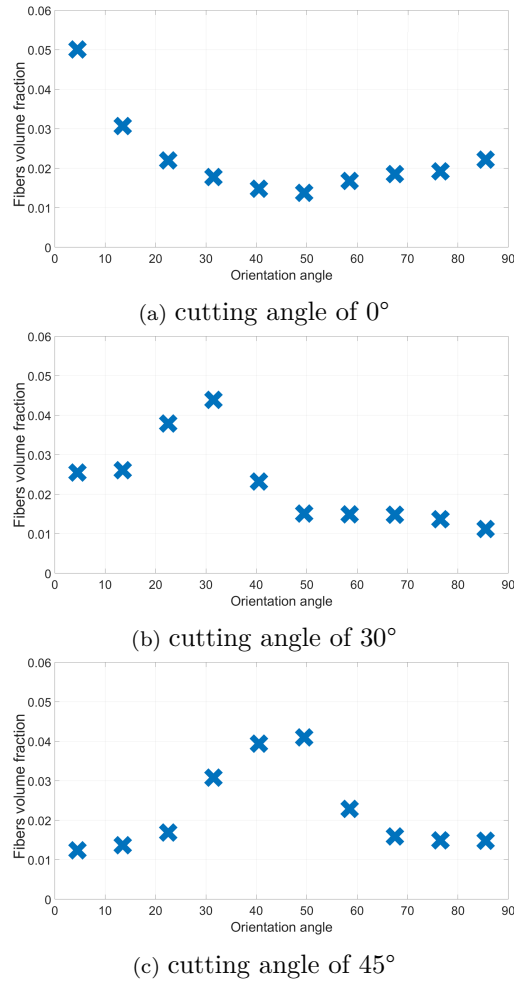


FIGURE 4.11: PPNF fibers' discretized orientation distributions

As a reminder, in the model used in this PhD thesis work, the transmission of the stress from the matrix to the fiber is done by a shear transfer process. Thus, the next parameter to be characterised is the Interfacial Shear Strength (IFSS, τ , Equation 1.17). This parameter is directly linked to several factors, such as nature of matrix and fibers, possible treatment of compatibilization, fiber volume fraction, process parameters, etc. Here, the IFSS value has been determined by fitting numerical results with experimental results for both materials. This value has been determined by using tensile specimens with a cutting angle of 0° and with fibers orientation distribution most centered on 0° to maximize the load transmission from matrix

to fibers. Thus, the implication of IFSS in mechanical response is maximized, and a robust identification can be expected.

In view of this, a tensile test has been selected among tensile tests performed at different strain rates and different cutting angles with both PP-35GF and PP-30NF. The strain rates are the same as for tests on matrix (see Table 4.3) and the cutting angles are 0° , 30° and 45° . For these tensile tests, optical extensometer is used to measure the axial elongation of the ROI. Since the material is naturally black, the ROI of each specimen is painted into a white surface in order to create black-and-white transition lines. Two different optical extensometers are used, the first one is a RUDOLPH ZS16D-50, used with the quasi-static tensile specimens with a precision of $3\mu\text{m}$. The second is a RUDOLPH 200XR, used with the dynamic tensile specimens with a precision of $5\mu\text{m}$. Figures 4.12 and 4.13 show the results obtained for both materials in which the axial strain is calculated as the ratio between the axial elongation measured with the extensometer by ROI's initial length (30 mm for quasi-static tensile specimen and 20 mm for dynamic tensile specimen).

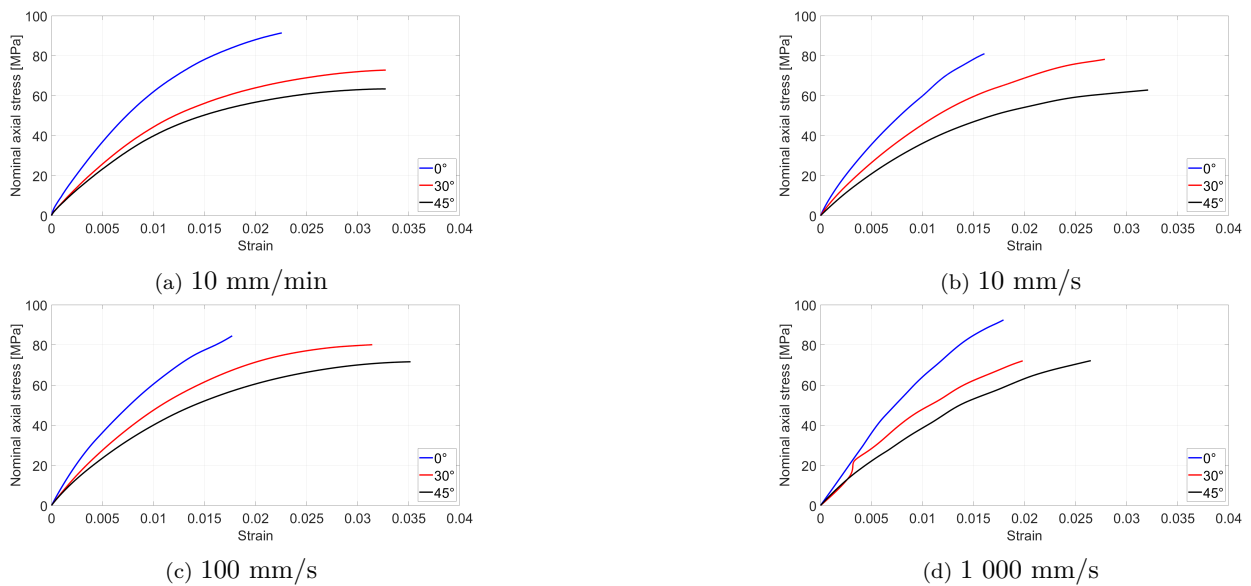


FIGURE 4.12: Nominal axial stress and strain results of PPGF tensile tests

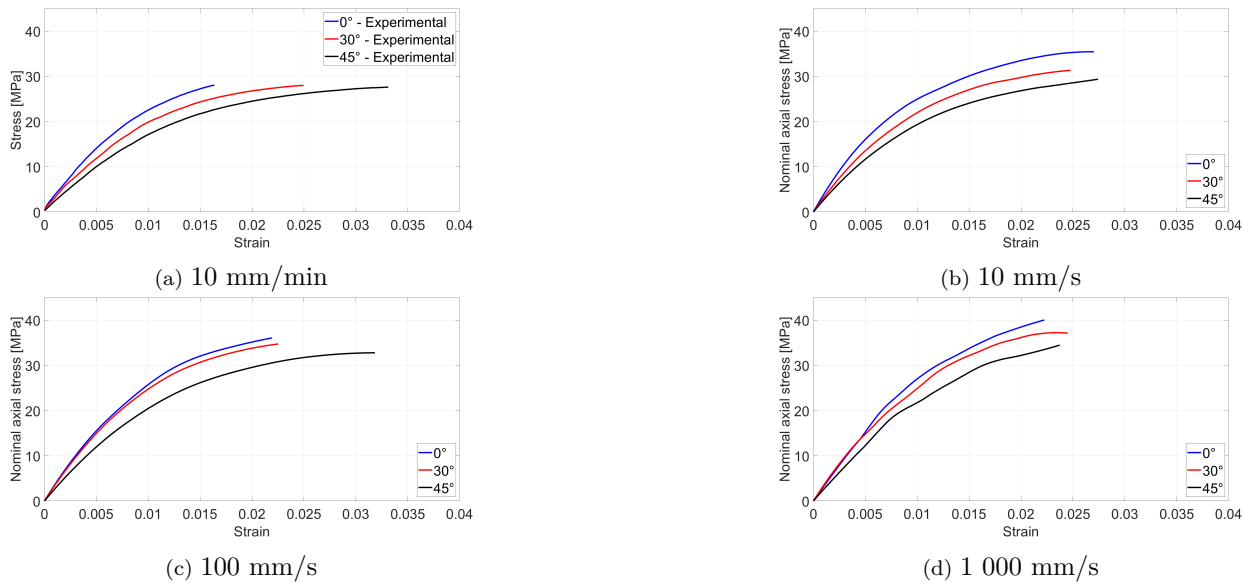


FIGURE 4.13: Nominal axial stress and strain results of PPNF tensile tests

As expected, when compared to the results of both matrices (see Figure 4.5), one can see that the reinforced materials become more brittle but also gain in tensile strength and rigidity, especially for a cutting angle of 0° vs IFD (meaning that fibers are mostly oriented along loading direction). When increasing the cutting angle, strength and brittleness of the composites logically decrease.

Once the experimental campaign is done, the value of the IFSS can be determined. As already highlighted, because the impact of IFSS will be maximized when the proportion of fibers oriented into loading direction is maximal, the specimen that showed the higher proportion of fibers oriented at 0° is selected for the identification of the IFSS. Then, in order to reduce computational time, tensile tests are performed at the speed of 100 mm/s. The value of IFSS identified for PPGF is equal to 21 MPa and to 9 MPa for PPNF. The difference between these values can be explained by the nature of both fibers. Indeed, natural fibers usually present hydrophilic properties when polypropylene matrices present hydrophobic properties, thus leading to weak fibers/matrix adhesion, even if grafting of MA, for instance, can lead to some improvements [147]. Thus, the adhesion between fibers and matrix is less effective in the case of natural fibers. The identified value for the PPNF is compared with values found in the literature. For example, Aliotta et Al. [148] have studied the IFSS for PP/hemp fibers, the IFSS values identified varies from 7 MPa to 15 MPa, depending on surface treatment. Also, Van Den Oever et Al. [149] have identified values between 8 MPa and 12 MPa for PP/flax fibers and MAPP/flax fibers respectively. Thus, the value identified is logical regarding the literature.

Figure 4.14 compares the tensile behaviour of both composites, where numerical curves are computed with identified value of IFSS. There is a satisfying match up to a few percent of

strain but numerical prediction overestimated the experimental response at the end of loading, which can be directly attributed to fibre/matrix debonding.

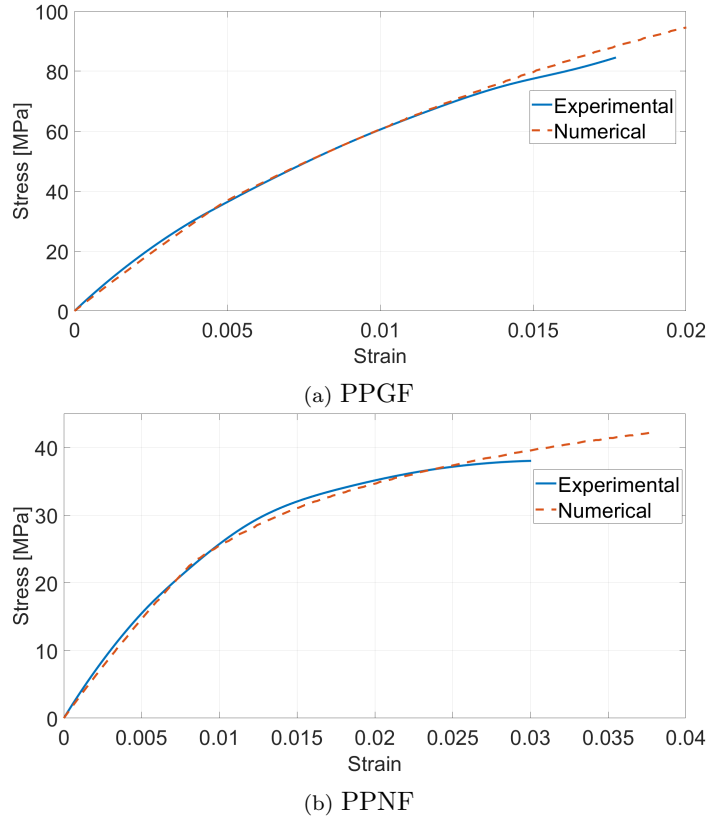


FIGURE 4.14: Comparison between experimental results and numerical results

In the VUMAT, fibre/matrix debonding is modelled considering a progressive degradation of the interface between the matrix and the fibers during loading (Eq. 4.17). a , b and ϵ_{th} are material parameters to be identified.

$$\begin{cases} \delta^\alpha = a \left(\frac{\epsilon_F^{Axial,\alpha} - \epsilon_{th}}{\epsilon_{th}} \right)^b \frac{L^\alpha}{2}, & \text{if } \epsilon_F^{Axial,\alpha} \geq \epsilon_{th} \\ \delta^\alpha = 0, & \text{otherwise} \end{cases} \quad (4.17)$$

The parameter ϵ_{th} is a fiber axial strain threshold for the debonding. Once fibers deformation threshold is reached, the debonding is triggered at fiber tips. Its value correspond to the strain reached at 75% of fibers ultimate load [86]. With Figure 2.8, one can see that the ultimate strain is reached at a fiber axial strain of 0.0145%. Thus, the ϵ_{th} is rounded to 0.01. Voids will then propagate from one tip of the fiber to the other reducing the length of the fiber available for the transmission of the loading [150]. It is worth to remind that the evolution law of debonded fiber length 4.17 has no physical fundation. The parameters are determined by fixing the value of ϵ_{th} and by varying a and b until numerical results fit experimental results. Results of the identified values are summarized in Table 4.5.

	PPGF	PPNF
ϵ_{th}	0.005	0.01
a	0.01	0.05
b	1.9	2

TABLE 4.5: Debonding parameters for both materials

A sensitivity analysis has been performed to study the impact of parameters a and b on the value of the debonded length δ^α . Thus, the impact of both parameters on the value of δ is studied by varying the value of a and then the value of b (Figure 4.15).

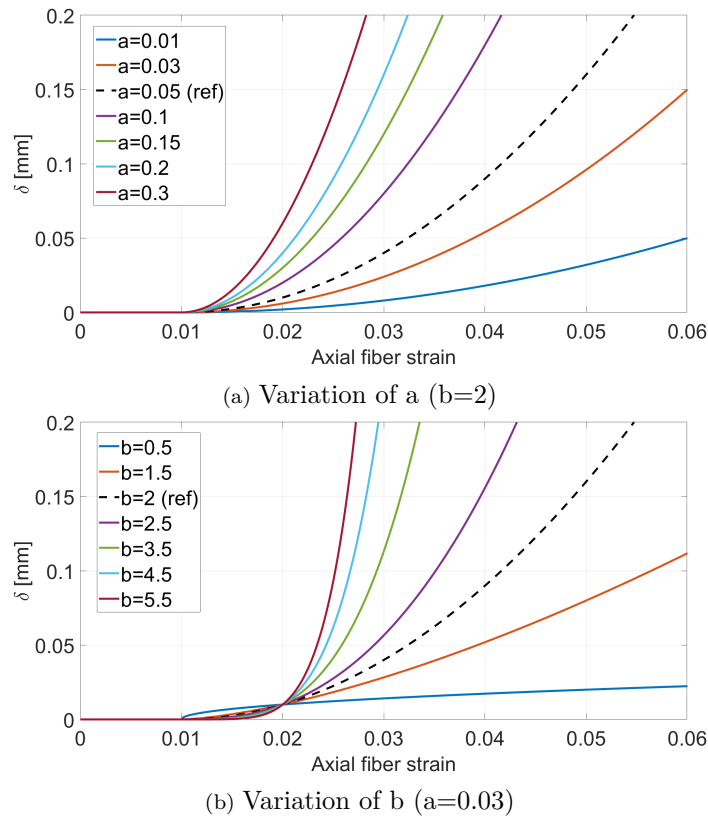
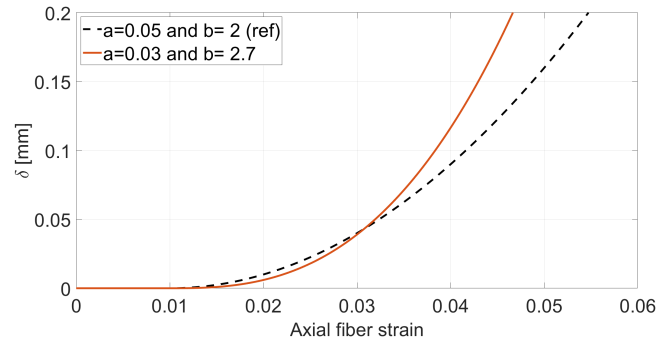
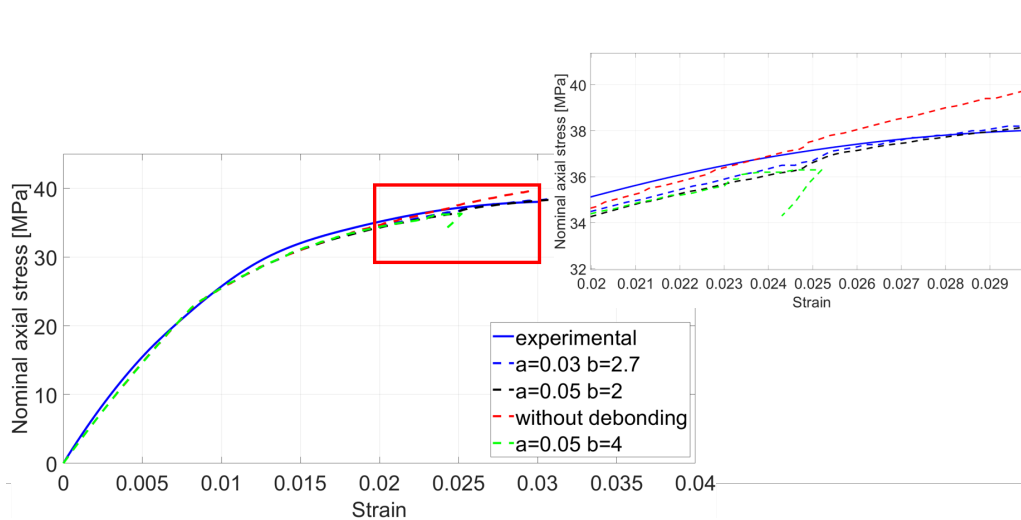
FIGURE 4.15: Impact of the variation of a and b on δ

Figure 4.15 shows that the variation of a causes the maximum value for δ , i.e. $L/2 = 0.2$ mm here, to be reached more or less abruptly. The variation of parameter b has the same impact for the value of δ and in addition, may also completely changes the shape of the evolution of δ . Indeed, when b is higher than 2, δ increases very abruptly after fiber strain reaches debonding threshold while its increase is far smoother when b is lower than 2. It is worth noting that several couples of parameters a and b may lead to a fit of numerical values to experimental data. For example, in this study, another couple of parameters a and b is found and equal to 0.03 and 2.7 respectively. The evolution of δ is plotted in Figure 4.16 for the case of $a = 0.05$, $b = 2$ and $a = 0.03$, $b = 2.7$.

FIGURE 4.16: Evolution of δ according to two couple of a and b

One can see that δ reaches more quickly the value of 0.2mm (i.e. max value for debonding) for the second couple (orange curve) than the first identified couple.

Finally, the comparison of the mechanical behavior of the PPNF with a cutting angle of 0° regarding loading direction and tested at 100 mm/s with both identifications of debonding parameters are plotted in Figure 4.17. Also, the behavior without matrix / fiber debonding and with a high value of the exponent b are plotted.

FIGURE 4.17: Comparison of the mechanical behavior of the PPNF at 100 mm/s between different values of a and b

One can see that both identifications (blue and black dashed-lines) are quite similar and lead to a relatively good fit with the experimental values. Then, with a high value of b , the critical value of δ is reached more quickly and leads to simulation error. Finally, when the debonding is disabled, the stress / strain curve continues to grow, leading to an important gap between numerical results and experimental behavior. That confirms the necessity to take debonding into account for an accurate prediction of SFRT behavior.

4.1.4 Model validation

Once all material parameters are identified, numerically predicted tensile behavior can be compared to experiments.

Tensile tests are numerically simulated using Abaqus Explicit and the VUMAT, with a mesh element size of 2 mm. It is worth reminding that, for the PPNF, real fibers orientation distributions are implemented in the model and the mean fibers length and diameter measured are considered. For the PPGF, geometrical properties have been manually measured on several fibers using the software ImageJ and the mean value has been used for numerical simulations. Results are plotted in Figure 4.18 for the PPNF and in Figure 4.19 for the PPGF.

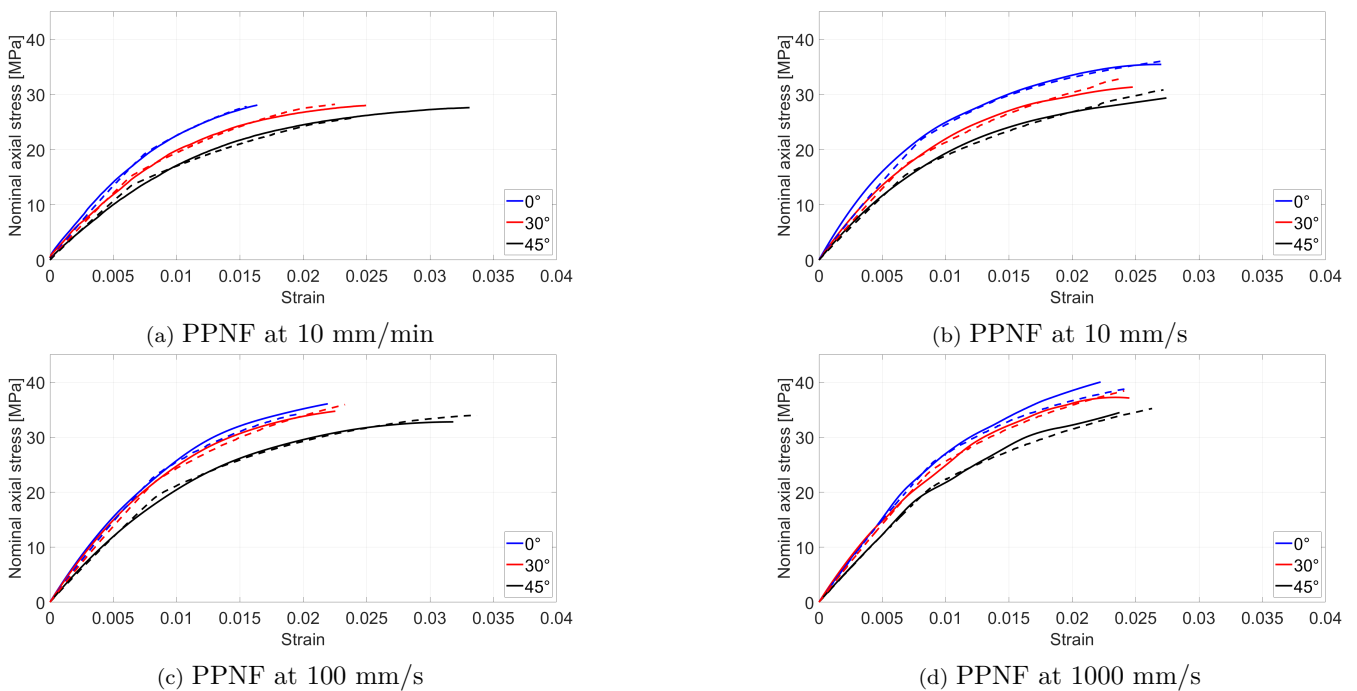


FIGURE 4.18: Correlation between experimental and numerical results for PPNF; straight lines are experimental values and dashed-lines are numerical values

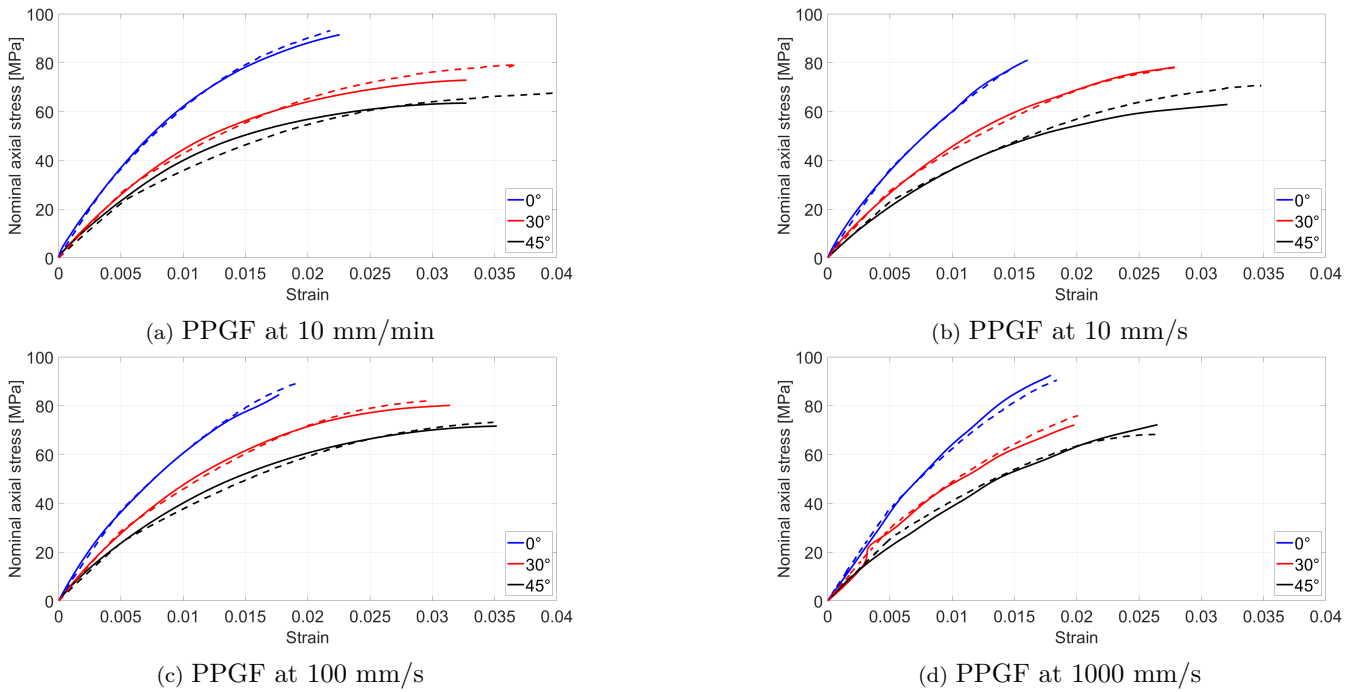


FIGURE 4.19: Correlation between experimental and numerical results for PPGF; straight lines are experimental values and dashed-lines are numerical values

With Figures 4.18 and 4.19 one can see that the model fairly simulates the real behavior of both materials and especially for the PPNF. This is explained by the use of the real fibers orientation distributions. The modeling of the SFRT is then validated and the mechanical information from the numerical calculations can then be used to determine a relevant failure criterion.

4.2 Investigation of SFRT's failure behavior

In this section, SFRT's failure behavior is investigated. Numerous studies in the literature are dedicated to failure phenomena of composites such as laminates composites, 3D printed composites, woven thermoplastics etc [151–155]. For most of these composites, the orientation of the reinforcement is known and mostly mastered. Also, in the case of laminated composites, microstructure can be considered as homogeneous and orthotropic which "simplifies" their study. It has been seen in the literature that for laminates composites, the most common failure criteria used in industrial context are based on a maximum strain or a maximum stress [13] (Figure 4.20). For Camanho [13], the theory of maximum strain or stress regroups the criteria based on the maximum matrix strain or stress, maximum fiber strain or stress and / or maximum shear strain or stress.

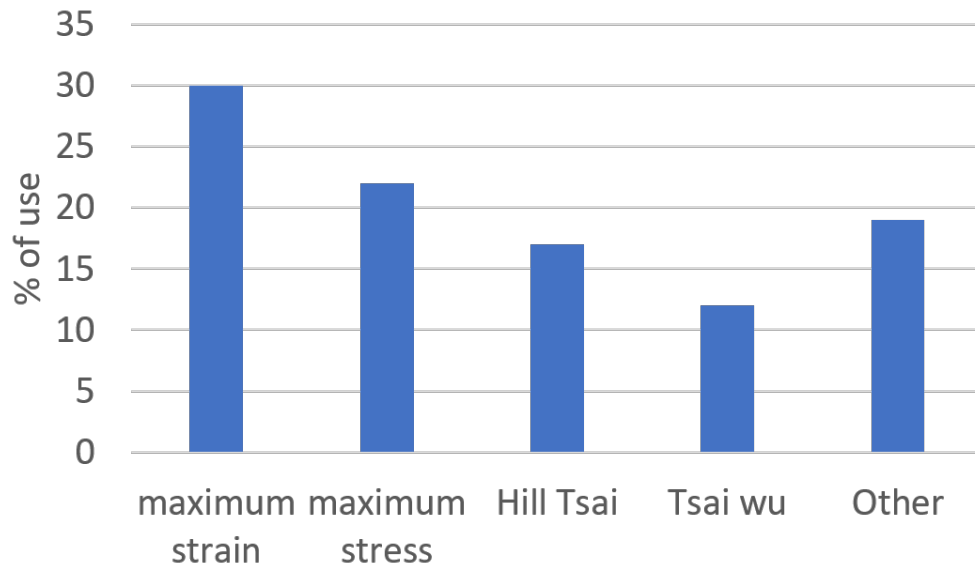


FIGURE 4.20: Percentage of use of various failure criteria in industrial context [13]

Such criteria are not adapted for injection molding SFRT, because of the unmastered fibers orientation. As it has been seen, fibers orientation depends on the studied localization, even for a simple geometry such as an injected plate. Moreover, SFRT's behavior highly depends on fibers orientation regarding the loading direction. Therefore, for the stress at break, when fibers are oriented parallel to the loading direction, SFRTs present a higher stress level than when fibers are oriented perpendicular to the loading direction. Also, the strain at break varies according to fibers orientation, with higher values when fibers are oriented perpendicular to the loading direction. Gruber et al. [156] have implemented a maximum strain criterion on LS-Dyna and for the reason explained previously, the results were not convincing. According to them, anisotropic strain failure criterion may enhance the precision of the simulations as the value of the maximum strain depends on the direction of the solicitation. Zhou and Mallick [157] have studied the implementation of a uniaxial tension failure criterion for a PA-GF and based on composite nonlinear damage identified from uniaxial tensile tests. This criterion has the disadvantage of not taking into account the microstructure specificities of the composite in the development of the model. Also, it has been seen that fibers are not perfectly oriented in one direction and that significant orientation variations are measured on the same part. Thus, such criteria are not appropriate for injection molded SFRT, even while considering different maximum strain or stress values for global fibers orientation regarding cutting angle / stress. It is therefore necessary to define a criterion that takes real fiber orientation into account.

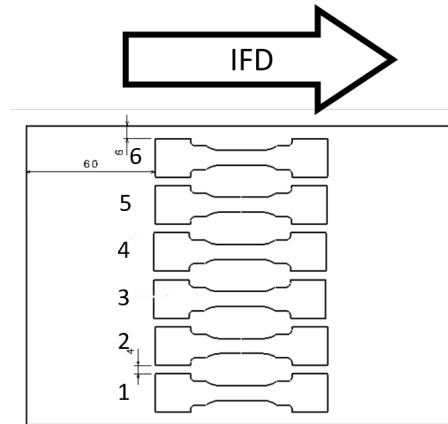
Horst and Spoormaker [158] found that for SFRT, the damage is initiated at fiber tips and then propagates along fibers, thus they introduce the damage by matrix / fibers debonding. This phenomenon is responsible for void growth and coalescence between fibers and matrix that at term may lead to failure. This observation has helped researchers for the determination

of damage mechanisms that lead to failure. Dutra et al [159] have developed a failure criterion that takes into account damage at the matrix/fiber interface based on interfacial shear strength in tension. Their study is done with 3D-printed continuous carbon fibers reinforced thermoplastics. In their study, three states may trigger the failure, depending on the constituent studied: matrix, fiber or matrix/ fiber interface. A criterion based on the maximum fiber axial stress is implemented to initiate rupture from fibers. For the matrix, a failure criterion similar to the Drucker-Prager yield criterion is implemented. Finally, for matrix / fiber interface a quadratic failure criterion is implemented. Nguyen and Kunc [160] proposed a failure criterion that considers both matrix macrocracks and matrix / fibers debonding in the case of long fibers. In their model, the failure of the material is supposed to happen when composites damage variable reaches a threshold value. It should be noted that the model used at the LAMIH allows to consider matrix damage behavior and also matrix / fiber debonding. Thus, the failure criterion developed in this PhD thesis work may lie on simulated evolution of those both damage phenomena.

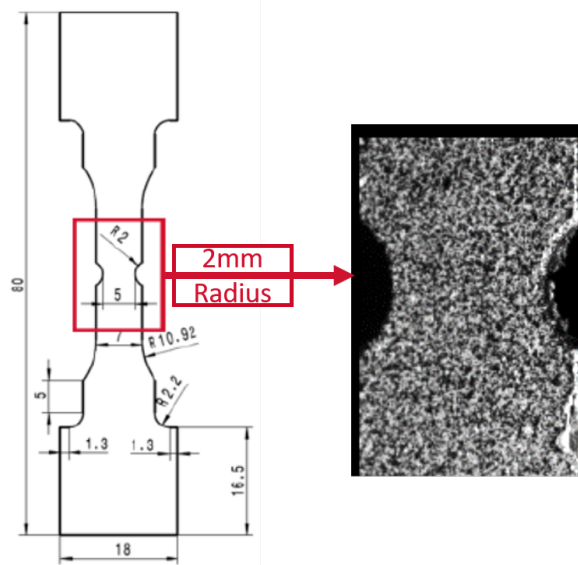
In the following sections, the failure of SFRTs is first experimentally studied and then numerical analyses are performed to investigate the implementation of a failure criterion.

4.2.1 Failure of notched tensile specimens

As a reminder, in the previous section, tensile tests have been performed on tensile specimens with straight geometries. As a drawback, failure may occur anywhere, even outside of the ROI. To solve this problem, notched tensile specimens have been designed (see Figure 4.21) and cut parallel to the IFD. The aim is to force the localization of the strain in the central part of the specimen so that the failure occurs there. Tensile tests of PPNF and PPGF have been performed at 100 mm.s^{-1} (4 specimens per material). Local axial strain is measured on the surface of tensile specimens using DIC at an acquisition rate of $50\,000 \text{ im.s}^{-1}$ with the high-speed camera.



(a) PPGF tensile specimen



(b) PPGF tensile specimen

FIGURE 4.21: Cutting plan of notched tensile specimens

The images are treated with the software VIC 2D. In order to find a good size of facets for the post-treatment of the results, images without displacement are analyzed several times with different facet sizes. Since no displacement is imposed, the in-plane strain components are theoretically equal to 0 and computed "strain" values using the DIC can be considered as noise. Thus the facet size that allows to have measured "strains" as close as possible to 0 is selected, see Figure 4.22 for axial "strain" component.

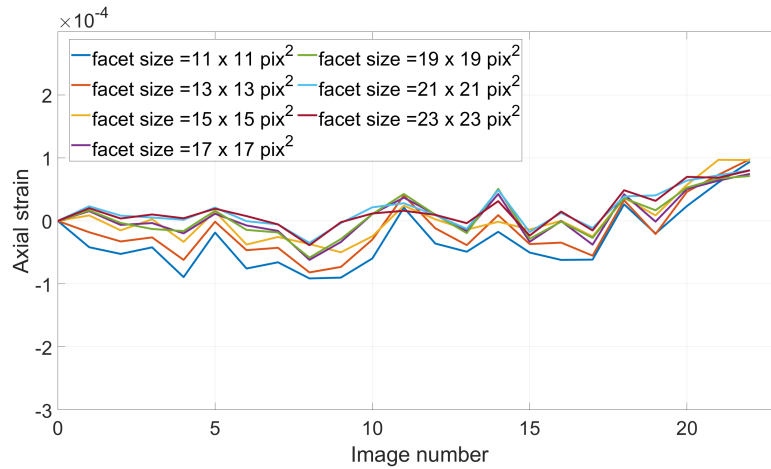
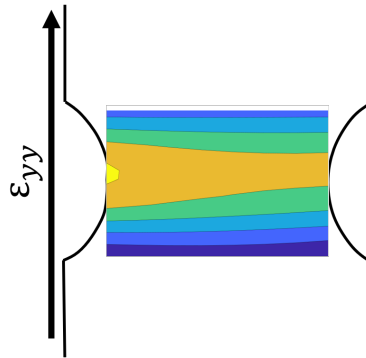
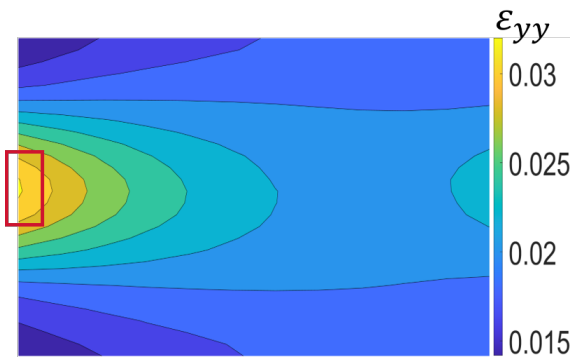


FIGURE 4.22: Noise measurement with the DIC

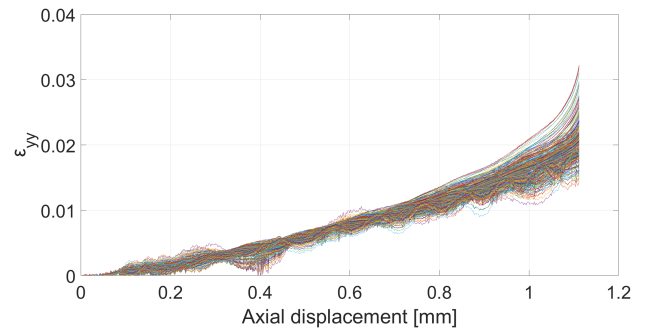
It can be seen that the noise measurement for facet size from $15 \times 15 \text{ pix}^2$ to $23 \times 23 \text{ pix}^2$ are quite similar. Then, keeping in mind that a smaller facet size will allow a better capture of localized strain gradient, size of $15 \times 15 \text{ pix}^2$ ($0.3 \text{ mm} \times 0.3 \text{ mm}$) is selected for all specimens.

The localization of the mapping of ε_{yy} in notched tensile specimen is represented in Figure 4.23. The local axial strain at the pre-failure step (i.e. for the last recorded image before failure) of several tensile specimens for both materials are mapped in Figure 4.24 and the evolution of ε_{yy} in all facets is also plotted in Figure 4.24. Experimentally, crack initiation always appears in surface at the localization where the local strain is maximum (yellow zones).

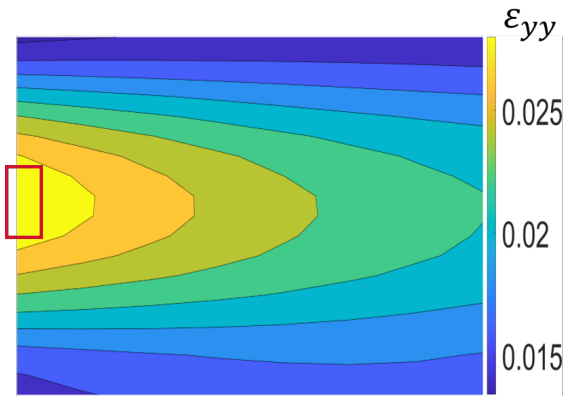
FIGURE 4.23: Localization of the mapping of ε_{yy} on a notched specimen



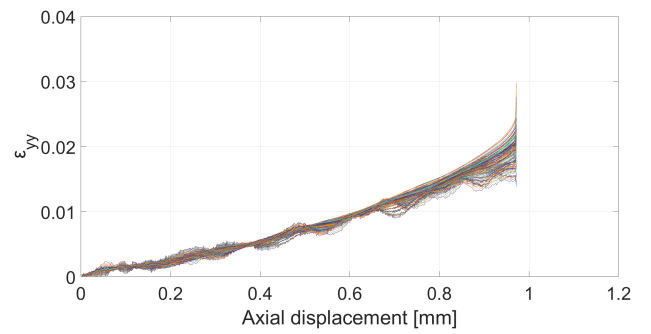
(a) PPGF tensile specimen N°1



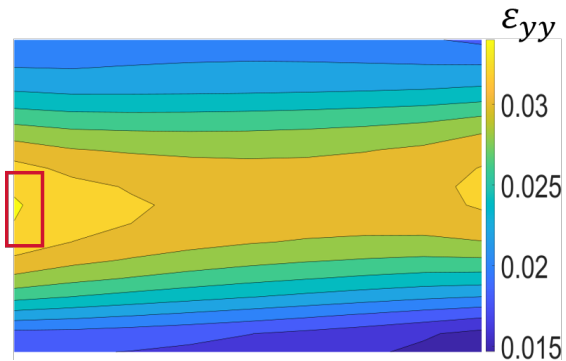
(b) PPGF tensile specimen N°1



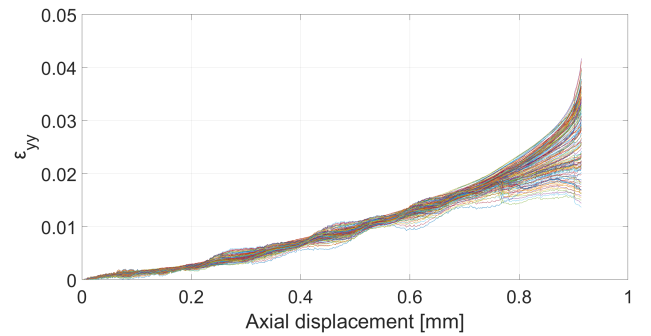
(c) PPGF tensile specimen N°4



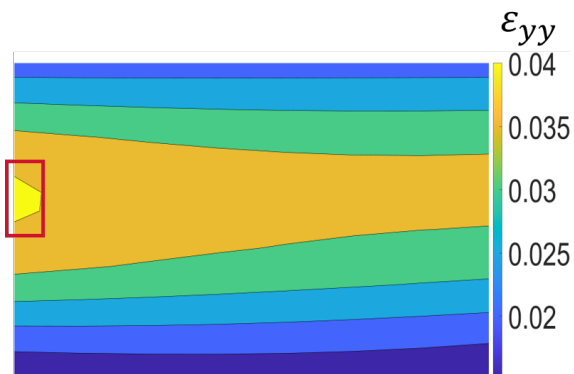
(d) PPGF tensile specimen N°4



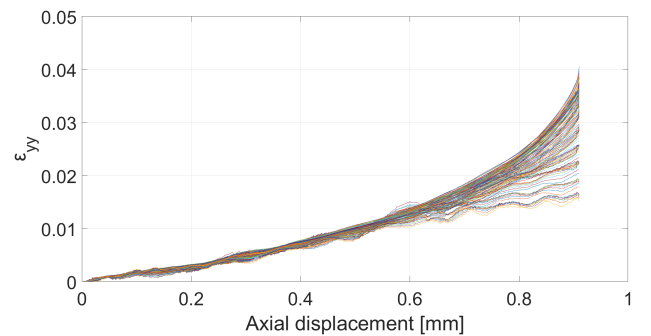
(e) PPNF tensile specimen N°2



(f) PPNF tensile specimen N°2



(g) PPNF tensile specimen N°4



(h) PPNF tensile specimen N°4

FIGURE 4.24: Mapping of ε_{yy} at the pre-crack step and evolution of ε_{yy} during tensile tests; numbers refers to the tensile specimen position in Figure 4.21

So, as expected, the crack initiation (in surface) appears in the middle of the ROI, in the notched zone. The value of axial strain at crack initiation is computed as the average of axial strain computed in an area of 10 facets surrounding the crack initiation localisation (corresponding to an area of 0.36 mm^2). The average axial strains at break calculated for both materials are summarized in Table 4.6 and the discrepancy of those of PPNF is shown in Figure 4.25 for three cutting angles, 0° , 30° and 45° regarding IFD. The blue rectangles represent first and third quartile, the red line is the median and the min and max values are represented by the black dashed lines.

	Mean strain at break	
	PPGF	PPNF
Specimen 1	0.031	-
Specimen 2	0.021	0.032
Specimen 3	0.032	0.039
Specimen 4	0.029	0.034
Specimen 5	0.027	0.039
Standard deviation (STD)	0.004	0.0034

TABLE 4.6: Mean value of axial strain, ε_{yy} , at failure initiation in surface for both materials and with a 0° cutting angle

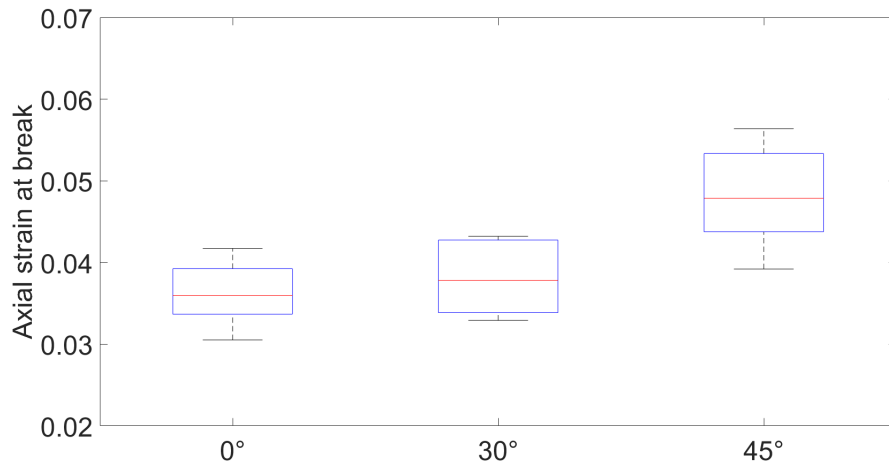


FIGURE 4.25: Boxplot of PPNF axial strain at break for notched specimens

With this tensile specimen geometry, one can see that the standard deviation of average axial strain at break is quite similar for both materials tested at 0° , with value of 0.004 for the PPGF and 0.0034 for the PPNF. The values of average axial strain at break vary from 0.021 to 0.032 for the PPGF and from 0.032 to 0.039 for the PPNF. Also, it can be noted that the standard deviation of the average axial strain at break of PPNF is quite similar for the three cutting angles. The variability of this quantity can be mostly explained by the fact that specimens have been cut from different parts of the plate and therefore have different local fiber orientations.

In this section, the failure of SFRTs has been studied. It has been seen that the axial strain at break is variable with notched tensile specimens. In addition, the rupture depends on fibers orientation and thus, the establishment of an anisotropic failure criterion seems important. To confirm the influence of fibers orientation on the rupture and to allow to have another loading case, the failure behavior of SFRT is studied during high-speed bulge tests in the next subsection.

4.2.2 SFRT's failure behavior during bulge tests

In this subsection, bulge tests have been performed to study the crash behavior of both materials. Figure 4.26 shows a picture of the experimental set-up. Bulge test consists of the high-speed projection of a punch (with a 40 mm diameter) toward an injection molded plate, in which a hole has been made by waterjet cuts (Figure 4.27). The speed of the punch is here equal to 100 mm/s. The impact between the punch and the perforated plates have been filmed with a high-speed camera with a frame rate of 600 images per second.

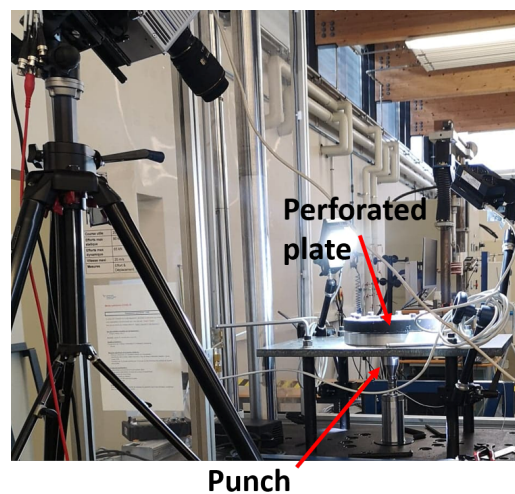


FIGURE 4.26: Experimental set-up for the bulge tests

In this study, the localisation and order of appearance of cracks in surface of the plate is investigated. It is reminded that fibers are mainly oriented parallel to the IFD in the injected plates. Different fibers orientation, from 0° to 90° , are therefore encountered around the hole. That will allow to evaluate the failure criterion with more complex loading paths compared to uniaxial tensile tests. During this analysis, focus is made on 4 different sides (Figure 4.27). Fibers located at the west and east sides of the hole are oriented parallel to the loading direction. On the contrary, fibers at north and south sides are oriented perpendicular to the loading direction.

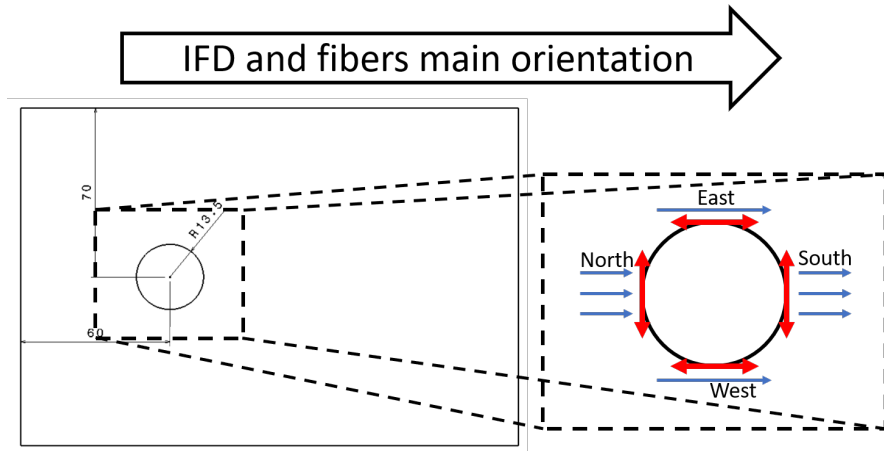
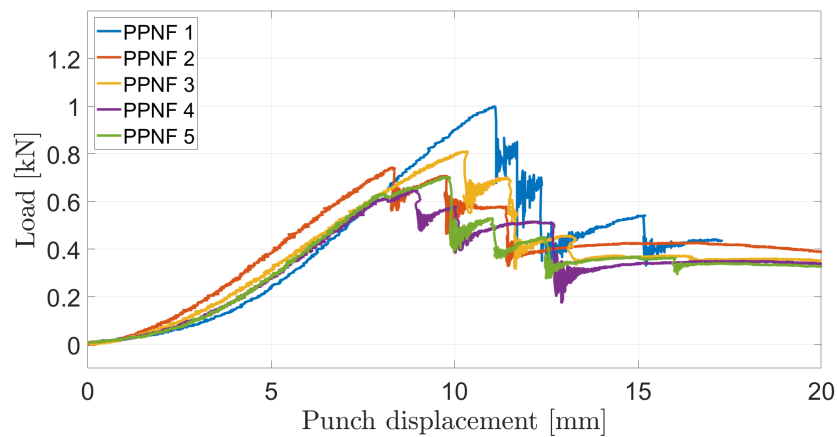
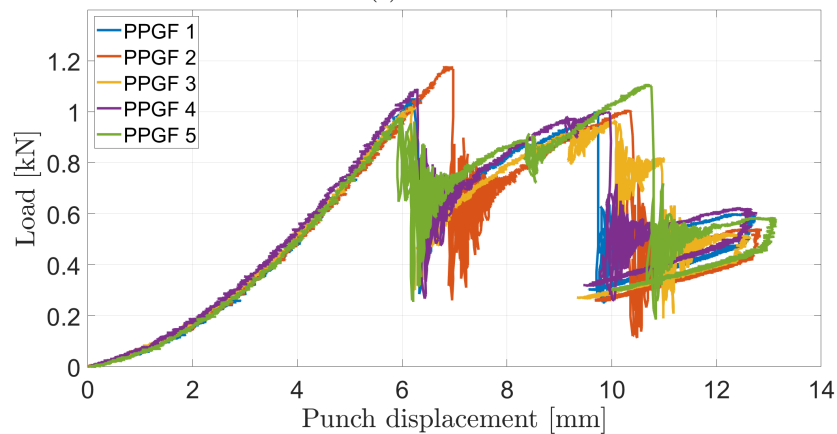


FIGURE 4.27: Plan of the perforated plates and schematic representation of fibers orientation (blue arrows) with respect to load direction (red arrows)

For each plate of both materials, the load is plotted in function of the displacement of the punch. The load is directly measured by the load cell implemented on the tensile machine. As long as the punch is not in contact with the plate, the measured load oscillates around zero. Thus, the displacement of the punch is measured from the moment when the force increases.



(a) PPNF



(b) PPGF

FIGURE 4.28: Load vs punch displacement during bulge tests for both materials

As for previous chapters, PPGF provides results with low discrepancy, except for one case (plate n°2). Indeed, the first crack for plates 1, 3, 4 and 5 appears after a displacement of the punch of 6 mm. On the contrary, tests on PPNF leads to more variable results. The first crack appears between 8 and 11 mm of displacement of the punch.

Figure 4.29 shows the order of appearance of cracks for one plate of both materials and Table 4.7 gives the order of appearance of cracks for all plates of both materials.

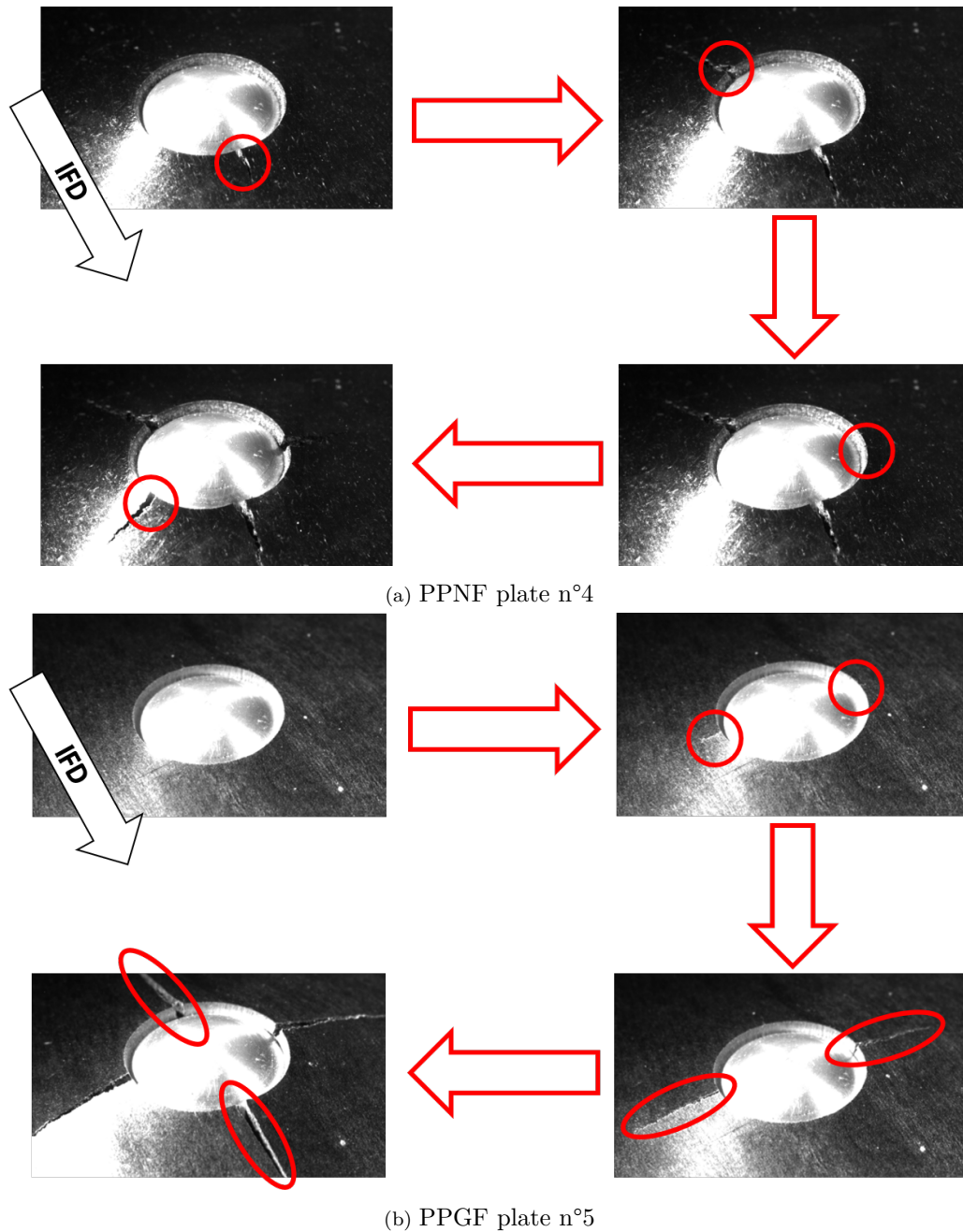


FIGURE 4.29: Example of order of appearance of cracks of one plate for both materials

Material and plate number	Order of appearance of cracks			
	1	2	3	4
PPGF 1	E/W	N/S	-	-
PPGF 2	E/W	N/S	-	-
PPGF 3	E/W	S	N	-
PPGF 4	E/W	N/S	-	-
PPGF 5	E/W	N/S	-	-
PPNF 1	S	W	N	E
PPNF 2	W	E	S	N
PPNF 3	N	E/W	S	X
PPNF 4	S	N	E	W
PPNF 5	W	E	N	S

TABLE 4.7: Crack order for both materials obtained during bulge tests; N = north, S = south, E = east, W = west and X is for none

For the PPGF, the same crack history is observed for all plates. The first initiation is double with cracks appearing simultaneously (or almost) at west and east sides of the hole and then the second initiation is also double with cracks appearance at north and south sides of the hole. This crack appearance order shows that the weakness zone is located where fibers are tangential to the hole and parallel to the loading direction (Figure 4.27). It is worth noting that matrix damage is slowed down by fibers when their orientation is mostly parallel to the loading direction. In addition, fibers debonding is initiated at fiber tips when the threshold of fibers axial strain is reached. Since fiber axial strain is maximized when fibers are oriented parallel to loading direction, the threshold is attained early. Therefore, the breakage located at west and east side is likely to be caused by matrix / fiber debonding regarding its predominance over matrix damage.

On the contrary, for the PPNF, the crack order of appearance seems random. For instance, the first crack is not always located in west or east side of the hole. This difference is likely to be induced by the nature of fibers. As seen in previous sections, natural fibers present variable geometrical properties and also a complex structure. For example, for plate PPNF n°4, a large fiber located on the surface of the plate and close to the hole seems to be at the origin of the crack initiated in the southern zone (Figure 4.30).

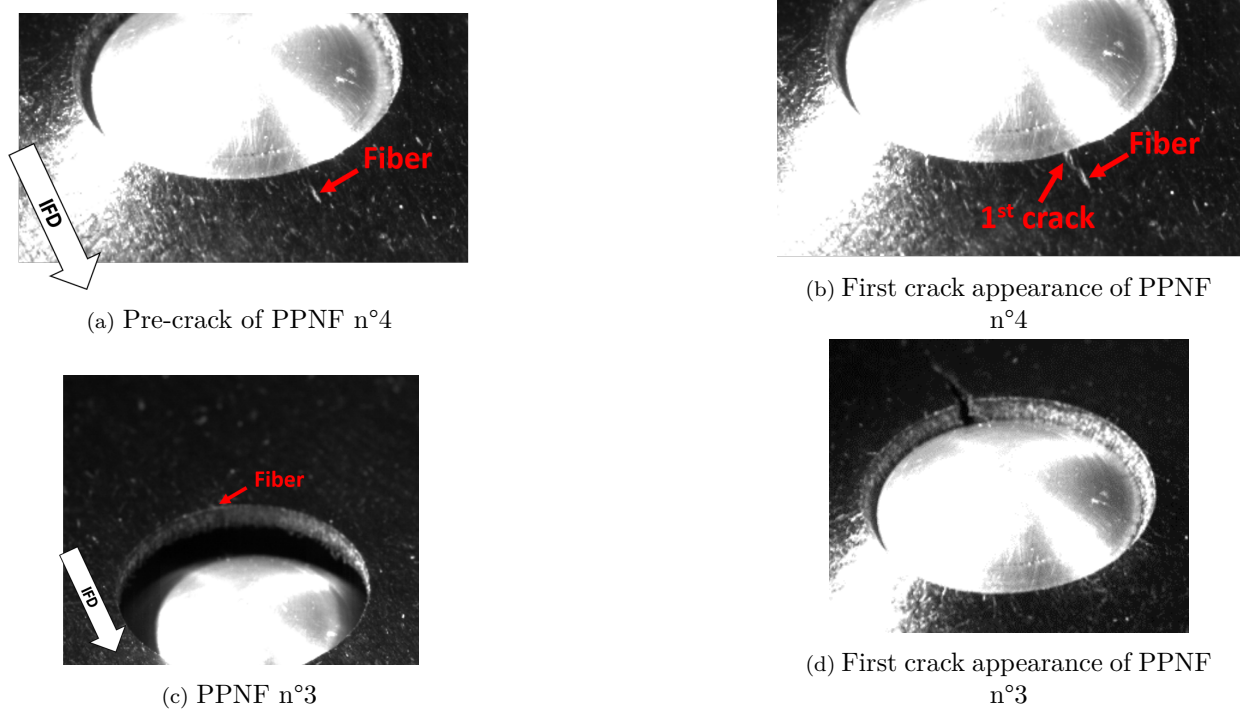


FIGURE 4.30: Example of PPNF crack

In this section, the failure behavior of SFRT during bulge tests has been studied. It has been seen that the PPGF presents the same history of crack initiation for the 5 plates, with a double initiation for the first crack at east and west sides of the hole. It means that in the presence of controlled geometry fibers, the weak zones can be predicted to be located at east and west sides. On the contrary, for the PPNF, the history of crack is not predictable. It can be affected by higher defect ratio in fibers, presence of larger fibers, etc, that act as crack initiators. Yet, in most cases, the first crack occurs on the west and/or east sides of the hole, where fibers are mainly oriented parallel to the loading direction and thus where matrix / fiber debonding is maximized while matrix damage is minimized. In the next section, both experiments are numerically tested. First, tensile tests on notched specimens are simulated in order to find a failure criterion and then bulge tests are simulated in order to assess its relevancy.

4.3 Towards a failure criterion

The aim of this subsection is to investigate the implementation of a failure criterion based on matrix / fibers debonding and matrix damage using the VUMAT. Thanks to the use of the VUMAT, matrix behavior specificities (VE, VP...) and fibers properties (orientations, geometrical properties...) are considered.

In view of this, first, notched tensile specimens are numerically simulated to define a failure criterion based on experimental results. Then, the criterion is applied to numerical bulge tests to assess its relevancy.

In order to consider microstructural damaging, in this study, the failure criterion is based on the evolution of a debonded fibers' length ratio and of matrix damage. As explained in Chapter 1.4.1, the model allows to calculate the debonded fiber length for each family and each iteration, Eq. 4.17. This debonded fiber length traduces the reduction of fibers length useful for the transmission of the load from the matrix that leads to a reduction of the mechanical properties of the composite. It is reminded that growth of debonded length is directly related to fiber axial strain and so on to fiber orientation with respect to loading direction. Here, a global debonded fibers' length ratio, τ_{LF} , is introduced to take into account the contribution of all fiber media to composite damage by debonding through a single scalar value. Thus, τ_{LF} is computed by summing the relative debonded length for each fiber family, weighted by the corresponding fiber volume fraction (Eq. 4.18).

$$\tau_{LF} = \sum_{\alpha=1}^N \frac{\delta^{\alpha}}{\frac{L}{2}} * v_F^{\alpha} \quad (4.18)$$

It is important to note that this value highly depends on the calculation of the debonded length δ^{α} and thus on values identified for parameters a and b (Eq. 4.17). Yet, it has been seen in Section 4.1.3 that several couples of parameters a and b may lead to a fit with experimental data. Thus, it is not trivial to choose among those values the most judicious couple of parameters. Here, the couple that gave rise to the less abrupt evolution of δ , while leading to an accurate behavior prediction, is chosen (i.e. $a = 0.05$ and $b = 2$).

Notched tensile specimens have been numerically tested using the VUMAT with parameters values identified in the previous section. The mesh (Figure 4.31) contains 4 elements in its thickness with an element size of 0.35 mm. For this simulation, fibers orientation according to the cutting zone is input in the VUMAT. The central node of the bottom surface is clamped and the displacement is set to the central node of the top surface.

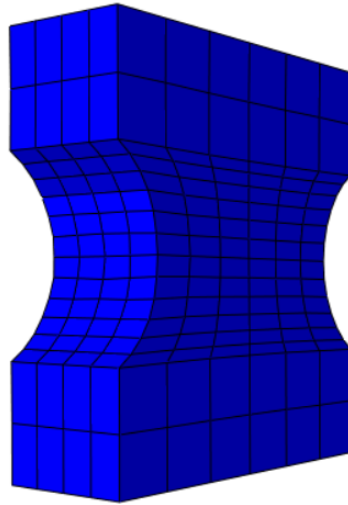


FIGURE 4.31: Mesh of notched tensile specimen

In order to ensure that numerical results are in agreement with experimental results, a comparison between the load vs axial displacement has been done. A reference point is used to extract the load and the axial displacement. The comparison between numerical and experimental results for both materials is plotted in Figure 4.32.

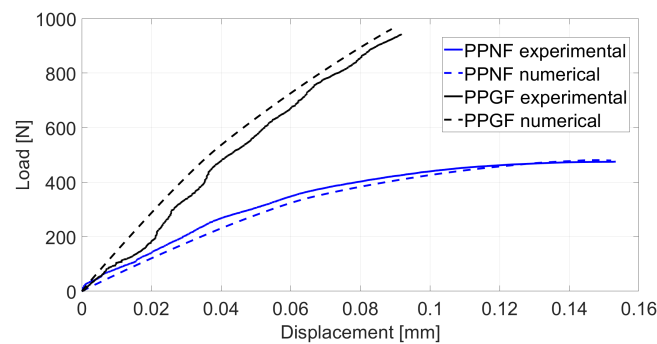


FIGURE 4.32: Comparison between numerical and experimental results

With this figure, one can see that PPNF model best fits experimental data in comparison with PPGF. This is due to the use of real fibers' orientation distribution in the case of PPNF. Thus, in the following, this study focuses on results linked to the PPNF. The evolution of matrix damage behavior and debonded fibers length ratio are analyzed in order to identify phenomena that leads to rupture.

Figure 4.33 shows axial strain calculated with the VUMAT on notched tensile specimens for a displacement of 0.082 mm. The image on the left is a sectional view at mid-thickness.

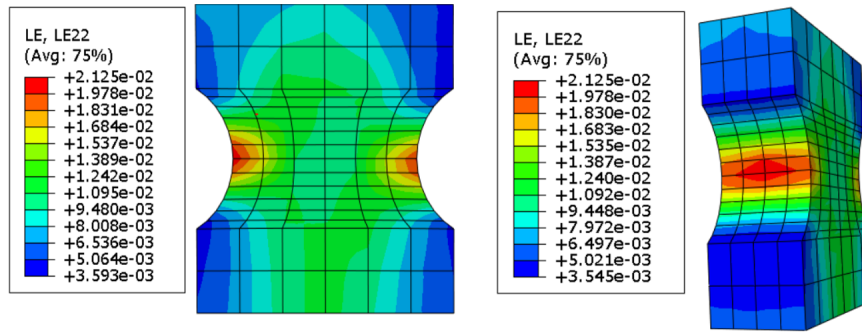


FIGURE 4.33: Sectional view of PPNF numerical axial strain

Numerical results show an axial strain concentration in the middle of the thickness suggesting that the rupture is initiated in the core of the specimen. These results have been observed for both materials. The aim of these simulations is to link the experimental axial strain at break to the numerical value of τ_{LF} . Focus is made on the min and max values and the average value of the axial strain at break, see Table 4.8. However, it is important to recall that during experimental tests, the axial strain has been measured on the surface of the specimens.

Cutting angle	Min. axial strain at break	Max. axial strain at break	Mean axial strain at break
0°	0.03051	0.04172	0.03721
30°	0.03291	0.04221	0.03812
45°	0.03919	0.05639	0.04820

TABLE 4.8: Experimental min and max values and mean value of axial strain at break for the three cutting angles

In view of this, the experimental values of the axial strain (blue crosses) are crossed with the numerical axial strain extracted from an element located on the surface of the specimen. This allows to identify the time step at break initiation, Figure 4.34.

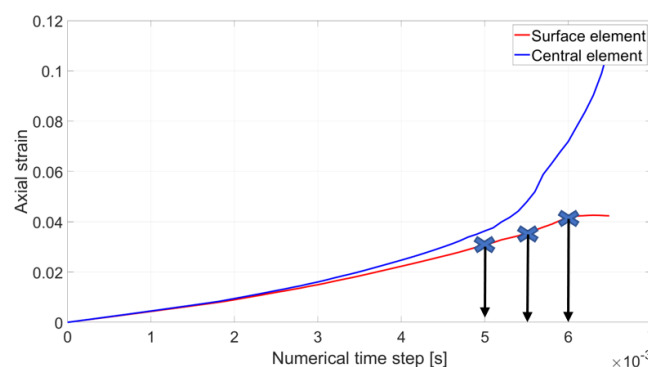


FIGURE 4.34: Identification of time step at break initiation according to experimental axial strain

Once the rupture time step is identified, it is possible to determine the value of τ_{LF} at rupture, in the core of the specimen. To do this, the evolution of τ_{LF} vs the time step is

plotted and the values of τ_{LF} at rupture are identified with previous time steps (black dotted-lines), Figure 4.35. The values obtained for τ_{LF} are summarized in Table 4.9.

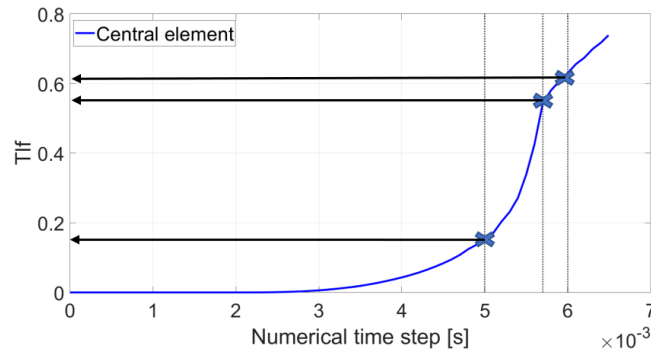


FIGURE 4.35: Identification of τ_{LF} at break

Cutting angle	τ_{LF} Min	τ_{LF} Max	τ_{LF} Mean
0°	0.1534	0.6301	0.5444
30°	0.1214	0.6056	0.2515
45°	0.1083	0.4122	0.2522

TABLE 4.9: Debonded fibers length ratio at break for the three cutting angles (with $a=0.05$ and $b=2$)

One can see that the value of τ_{LF} is maximum when fibers are mainly oriented parallel to the loading direction, in agreement with the assumption that matrix/fibers debonding is maximum in that configuration.

Concerning the evolution of the matrix damage, the same protocole has been applied and the values at break of D are summarized in Table 4.10 for the three cutting angles.

Cutting angle	D Min	D Max	D Mean
0°	0.0078	0.0371	0.0152
30°	0.0096	0.0516	0.0156
45°	0.0148	0.0497	0.0276

TABLE 4.10: Min., max. and mean values of D for the 3 cutting angles

As can be seen, the value of D increases while the cutting angle increases. For example, the mean value of D for the 0° cutting angle is equal to 0.0152 and increase up to 0.0276 for the 45° cutting angle. It is worth to note that the values of D are quite similar and low for the cutting angles of 0° and 30°. This observation is linked to the fact that matrix damage increases as fibers orientation moves away from the loading direction. Indeed, fibers oriented parallel to the loading direction prevent matrix damage. Also, for the 45° cutting angle, it should be noted that not only the value of D is higher than the two other cutting angles but also the value of τ_{LF} is lower than the value corresponding to the two other cutting angles. It indicates that

matrix damage seems to progressively become a predominant damage phenomenon as fiber orientation with respect to loading direction increases, as already highlighted in a previous numerical study [11]. Nevertheless, the values of D calculated by the VUMAT remain quite low in comparison with the values of D obtained with PPNF matrix (up to 0.25, Figure 4.9). This result suggests that for this material and loading case, matrix damage does not play a major role in the failure of the part and can probably be neglected.

The next step of this work is to check if the same values of τ_{LF} are found on bulge tests simulations and to compare numerical results with experimental ones. In view of this, bulge tests are numerically simulated. The perforated plates are meshed with a refinement close to the hole. The mesh is composed of three elements in the thickness of the plate with 80 elements with an element size of 1 mm at the periphery of the hole (Figure 4.36).

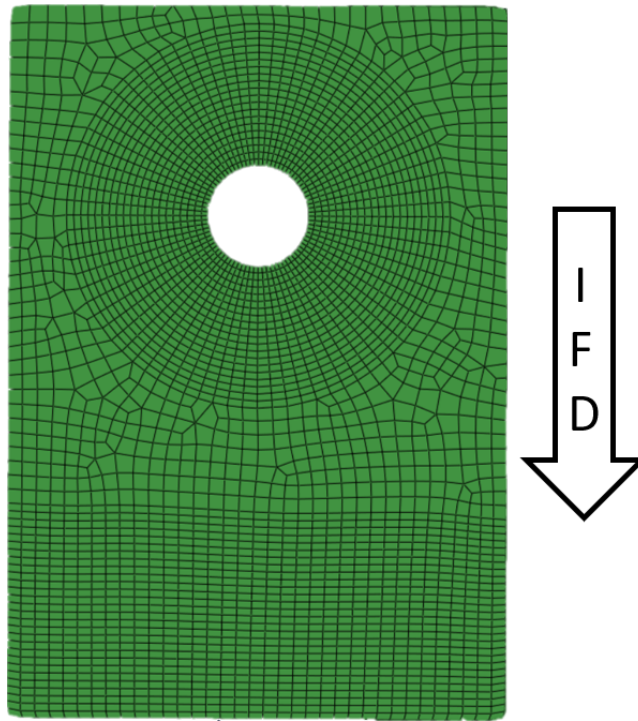


FIGURE 4.36: Mesh of the plate for numerical bulge test

In order to ensure the homogeneity of the results near the hole, the axial displacement of the plate (out-of-plan displacement) is first analyzed (Figure 4.37).

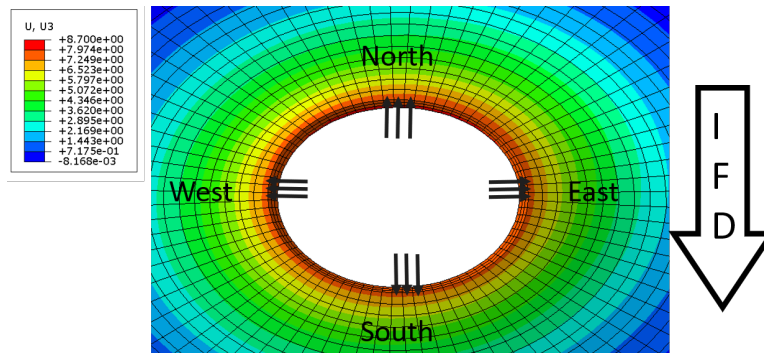


FIGURE 4.37: Axial displacement during numerical bulge test

One can see that the axial displacement is quite similar in all the elements near the hole, which validates the homogeneity of the results for this numerical model. The evolution of D vs the punch displacement is plotted for 3 elements at each side in Figure 4.38.

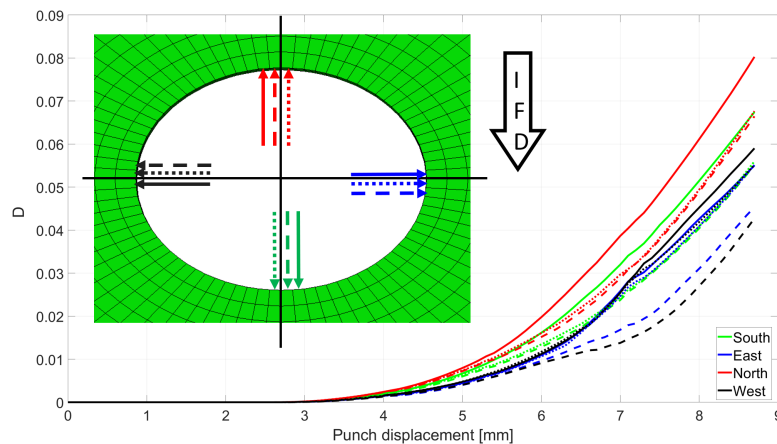
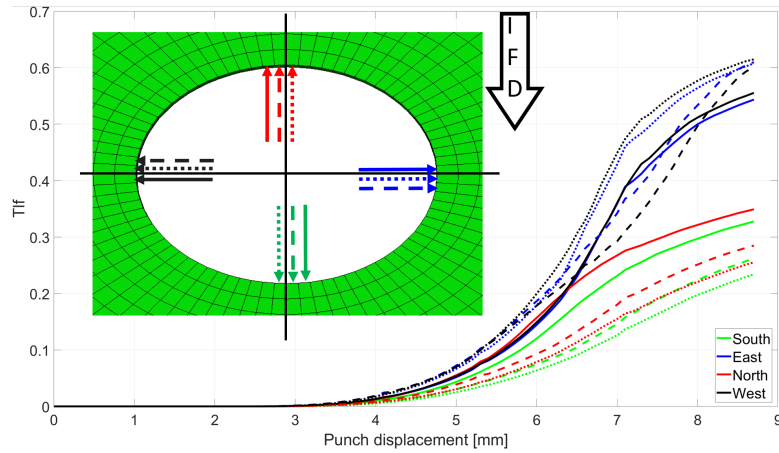


FIGURE 4.38: Evolution of D vs punch displacement for the 4 sides

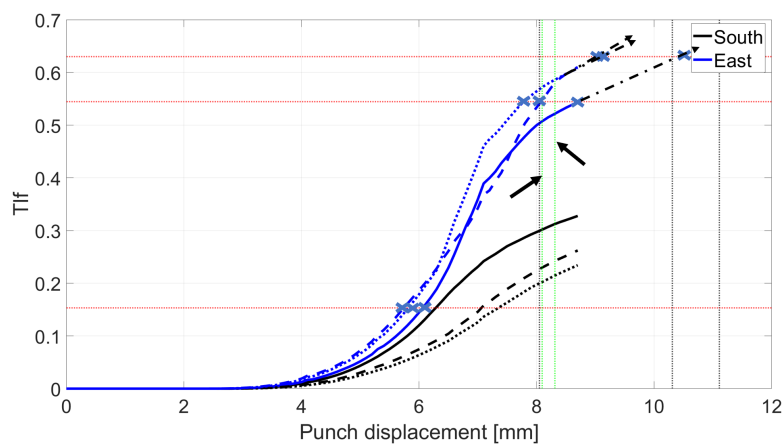
Except for 3 elements, the evolution of D is quite similar between the elements and remains quite low (lower than 0.07) when compared to the value found during cyclic tests performed on the matrix (up to 0.25, Figure 4.9). Then, the evolution of τ_{LF} is calculated for the same 3 elements of each side and the results are plotted on Figure 4.39.

The two black straight lines represent the impact zones where fibers are either oriented most perpendicular to the loading direction (horizontal black straight line) or most parallel to the loading direction (vertical black straight line). It can be seen that the results show partial symmetry. Indeed, east and west sides show the same order of magnitude of τ_{LF} for the 6 elements. Differences can be seen for north and south sides. The difference for the value of τ_{LF} between these elements is explained by fibers orientation. For both sides, the straight curves represent the evolution of τ_{LF} of the farthest element from the black line. It means that both

FIGURE 4.39: Evolution of τ_{LF} vs punch displacement for the 4 sides

elements have fewer fibers oriented perpendicular to the loading than the four others (dashed and dotted curves). Thus, one can see that the evolution of τ_{LF} for these two elements is higher than the others. For the same reason, the evolution of τ_{LF} is more abrupt for the elements located in east and west sides of the hole than elements of south and north sides. The evolution of τ_{LF} measured is therefore logical and in agreement with the results found in Table 4.9.

In the case of a failure criterion based on the value of τ_{LF} (i.e. by neglecting the contribution of matrix damage, which seems relevant regarding low values of D), this observation would indicate that the failure should be in east or west side which is the case of all plates of PPGF and 2 plates of PPNF. Thus, in order to find the numerical punch displacement at break, the evolution of τ_{LF} is compared to the values of τ_{LF} at break identified with the notched tensile specimens. Focus is made on the 3 elements of east and south sides. The evolution of τ_{LF} vs punch displacement of these elements are plotted in Figure 4.40.

FIGURE 4.40: Evolution of τ_{LF} vs punch displacement for east and south sides

By plotting values of τ_{LF} at break obtained with experimental results (red dotted lines), the numerical punch displacement at break is deduced. The 5 vertical dotted lines represent the punch displacement at break for the PPNF plates during experiments and the two black arrows

are pointing the punch displacement of plates 2 and 5 for whom the first two crack appeared in west and then east sides. The three black dashed arrows are manual extrapolations of their τ_{LF} curve. The blue crosses correspond to the intersection between the value of τ_{LF} identified with notched tensile specimens and the evolution of τ_{LF} from the bulge test simulation. The values of the measured numerical punch displacement are summarized in Table 4.11 and experimental punch displacement at first crack initiation in surface identified with the images are summarized in Table 4.12.

Punch displacement [mm]	Element 1	Element 2	Element 3
Min	5.7	5.8	6.1
Mean	8.1	7.8	8.7
Max	9.2	9.1	10.5

TABLE 4.11: Numerical punch displacement according to values of τ_{LF}

	PPNF 1	PPNF 2	PPNF 3	PPNF4	PPNF 5
Punch displacement [mm]	11.11	8.312	10.31	8.096	8.05

TABLE 4.12: Experimental punch displacement at first crack initiation in surface

By comparing the punch displacement of both tables, one can see that the values of the punch displacement identified by using the min τ_{LF} highly under-estimates the experimental displacement. On the contrary, considering the max τ_{LF} slightly over-estimates the experimental displacement if only considering plates 2 and 5. Then, the mean τ_{LF} allows to obtain accurate results. Also, it has been seen with notched tensile specimens that the value identified for the strain at break has a relative standard deviation (the STD divided by the mean) equal to 9.8%. Thus, the numerical punch displacement found may vary with the same coefficient. It should be noted that in order to save computing time, the mesh size for the simulation of the bulge test is higher than the mesh of notched tensile specimens. This analysis made on two different mesh sizes may introduce some error for the identification of τ_{LF} . Indeed, smaller elements allow to analyze more locally the results (here τ_{LF}) and thus to obtain higher and more quickly maximum values.

Despite quite good prediction of punch displacement at failure initiation, some improvements of failure criterion can be proposed. For example, as previously stated, the identification of parameters a and b for the debonding is made by fitting numerical results to experimental results and several couples of the two parameters allow to have good fits. Thus, a first way to further improve numerical results is to define an evolution law of the debonded length with physical foundations. The punch displacement at break is identified with the data directly recorded by the tensile machine. This identification may introduce some error. Also, the fragile nature of the PPNF at high-speed makes the measurement of the real strain at break difficult because it depends on the measurement accuracy.

4.4 Conclusion

In this section, the behavior of SFRT under high-strain-rate loading has been investigated. First, PP-35GF and PP-30NF have been characterized in order to model SFRT VE-VP behavior while taking into account fibers specificities such as orientation and geometrical properties but also matrix / fibers debonding and matrix ductile damage.

Failure behavior of SFRTs has been investigated for both materials through two experimental campaigns. During the first one, tensile tests have been performed with notched tensile specimens. The aim of this special geometry is to force the rupture to happen in the notched area. It has been seen that the strain at break is slightly variable for both materials. Then, bulge tests have been performed on perforated plates. Contrary to the notched tensile specimens, more variabilities have been observed, especially for the PPNF. Indeed, it has been seen that the crack pattern is the same for all the plates in PPGF but is different for the plates in PPNF. Indeed, for the PPNF, there is a risk that the first crack appears at the north or south side if a large fiber or an aggregate of fibers is located near the hole. This case has happened twice during this study.

Numerical simulations have been carried out to identify damage mechanisms that may lead to failure, i.e. matrix / fiber debonding and matrix damage. It has been seen that matrix/fibers debonding is the preponderant mechanism on the rupture. Thus, a failure criterion based on matrix / fiber debonding is proposed. First, the debonding fibers length ratio has been investigated with the notched tensile specimens. This criterion has the advantage of being a scalar value, while taking the contribution of all fibers families, and therefore of local microstructure properties, into account. The evolution of τ_{LF} during high-speed tensile tests on notched specimens has been computed in order to identify critical values that lead to failure. Second, the evolution of τ_{LF} has been studied in the case of the bulge tests. It has been seen that the study of τ_{LF} may indicate the failure zone and approximate the punch displacement at rupture initiation when using the mean values found for τ_{LF} .

By definition, τ_{LF} is directly linked to the evolution of debonded length δ . In the next future, this failure criterion could therefore be improved by defining a more representative evolution law for debonded length δ .

Conclusions and outlooks

Conclusions

The aim of this PhD thesis work was to experimentally quantify the microstructural variability of short glass or natural fiber reinforced composites, especially in terms of fiber geometry and orientation, then to experimentally and numerically analyze their impact on the dynamic behavior. In complement, the influence of injection molding process parameters on these variabilities have been investigated in the case of glass fibers.

The first objective is to study the impact of different types of variability on SFRT Young's modulus. First, the impact of variable injection molding parameters is studied in the case of PPGF. In view of this, the melt and mold temperatures as well as the injection speed are chosen to vary. It has been found that the choice of parameters is not trivial and that some compromises must be made for manufacturers, for example, between the duration of injection cycle and the maximization of Young's modulus. Second, a study of the microstructure of PPNF shows that the **orientation of the fibers varies locally into parts** resulting from injection molding process. The second observation of the microstructural analysis is that although natural fibers have variable geometrical properties, the **range of variation remains quite similar** from one sample to another. Third, the origin of the sources of Young's modulus variability of matrix and composite materials has been investigated by means of the COV. It has been seen that adding glass fibers to thermoplastic matrices slightly increases the variability of composites' Young modulus for the same loading angle. On the other hand, **the variability of composites' Young modulus is significantly increased in the case of natural fibers reinforcement**, as a consequence of high intrinsic variability of numerous natural fibers properties. Nevertheless, the **variability measured at composite scale remains lower than the variability measured at the scale of natural fibers** in the litterature.

The vibration response of the SFRTs has been studied as well as the impact of fibers orientation variability on the first natural frequency of SFRTs. Experimental campaigns showed that the first natural frequency of the plates presents little variability from one plate to another. On the other hand, within the same plate, the results depends on the clamping side, thus underlining the existence of a longitudinal variability. To study the local variation, barrels cut at different locations in a given plate are tested. It allowed, first, to confirm the existence of previously observed **longitudinal variability** and, secondly, to show the existence of a **transverse variability** of vibratory properties within the plate. Microtomographic scans of barrels' subvolumes have highlighted a **direct correlation between fibers' orientation and barrels' first natural frequency**. Finally, different numerical strategies are presented to model the variability of the first natural frequency of barrels. For this purpose, different levels of uncertainties are modeled in order to take into account the variation of fibers orientation at different scales. It has been seen that increasing the precision of numerical results is possible but at the expense of experimental and/or numerical cost. Then, a comparison between PPGF and PPNF has been done. The first natural frequency measured for the PPNF injection molded plates is always lower than that of PPGF injection molded plates. It is explained by the intrinsic lower rigidity of natural fibers in our case. Yet, it has been seen that the variability of the first natural frequency of the barrel is slightly higher for natural fibers (5% for the longitudinal variability of PPNF against 1.8% for PPGF). Moreover, at part scale (here injection plates), the variability for both materials remains low and quite similar (1.17% for PPNF against 0.52% for PPGF). This result allows to have a greater confidence in the use of natural fibers to replace glass fibers as the variability at part scale is not significantly increased.

Finally, as a third objective, the variability of SFRT behavior and rupture under high-strain-rate loadings is studied. In view of this, the behavior of both materials is first characterized in order to find the inputs for numerical simulations. Then, the failure of SFRT is studied through two experimental campaigns, one with tensile tests on notched tensile specimens and the other with bulge tests on perforated plates. Tensile tests enabled to study more deeply the phenomenon of rupture. Indeed, notches allow strain concentration in the middle part of the specimen and therefore ensure that failure initiates in this area. The tests showed **little variability of strain at break** for both materials. The analysis of the tests allowed to set up a **failure criterion based on debonded fiber length ratio**. The punch displacement during bulge tests has shown more variability between both materials than the strain at break during tensile tests performed on notched tensile specimens, and especially for the PPNF. The results from the bulge tests on PPGF are very similar from one plate to another with the same failure pattern and the same punch displacement before failure initiation. At the contrary, the failure pattern of PPNF plates varied. It has been related to more variable microstructural properties

and/or higher presence of defects in that material, compared to PPGF. Finally, the **failure criterion presented above allows identifying the "classical" failure** (in the western or eastern zone) **of the bulge tests** but not the failures in the southern or northern zone. Thus, this failure criterion allows to predict the failure initiation zone for materials with controlled geometrical properties.

In summary, it has been seen that the **local fiber orientation drastically impacts SFRTs' mechanical behavior**, whatever the nature of fibers. On the contrary, the impact of the variability of geometrical properties of natural fibers appeared to be more moderate. Thus, according to author, **taking into account the local fibers orientation in numerical simulation would constitute a huge improvement of accuracy of the numerical prediction of the industrial partner**, thus allowing to boost the use of natural fibers in its technical parts.

Outlooks

In this PhD thesis, a focus has mainly been made on the uncertainty quantification of natural fibers properties as well as of their orientations in short-fiber-reinforced thermoplastics through various experimental campaigns. The next steps will be to model the observed uncertainty with the probabilistic theory and to propagate them on the mechanical quantities of interest, for example with a polynomial chaos expansion method. A recent work [101], complementary to our ones, discussed of the probability distributions of fibers' Young modulus, not identified here, the same study should be applied to the IFSS. Next, the analysis of Sobol indices will allow to evaluate the effect of natural fibers properties on the macroscopic ones of the thermoplastics. This non-deterministic strategy could easily be applied for the modal analysis, especially for the first frequency. However, the task will be more complex for the dynamic analysis, for which the failure criterion is currently not enough predictive. Thus, improvement should be done with the failure criterion presented in Chapter 4.

As a reminder, the failure criterion proposed in this study is based on an evolution law of matrix / fiber debonded length without physical foundation. Thus, it seems necessary to develop a better modelling of debonding mechanisms. For this, in-situ tests under micro tomograph with sufficient resolution to observe the initiation and evolution of matrix / fiber debonding could be considered. This would make it possible to measure the evolution of the debonding and thus establish a more representative law.

The failure criterion proposed here allows identifying the failure initiation zone in the case of materials with controlled microstructure. Yet, in case of natural fibers, some microstructure variations (clusters, defects...) are randomly dispersed in the part. The exact location of failure could be predicted if those variations were taken into account in FE model, which seems impossible in practice. Yet, the failure criterion could be improved to predict a macroscopic quantity at failure (for instance punch displacement at failure initiation for bulge tests), taking into account those randomly dispersed microstructure variation in the part.

Other improvements may concern some microstructure specificities related to the constraints imposed by the injection molding process, and especially the presence of weld lines. To highlight the impact of this phenomenon, experimental tests on plates injected with a hole have been performed. The presence of the hole forces the melt flow to split in two in order to get around the hole. The weld line appears on the downstream of the hole where the two branches of the melt flow meet up (Figure 4.41).

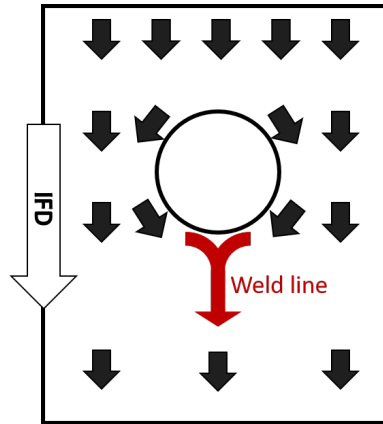


FIGURE 4.41: Schematic representation of the formation of a weld line

It has been identified that the first crack always occurs at the weld line for both materials. A weld line leads to local weakening of material properties and is therefore always the preferential zone of rupture initiation, whatever the nature of fibers (Tables 4.13 and 4.14).

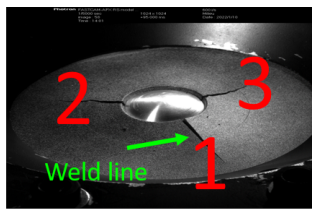
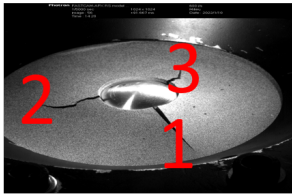
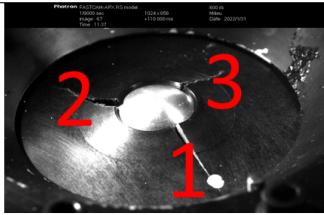

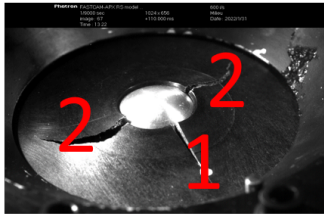
PPGF		
		
		

TABLE 4.13: Crack order for PPGF with welding line

Then, concerning the appearance of the other cracks, it can be seen that the same pattern of failure occurs for the plates made in PP-35GF but not for the plates made in PP-30NF. Also, in the case of the PP-30NF, one plate over six presents tree cracks instead of four. It is thus observed that the variability related to natural fibers impacts the order of appearance of the following cracks but also the number of cracks.

Always in the perspective of improving the failure criterion, it seems interesting to study more deeply matrix damage. In the proposed criterion, matrix damage is neglected. This assumption is probably wrong for materials with less fibers (i.e. more proportion of matrix). Indeed, less fiber induces a greater importance of matrix mechanical response on composite

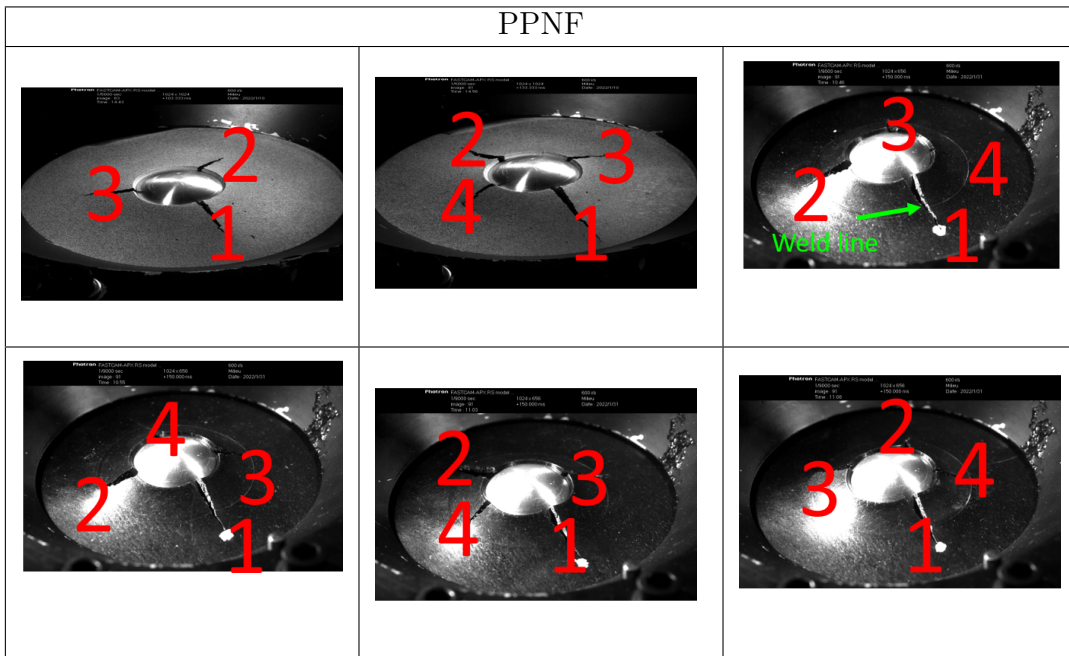


TABLE 4.14: Crack order for PPNF with welding line

mechanical behavior and thus, a more important matrix damage. Matrix damage is also likely to be more important in other kinds of loading than those analyzed in this work, as suggested by the increase of damage value in notched specimens at 45° (even moderate in the present case). The present failure criterion should evolve in order to take into account matrix damage.

Bibliography

- [1] K. Tabit, *Elaboration des matériaux aluminosilicates à base d'anorthite, de cordiérite et de zéolite Na-P1 à partir des cendres volantes et des scories Optimisation, caractérisation et propriétés*. PhD thesis, Université Cadi Ayyad, Oct. 2019.
- [2] C. Felgueiras, N. G. Azoia, C. Gonçalves, M. Gama, and F. Dourado, "Trends on the Cellulose-Based Textiles: Raw Materials and Technologies," *Frontiers in Bioengineering and Biotechnology*, vol. 9, p. 608826, Mar. 2021.
- [3] H. L. Bos, J. Müssig, and M. J. A. van den Oever, "Mechanical properties of short-flax-fibre reinforced compounds," *Composites Part A: Applied Science and Manufacturing*, vol. 37, pp. 1591–1604, Oct. 2006.
- [4] G.-H. Oh, J.-H. Jeong, S.-H. Park, and H.-S. Kim, "Terahertz time-domain spectroscopy of weld line defects formed during an injection moulding process," *Composites Science and Technology*, vol. 157, pp. 67–77, Mar. 2018.
- [5] D.-A. Serban, "Viscoplastic Behaviour of Polyamides," in *Viscoelastic and Viscoplastic Materials* (M. F. El-Amin, ed.), InTech, Sept. 2016.
- [6] B. Enciso, J. Abenojar, and M. A. Martínez, "Influence of plasma treatment on the adhesion between a polymeric matrix and natural fibres," *Cellulose*, vol. 24, pp. 1791–1801, Apr. 2017.
- [7] C. Eberhardt, A. Clarke, M. Vincent, T. Giroud, and S. Flouret, "Fibre-orientation measurements in short-glass-fibre composites—II: a quantitative error estimate of the 2D image analysis technique," *Composites Science and Technology*, vol. 61, pp. 1961–1974, Oct. 2001.
- [8] N. L. Moigne, M. v. d. Oever, and T. Budtova, "A statistical analysis of fibre size and shape distribution after compounding in composites reinforced by natural fibres," *Composites Part A: Applied Science and Manufacturing*, vol. 42, pp. 1542–1550, Oct. 2011.

- [9] C. Baley, “Analysis of the flax fibres tensile behaviour and analysis of the tensile stiffness increase,” *Composites Part A: Applied Science and Manufacturing*, vol. 33, pp. 939–948, July 2002.
- [10] M. Vincent, T. Giroud, A. Clarke, and C. Eberhardt, “Description and modeling of fiber orientation in injection molding of fiber reinforced thermoplastics,” *Polymer*, vol. 46, pp. 6719–6725, Aug. 2005.
- [11] D. Notta-Cuvier, M. Nciri, F. Lauro, R. Delille, F. Chaari, F. Robache, G. Haugou, and Y. Maalej, “Coupled influence of strain rate and heterogeneous fibre orientation on the mechanical behaviour of short-glass-fibre reinforced polypropylene,” *Mechanics of Materials*, vol. 100, pp. 186–197, Sept. 2016.
- [12] S. Dey, T. Mukhopadhyay, H. H. Khodaparast, and S. Adhikari, “Fuzzy uncertainty propagation in composites using Gram–Schmidt polynomial chaos expansion,” *Applied Mathematical Modelling*, vol. 40, pp. 4412–4428, Apr. 2016.
- [13] P. P. Camanho, “Failure criteria for fibre-reinforced polymer composites,” p. 13, 2002.
- [14] European commission, “A european strategy for plastics in a circular economy,” tech. rep., 2018.
- [15] J. Proy, F. Massa, D. Notta-Cuvier, F. Lauro, T. Tison, and G. Spingler, “Integrating fibers and injection molding process variability in short-natural-fiber-reinforced thermoplastics behavior: A review,” *Materials Today Communications*, vol. 29, p. 102785, Dec. 2021.
- [16] S. Joshi, L. Drzal, A. Mohanty, and S. Arora, “Are natural fiber composites environmentally superior to glass fiber reinforced composites?,” *Composites Part A: Applied Science and Manufacturing*, vol. 35, pp. 371–376, Mar. 2004.
- [17] R. Jeyapragash, V. Srinivasan, and S. Sathiyamurthy, “Mechanical properties of natural fiber/particulate reinforced epoxy composites – A review of the literature,” *Materials Today: Proceedings*, vol. 22, pp. 1223–1227, Jan. 2020.
- [18] J. Müssig, ed., *Industrial application of natural fibres: structure, properties and technical applications*. Wiley series in renewable resources, Chichester: Wiley, 2010.
- [19] D. page, F. Elhosseiny, K. Winkler, and A. P. S. Lancaster, “Elastic modulus of single wood pulp fibers,” *Tappi*, vol. 60, n^o4, p. 114–117., 1977.
- [20] M. Groß, J. Dietzsch, and C. Rübiger, “Non-isothermal energy–momentum time integrations with drilling degrees of freedom of composites with viscoelastic fiber bundles and

- curvature–twist stiffness,” *Computer Methods in Applied Mechanics and Engineering*, vol. 365, p. 112973, June 2020.
- [21] A. T. Talib, C. Chang Jie, M. A. P. Mohammed, A. Samsu Baharuddin, M. N. Mokhtar, and M. Wakisaka, “On the nonlinear viscoelastic behaviour of fresh and dried oil palm mesocarp fibres,” *Biosystems Engineering*, vol. 186, pp. 307–322, Oct. 2019.
- [22] M. S. Sreekala, M. G. Kumaran, and S. Thomas, “Stress relaxation behaviour in oil palm fibres,” *Materials Letters*, vol. 50, pp. 263–273, Sept. 2001.
- [23] V. Placet, F. Trivaudey, O. Cisse, V. Gucheret-Retel, and M. L. Boubakar, “Diameter dependence of the apparent tensile modulus of hemp fibres: A morphological, structural or ultrastructural effect?,” *Composites Part A: Applied Science and Manufacturing*, vol. 43, pp. 275–287, Feb. 2012.
- [24] E. Richely, A. Bourmaud, V. Placet, S. Guessasma, and J. Beaugrand, “A critical review of the ultrastructure, mechanics and modelling of flax fibres and their defects,” *Progress in Materials Science*, vol. 124, p. 100851, Feb. 2022.
- [25] J.-F. Agassant, P. Avenas, J.-P. Sergent, B. Vergnes, and M. Vincent, “La mise en forme des matières plastiques,” p. 500.
- [26] Y.-K. Shen, C.-W. Wu, Y.-F. Yu, and H.-W. Chung, “Analysis for optimal gate design of thin-walled injection molding,” *International Communications in Heat and Mass Transfer*, vol. 35, pp. 728–734, July 2008.
- [27] A. Ayadi, *Modélisation et analyses expérimentales basées sur la caractérisation microstructurale par imageries à rayons X. Application aux composites thermoplastiques renforcés par des fibres de verre courtes*. PhD thesis, Sept. 2016.
- [28] B. Ozcelik, E. Kuram, and M. M. Topal, “Investigation the effects of obstacle geometries and injection molding parameters on weld line strength using experimental and finite element methods in plastic injection molding,” *International Communications in Heat and Mass Transfer*, vol. 39, pp. 275–281, Feb. 2012.
- [29] A. Megally, “Étude et modélisation de l’orientation de fibres dans des thermoplastiques renforcés,”
- [30] G. West, “On the resistance to the motion of a thread of mercury in a glass tube,” *Proceedings of the Royal Society of London. Series A, Containing Papers of a Mathematical and Physical Character*, vol. 86, pp. 20–25, Dec. 1911.

- [31] A. Bechara, S. Kollert, J. Onken, D. Ramírez, and T. Osswald, “Effect of fountain flow on fiber orientation and distribution in fiber filled polymers during mold filling,” p. 5.
- [32] M. Baltussen, M. Hulsen, and G. Peters, “Numerical simulation of the fountain flow instability in injection molding,” *Journal of Non-Newtonian Fluid Mechanics*, vol. 165, pp. 631–640, June 2010.
- [33] H. Mavridis, A. N. Hrymak, and J. Vlachopoulos, “The Effect of Fountain Flow on Molecular Orientation in Injection Molding,” *Journal of Rheology*, vol. 32, pp. 639–663, Aug. 1988.
- [34] Z. Tadmor, “Molecular orientation in injection molding,” *Journal of Applied Polymer Science*, vol. 18, pp. 1753–1772, June 1974.
- [35] M. Gupta and K. K. Wang, “Fiber orientation and mechanical properties of short-fiber-reinforced injection-molded composites: Simulated and experimental results,” *Polymer Composites*, vol. 14, pp. 367–382, Oct. 1993.
- [36] M. R. Kantz, H. D. Newman, and F. H. Stigale, “The skin-core morphology and structure–property relationships in injection-molded polypropylene,” *Journal of Applied Polymer Science*, vol. 16, pp. 1249–1260, May 1972.
- [37] H. Rolland, N. Saintier, N. Lenoir, A. King, and G. Robert, “Fatigue mechanisms description in short glass fibre reinforced thermoplastic by microtomographic observations,” *Procedia Structural Integrity*, vol. 2, pp. 301–308, 2016.
- [38] S. Kenig, “Fiber orientation development in molding of polymer composites,” *Polymer Composites*, vol. 7, pp. 50–55, Feb. 1986.
- [39] R. S. Bay and C. L. Tucker, “Fiber orientation in simple injection moldings. Part II: Experimental results,” *Polymer Composites*, vol. 13, pp. 332–341, Aug. 1992.
- [40] R. S. Bay and C. L. Tucker, “Fiber orientation in simple injection moldings. Part I: Theory and numerical methods,” *Polymer Composites*, vol. 13, pp. 317–331, Aug. 1992.
- [41] J. Brezinová and A. Guzanová, “Friction Conditions during the Wear of Injection Mold Functional Parts in Contact with Polymer Composites,” *Journal of Reinforced Plastics and Composites*, vol. 29, pp. 1712–1726, June 2010.
- [42] A. S. Lodge, M. Renardy, J. A. Nohel, and U. of Wisconsin-Madison, eds., *Viscoelasticity and rheology*. Publication no. 53 of the Mathematics Research Center, the University of Wisconsin–Madison, Orlando, Fla: Academic Press, 1985.

- [43] D.-A. Wang and J. Pan, "A non-quadratic yield function for polymeric foams," *International Journal of Plasticity*, vol. 22, pp. 434–458, Mar. 2006.
- [44] E. Ghorbel, "A viscoplastic constitutive model for polymeric materials," *International Journal of Plasticity*, vol. 24, pp. 2032–2058, Nov. 2008.
- [45] J. A. Sauer and K. D. Pae, "The flow of solid polymers under high pressure," *Colloid and Polymer Science*, vol. 252, pp. 680–695, Sept. 1974.
- [46] R. Raghava, R. M. Caddell, and G. S. Y. Yeh, "The macroscopic yield behaviour of polymers," *Journal of Materials Science*, vol. 8, pp. 225–232, Feb. 1973.
- [47] R. Balieu, F. Lauro, B. Bennani, R. Delille, T. Matsumoto, and E. Mottola, "A fully coupled elastoviscoplastic damage model at finite strains for mineral filled semi-crystalline polymer," *International Journal of Plasticity*, vol. 51, pp. 241–270, Dec. 2013.
- [48] J. Zhang, N. Kikuchi, V. Li, A. Yee, and G. Nusholtz, "Constitutive modeling of polymeric foam material subjected to dynamic crash loading," *International Journal of Impact Engineering*, vol. 21, pp. 369–386, May 1998.
- [49] C. Zhang and I. D. Moore, "Nonlinear mechanical response of high density polyethylene. Part I: Experimental investigation and model evaluation," *Polymer Engineering & Science*, vol. 37, pp. 404–413, Feb. 1997.
- [50] S.-L. Bai, C. G'Sell, J.-M. Hiver, and C. Mathieu, "Polypropylene/polyamide 6/polyethylene-octene elastomer blends. Part 3. Mechanisms of volume dilatation during plastic deformation under uniaxial tension," *Polymer*, vol. 46, pp. 6437–6446, Aug. 2005.
- [51] C. G'Sell, J. M. Hiver, and A. Dahoun, "Experimental characterization of deformation damage in solid polymers under tension, and its interrelation with necking," *International Journal of Solids and Structures*, vol. 39, pp. 3857–3872, June 2002.
- [52] M. Jerabek, Z. Major, K. Renner, J. Móczó, B. Pukánszky, and R. W. Lang, "Filler/matrix-debonding and micro-mechanisms of deformation in particulate filled polypropylene composites under tension," *Polymer*, vol. 51, pp. 2040–2048, Apr. 2010.
- [53] R. Balieu, F. Lauro, B. Bennani, T. Matsumoto, and E. Mottola, "Non-associated viscoplasticity coupled with an integral-type nonlocal damage model for mineral filled semi-crystalline polymers," *Computers & Structures*, vol. 134, pp. 18–31, Apr. 2014.
- [54] B. Mouhmid, A. Imad, N. Benseddiq, S. Benmedakhène, and A. Maazouz, "A study of the mechanical behaviour of a glass fibre reinforced polyamide 6,6: Experimental investigation," *Polymer Testing*, vol. 25, pp. 544–552, June 2006.

- [55] D.-H. Kim, S.-Y. Kang, H.-J. Kim, and H.-S. Kim, "Strain rate dependent mechanical behavior of glass fiber reinforced polypropylene composites and its effect on the performance of automotive bumper beam structure," *Composites Part B: Engineering*, vol. 166, pp. 483–496, June 2019.
- [56] M. Eftekhari and A. Fatemi, "Creep behavior and modeling of neat, talc-filled, and short glass fiber reinforced thermoplastics," *Composites Part B: Engineering*, vol. 97, pp. 68–83, July 2016.
- [57] D. Notta-Cuvier, F. Lauro, B. Bennani, and M. Nciri, "Impact of natural variability of flax fibres properties on mechanical behaviour of short-flax-fibre-reinforced polypropylene," *Journal of Materials Science*, vol. 51, pp. 2911–2925, Mar. 2016.
- [58] W. H. Bowyer and M. G. Bader, "On the re-inforcement of thermoplastics by imperfectly aligned discontinuous fibres," p. 7.
- [59] X. Yan and S. Cao, "Structure and interfacial shear strength of polypropylene-glass fiber/carbon fiber hybrid composites fabricated by direct fiber feeding injection molding," *Composite Structures*, vol. 185, pp. 362–372, Feb. 2018.
- [60] S. Y. Fu, B. Lauke, E. Mäder, C. Y. Yue, and X. Hu, "Tensile properties of short-glass-fiber- and short-carbon-fiber-reinforced polypropylene composites," *Composites Part A: Applied Science and Manufacturing*, vol. 31, pp. 1117–1125, Oct. 2000.
- [61] M. Jing, J. Che, S. Xu, Z. Liu, and Q. Fu, "The effect of surface modification of glass fiber on the performance of poly(lactic acid) composites: Graphene oxide vs. silane coupling agents," *Applied Surface Science*, vol. 435, pp. 1046–1056, Mar. 2018.
- [62] H.-S. Kim, B.-H. Lee, S.-W. Choi, S. Kim, and H.-J. Kim, "The effect of types of maleic anhydride-grafted polypropylene (MAPP) on the interfacial adhesion properties of bio-flour-filled polypropylene composites," *Composites Part A: Applied Science and Manufacturing*, vol. 38, pp. 1473–1482, June 2007.
- [63] S. Mishra, J. B. Naik, and Y. P. Patil, "The compatibilising effect of maleic anhydride on swelling and mechanical properties of plant-fiber-reinforced novolac composites," *Composites Science and Technology*, vol. 60, pp. 1729–1735, July 2000.
- [64] A. Madra, J. Adrien, P. Breitkopf, E. Maire, and F. Trochu, "A clustering method for analysis of morphology of short natural fibers in composites based on X-ray microtomography," *Composites Part A: Applied Science and Manufacturing*, vol. 102, pp. 184–195, Nov. 2017.

- [65] A. Etaati, H. Wang, S. Pather, Z. Yan, and S. Abdanan Mehdizadeh, “3D X-ray microtomography study on fibre breakage in noil hemp fibre reinforced polypropylene composites,” *Composites Part B: Engineering*, vol. 50, pp. 239–246, July 2013.
- [66] S. Mahadevan and S. Sarkar, “Uncertainty analysis methods,”
- [67] Y. Cui, K. Lin, and Y. Chen, “A generalized model for static fatigue lifetime evaluation of optical fibers to reduce the model uncertainty,” *Applied Mathematical Modelling*, vol. 88, pp. 731–742, Dec. 2020.
- [68] A. Thuault, “Approche multi-échelle de la structure et du comportement mécanique de la fibre de lin Multiscale approach of the structure and the mechanical behaviour of the flax fibre,” 2011. Publisher: Unpublished.
- [69] J. L. Thomason, J. Carruthers, J. Kelly, and G. Johnson, “Fibre cross-section determination and variability in sisal and flax and its effects on fibre performance characterisation,” *Composites Science and Technology*, vol. 71, pp. 1008–1015, May 2011.
- [70] K. Charlet, J.-P. Jernot, J. Breard, and M. Gomina, “Scattering of morphological and mechanical properties of flax fibres,” *Industrial Crops and Products*, vol. 32, pp. 220–224, Nov. 2010.
- [71] M. E. Andrieu, M. A. Beakou, U. de Clermont-Ferrand, M. C. Baley, M. de Conférence, U. de Bretagne-Sud, M. J. Breard, M. M. Gomina, M. I. Verpoest, and M. J.-P. Jernot, “Contribution à l’étude de composites unidirectionnels renforcés par des fibres de lin : relation entre la microstructure de la fibre et ses propriétés mécaniques,” p. 182.
- [72] J. Andersons, E. Poriķe, and E. Spārniņš, “The effect of mechanical defects on the strength distribution of elementary flax fibres,” *Composites Science and Technology*, vol. 69, pp. 2152–2157, Oct. 2009.
- [73] K.-T. Lau, P.-Y. Hung, M.-H. Zhu, and D. Hui, “Properties of natural fibre composites for structural engineering applications,” *Composites Part B: Engineering*, vol. 136, pp. 222–233, Mar. 2018.
- [74] K. Kaack, K.-U. Schwarz, and P. Brander, “Variation in morphology, anatomy and chemistry of stems of *Miscanthus* genotypes differing in mechanical properties,” *Industrial Crops and Products*, vol. 17, pp. 131–142, Mar. 2003.
- [75] C. Mattrand, A. Béakou, and K. Charlet, “Numerical modeling of the flax fiber morphology variability,” *Composites Part A: Applied Science and Manufacturing*, vol. 63, pp. 10–20, Aug. 2014.

- [76] M. W. Darlington and A. C. Smith, "Some features of the injection molding of short fiber reinforced thermoplastics in center sprue-gated cavities," *Polymer Composites*, vol. 8, pp. 16–21, Feb. 1987.
- [77] T. D. Papathanasiou, "4 - Flow-induced alignment in injection molding of fiber-reinforced polymer composites," in *Flow-Induced Alignment in Composite Materials* (T. D. Papathanasiou and D. C. Guell, eds.), Woodhead Publishing Series in Composites Science and Engineering, pp. 112–165, Woodhead Publishing, Jan. 1997.
- [78] P. Bright, "A study of the effect of injection speed on fibre orientation in simple mouldings of short glass fibre-filled polypropylene," p. 10.
- [79] P. Shokri and N. Bhatnagar, "Effect of packing pressure on fiber orientation in injection molding of fiber-reinforced thermoplastics," *Polymer Composites*, vol. 28, pp. 214–223, Apr. 2007.
- [80] P. Shokri and N. Bhatnagar, "Effect of the Post-Filling Stage on Fiber Orientation at the Mid-Plane in Injection Molding of Reinforced Thermoplastics," *Physics Procedia*, vol. 25, pp. 79–85, Jan. 2012.
- [81] M. Vincent and J. F. Agassant, "Experimental study and calculations of short glass fiber orientation in a center gated molded disc," *Polymer Composites*, vol. 7, pp. 76–83, Apr. 1986.
- [82] C. L. Tucker, "Flow regimes for fiber suspensions in narrow gaps," *Journal of Non-Newtonian Fluid Mechanics*, vol. 39, pp. 239–268, Jan. 1991.
- [83] S. Ranganathan and S. G. Advani, "A simultaneous solution for flow and fiber orientation in axisymmetric diverging radial flow," *Journal of Non-Newtonian Fluid Mechanics*, vol. 47, pp. 107–136, June 1993.
- [84] D. Masato, J. Rathore, M. Sorgato, S. Carmignato, and G. Lucchetta, "Analysis of the shrinkage of injection-molded fiber-reinforced thin-wall parts," *Materials & Design*, vol. 132, pp. 496–504, Oct. 2017.
- [85] J. W. Gillespie, J. A. Vanderschuren, and R. B. Pipes, "Process induces fiber orientation: Numerical simulation with experimental verification," *Polymer Composites*, vol. 6, pp. 82–86, Apr. 1985.
- [86] D. Notta-Cuvier, F. Lauro, and B. Bennani, "Modelling of progressive fibre/matrix debonding in short-fibre reinforced composites up to failure," *International Journal of Solids and Structures*, vol. 66, pp. 140–150, Aug. 2015.

- [87] S. Liang, “Etude de comportement en fatigue des composites renforcés par fibres végétales: prise en compte de la variabilité des propriétés,” p. 243.
- [88] M. A. Laribi, S. Tamboura, J. Fitoussi, M. Shirinbayan, R. T. Bi, A. Tcharkhtchi, and H. B. Dali, “Microstructure dependent fatigue life prediction for short fibers reinforced composites: Application to sheet molding compounds,” *International Journal of Fatigue*, vol. 138, p. 105731, Sept. 2020.
- [89] M. F. M. Alkbir, S. M. Sapuan, A. A. Nuraini, and M. R. Ishak, “Fibre properties and crashworthiness parameters of natural fibre-reinforced composite structure: A literature review,” *Composite Structures*, vol. 148, pp. 59–73, July 2016.
- [90] M. Fontana, A. L. Araujo, and J. F. A. Madeira, “Optimization of a thin-walled composite crash absorber,” *Thin-Walled Structures*, vol. 155, p. 106826, Oct. 2020.
- [91] D. E. Sommer, D. Thomson, O. Falcó, G. Quino, H. Cui, and N. Petrinic, “Damage modelling of carbon fibre composite crush tubes: Numerical simulation and experimental validation of drop weight impact,” *Composites Part A: Applied Science and Manufacturing*, vol. 160, p. 107033, Sept. 2022.
- [92] H. K. Kim, J. Kim, D. Kim, Y. Ryu, and S. W. Cha, “Vibration and Sound Response of Glass-Fiber-Reinforced Polyamide 6 Using Microcellular-Foaming-Process-Applied Injection Molding Process,” *Polymers*, vol. 14, p. 173, Jan. 2022.
- [93] K. Senthil Kumar, I. Siva, P. Jeyaraj, J. Winowlin Jappes, S. Amico, and N. Rajini, “Synergy of fiber length and content on free vibration and damping behavior of natural fiber reinforced polyester composite beams,” *Materials & Design (1980-2015)*, vol. 56, pp. 379–386, Apr. 2014.
- [94] C. Khoulood, *Analyse du comportement en vibration des matériaux composites à fibres végétales*. PhD thesis.
- [95] D. Spahr, K. Friedrich, J. Schultz, and R. Bailey, “Microstructure and fracture behaviour of short and long fibre-reinforced polypropylene composites,” *Journal of materials science*, vol. 25, p. 13, 1990.
- [96] J. L. Thomason and M. A. Vlug, “Influence of fibre length and concentration on the properties of glass fibre-reinforced polypropylene: 1. Tensile and flexural modulus,” *Composites Part A: Applied Science and Manufacturing*, vol. 27, pp. 477–484, Jan. 1996.
- [97] A. Bernasconi and F. Cosmi, “Analysis of the dependence of the tensile behaviour of a short fibre reinforced polyamide upon fibre volume fraction, length and orientation,” *Procedia Engineering*, vol. 10, pp. 2129–2134, 2011.

- [98] J. Hohe, H. Paul, and C. Beckmann, “A probabilistic elasticity model for long fiber reinforced thermoplastics with uncertain microstructure,” *Mechanics of Materials*, vol. 122, pp. 118–132, July 2018.
- [99] M. T. Piovan and R. Sampaio, “Parametric and non-parametric probabilistic approaches in the mechanics of thin-walled composite curved beams,” *Thin-Walled Structures*, vol. 90, pp. 95–106, May 2015.
- [100] P. A. Hessman, T. Riedel, F. Welschinger, K. Hornberger, and T. Böhlke, “Microstructural analysis of short glass fiber reinforced thermoplastics based on x-ray micro-computed tomography,” *Composites Science and Technology*, vol. 183, p. 107752, Oct. 2019.
- [101] B. Sala, P. Surkova, M. Sanctorum, V. Guicheret-Retel, F. Trivaudey, L. Boubakar, and V. Placet, “Variability in the elastic and time-delayed properties of structural hemp fibre composites,” *Composites Part A: Applied Science and Manufacturing*, vol. 161, p. 107116, Oct. 2022.
- [102] G. Terejanu, P. Singla, T. Singh, and P. D. Scott, “Approximate interval method for epistemic uncertainty propagation using Polynomial Chaos and evidence theory,” in *Proceedings of the 2010 American Control Conference*, (Baltimore, MD), pp. 349–354, IEEE, June 2010.
- [103] S. Naskar, T. Mukhopadhyay, and S. Sriramula, “Spatially varying fuzzy multi-scale uncertainty propagation in unidirectional fibre reinforced composites,” *Composite Structures*, vol. 209, pp. 940–967, Feb. 2019.
- [104] I. Babuška and M. Motamed, “A fuzzy-stochastic multiscale model for fiber composites: A one-dimensional study,” *Computer Methods in Applied Mechanics and Engineering*, vol. 302, pp. 109–130, Apr. 2016.
- [105] F. Massa, K. Ruffin, T. Tison, and B. Lallemand, “A complete method for efficient fuzzy modal analysis,” *Journal of Sound and Vibration*, vol. 309, pp. 63–85, Jan. 2008.
- [106] K. F. Sodoke, L. Laperrière, L. Toubal, and R. S. Khakestar, “Fuzzy logic response to Young’s modulus characterization of a flax–epoxy natural fiber composite,” *Materials & Design*, vol. 89, pp. 273–285, Jan. 2016.
- [107] M. A. Alazwari and S. S. Rao, “Modeling and analysis of composite laminates in the presence of uncertainties,” *Composites Part B: Engineering*, vol. 161, pp. 107–120, Mar. 2019.

- [108] S. S. Rao and X. T. Liu, “Universal Grey System Theory for Analysis of Uncertain Structural Systems,” *AIAA Journal*, vol. 55, pp. 3966–3979, Nov. 2017.
- [109] K. Sepahvand, M. Scheffler, and S. Marburg, “Uncertainty quantification in natural frequencies and radiated acoustic power of composite plates: Analytical and experimental investigation,” *Applied Acoustics*, vol. 87, pp. 23–29, Jan. 2015.
- [110] K. Sepahvand, “Spectral stochastic finite element vibration analysis of fiber-reinforced composites with random fiber orientation,” *Composite Structures*, vol. 145, pp. 119–128, June 2016.
- [111] R. Ghanem, “Hybrid Stochastic Finite Elements and Generalized Monte Carlo Simulation,” *Journal of Applied Mechanics*, vol. 65, pp. 1004–1009, Dec. 1998.
- [112] S.-P. Lee, J.-W. Jin, and K.-W. Kang, “Probabilistic analysis for mechanical properties of glass/epoxy composites using homogenization method and Monte Carlo simulation,” *Renewable Energy*, vol. 65, pp. 219–226, May 2014.
- [113] Y. Zhou, M. A. Baseer, H. Mahfuz, and S. Jeelani, “Monte Carlo simulation on tensile failure process of unidirectional carbon fiber reinforced nano-phased epoxy,” *Materials Science and Engineering: A*, vol. 420, pp. 63–71, Mar. 2006.
- [114] H. K. Jeong and R. A. Shenoi, “Probabilistic strength analysis of rectangular FRP plates using Monte Carlo simulation,” *Computers & Structures*, vol. 76, pp. 219–235, June 2000.
- [115] B. Sudret, “Des é’lé’ments finis stochastiques spectraux aux surfaces de re’ponses stochastiques : une approche unifie’e,” p. 9, 2005.
- [116] B. Sudret, “Stochastic Finite Element Methods and Reliability A State-of-the-Art Report,” p. 189.
- [117] N. Carrere, Y. Rollet, F.-H. Leroy, and J.-F. Maire, “Efficient structural computations with parameters uncertainty for composite applications,” *Composites Science and Technology*, vol. 69, pp. 1328–1333, July 2009.
- [118] S. Marelli and B. Sudret, “UQLab user manual – Polynomial chaos expansions,” p. 66.
- [119] M. Steven Greene, Y. Liu, W. Chen, and W. K. Liu, “Computational uncertainty analysis in multiresolution materials via stochastic constitutive theory,” *Computer Methods in Applied Mechanics and Engineering*, vol. 200, pp. 309–325, Jan. 2011.
- [120] M. Thapa, S. B. Mulani, and R. W. Walters, “Stochastic multi-scale modeling of carbon fiber reinforced composites with polynomial chaos,” *Composite Structures*, vol. 213, pp. 82–97, Apr. 2019.

- [121] F. Massa, T. Tison, and B. Lallemand, “Fuzzy modal analysis: Prediction of experimental behaviours,” *Journal of Sound and Vibration*, vol. 322, pp. 135–154, Apr. 2009.
- [122] H. Q. Do, F. Massa, T. Tison, and B. Lallemand, “A global strategy for the stability analysis of friction induced vibration problem with parameter variations,” *Mechanical Systems and Signal Processing*, vol. 84, pp. 346–364, Feb. 2017.
- [123] F. Massa, T. Tison, and B. Lallemand, “A fuzzy procedure for the static design of imprecise structures,” *Computer Methods in Applied Mechanics and Engineering*, vol. 195, pp. 925–941, Feb. 2006.
- [124] R. Chowdhury and S. Adhikari, “Fuzzy parametric uncertainty analysis of linear dynamical systems: A surrogate modeling approach,” *Mechanical Systems and Signal Processing*, vol. 32, pp. 5–17, Oct. 2012.
- [125] A. Del Mastro, F. Trivaudey, V. Guicheret-Retel, V. Placet, and L. Boubakar, “Investigation of the possible origins of the differences in mechanical properties of hemp and flax fibres: A numerical study based on sensitivity analysis,” *Composites Part A: Applied Science and Manufacturing*, vol. 124, p. 105488, Sept. 2019.
- [126] Z. G. Ghauch, V. Aitharaju, W. R. Rodgers, P. Pasupuleti, A. Dereims, and R. G. Ghanem, “Integrated stochastic analysis of fiber composites manufacturing using adapted polynomial chaos expansions,” *Composites Part A: Applied Science and Manufacturing*, vol. 118, pp. 179–193, Mar. 2019.
- [127] S. L. Omairey, P. D. Dunning, and S. Sriramula, “Influence of micro-scale uncertainties on the reliability of fibre-matrix composites,” *Composite Structures*, vol. 203, pp. 204–216, Nov. 2018.
- [128] C. C. António and L. N. Hoffbauer, “An approach for reliability-based robust design optimisation of angle-ply composites,” *Composite Structures*, p. 7, 2009.
- [129] M. Kalantari, C. Dong, and I. J. Davies, “Multi-objective robust optimization of multi-directional carbon/glass fibre-reinforced hybrid composites with manufacture related uncertainties under flexural loading,” *Composite Structures*, vol. 182, pp. 132–142, Dec. 2017.
- [130] X. Meng, J. Liu, L. Cao, Z. Yu, and D. Yang, “A general frame for uncertainty propagation under multimodally distributed random variables,” *Computer Methods in Applied Mechanics and Engineering*, vol. 367, p. 113109, Aug. 2020.

- [131] D. Notta-Cuvier, F. Lauro, B. Bennani, and R. Balieu, “An efficient modelling of inelastic composites with misaligned short fibres,” *International Journal of Solids and Structures*, vol. 50, pp. 2857–2871, Sept. 2013.
- [132] D. Notta-Cuvier, F. Lauro, and B. Bennani, “An original approach for mechanical modelling of short-fibre reinforced composites with complex distributions of fibre orientation,” *Composites Part A: Applied Science and Manufacturing*, vol. 62, pp. 60–66, July 2014.
- [133] R. Balieu, *Modèle viscoélastique-viscoplastique couplé avec endommagement pour les matériaux polymères semi-cristallins*. PhD thesis.
- [134] M. Nciri, *Modélisation du Comportement des Composites à Fibres Courtes NonAlignées en Dynamique*. PhD thesis.
- [135] J. Lemaitre and J.-L. Chaboche, *Mechanics of Solid Materials*. Cambridge: Cambridge University Press, 1990.
- [136] D. Notta-Cuvier, M. Nciri, F. Lauro, F. Chaari, B. Zouari, and Y. Maalej, “A Pragmatic Approach for Modelling the Viscoelastic-Viscoplastic Behaviour of Short-Fibre Reinforced Thermoplastics Coupled with Anisotropic Damage,” *Applied Composite Materials*, vol. 28, pp. 341–368, Apr. 2021.
- [137] N. Otsu, “A Threshold Selection Method from Gray-Level Histograms,” *IEEE Transactions on Systems, Man, and Cybernetics*, vol. 9, pp. 62–66, Jan. 1979. Conference Name: IEEE Transactions on Systems, Man, and Cybernetics.
- [138] T. Church, “Problems associated with the use of the ratio of Martin’s diameter to Feret’s diameter as a profile shape factor,” *Powder Technology*, vol. 2, pp. 27–31, Sept. 1968.
- [139] N. N. Lal, J. Cornwall, and P. W. Sheard, “Age-related structural changes show that loss of fibers is not a significant contributor to muscle atrophy in old mice,” *Experimental Gerontology*, vol. 156, p. 111618, Dec. 2021.
- [140] W. Pabst, C. Berthold, and E. Gregorová, “Size and shape characterization of polydisperse short-fiber systems,” *Journal of the European Ceramic Society*, vol. 26, pp. 1121–1130, Jan. 2006.
- [141] L. Lundquist, G. Arpin, Y. Leterrier, F. Berthold, M. Lindström, and J.-A. E. Månson, “Alkali-methanol-anthraquinone pulping of *Miscanthus x giganteus* for thermoplastic composite reinforcement: Pulp Fiber-Reinforced Thermoplastics,” *Journal of Applied Polymer Science*, vol. 92, pp. 2132–2143, May 2004.

- [142] A. Bourmaud and S. Pimbert, “Investigations on mechanical properties of poly(propylene) and poly(lactic acid) reinforced by miscanthus fibers,” *Composites Part A: Applied Science and Manufacturing*, vol. 39, pp. 1444–1454, Sept. 2008.
- [143] K. Charlet and A. Béakou, “Mechanical properties of interfaces within a flax bundle – Part I: Experimental analysis,” *International Journal of Adhesion and Adhesives*, vol. 31, pp. 875–881, Dec. 2011.
- [144] Moldex, “Mathematical models and assumption for anisotropic mechanical properties.”
- [145] Moldex, “Mathematical models and assumption for fiber orientation models.”
- [146] F. Lauro, B. Bennani, D. Morin, and A. Epee, “The SEĖ method for determination of behaviour laws for strain rate dependent material: Application to polymer material,” *International Journal of Impact Engineering*, vol. 37, pp. 715–722, June 2010.
- [147] D. C. Nguyen, “Caractérisation de l’interface fibre/matrice: application aux composites polypropylène/chanvre,” p. 126.
- [148] L. Aliotta and A. Lazzeri, “A proposal to modify the Kelly-Tyson equation to calculate the interfacial shear strength (IFSS) of composites with low aspect ratio fibers,” *Composites Science and Technology*, vol. 186, p. 107920, Jan. 2020.
- [149] M. Van Den Oever and H. Bos, “Critical Fibre Length and Apparent Interfacial Shear Strength of Single Flax Fibre Polypropylene Composites,” *Advanced Composites Letters*, vol. 7, p. 096369359800700303, May 1998. Publisher: SAGE Publications Ltd.
- [150] N. Sato, T. Kurauchi, S. Sato, and O. Kamigaito, “Microfailure behaviour of randomly dispersed short fibre reinforced thermoplastic composites obtained by direct SEM observation,” *Journal of Materials Science*, vol. 26, pp. 3891–3898, July 1991.
- [151] J. Holmes, G. Vlandis, Z. Stachurski, R. Das, and P. Compston, “Failure behaviour in woven thermoplastic composites subjected to various deformation modes,” *Composites Part A: Applied Science and Manufacturing*, vol. 146, p. 106410, July 2021.
- [152] H. Zhang and W.-f. Sun, “Mechanical properties and failure behavior of 3D printed thermoplastic composites using continuous basalt fiber under high-volume fraction,” *Defence Technology*, Aug. 2022.
- [153] Y. Wang, M. Lou, and Y. Wang, “Stochastic analysis of failure pressure in reinforced thermoplastic pipes under axial loading and external pressure,” *Ocean Engineering*, vol. 240, p. 109963, Nov. 2021.

-
- [154] M. E. Kazemi, L. Shanmugam, D. Lu, X. Wang, B. Wang, and J. Yang, “Mechanical properties and failure modes of hybrid fiber reinforced polymer composites with a novel liquid thermoplastic resin, Elium®,” *Composites Part A: Applied Science and Manufacturing*, vol. 125, p. 105523, Oct. 2019.
- [155] H. Liu, B. G. Falzon, S. Li, W. Tan, J. Liu, H. Chai, B. R. K. Blackman, and J. P. Dear, “Compressive failure of woven fabric reinforced thermoplastic composites with an open-hole: An experimental and numerical study,” *Composite Structures*, vol. 213, pp. 108–117, Apr. 2019.
- [156] G. F. Gruber, D. Klein, and S. Wartzack, “A modified approach for simulating complex compound structures within early design steps,”
- [157] Y. Zhou and P. K. Mallick, “A non-linear damage model for the tensile behavior of an injection molded short E-glass fiber reinforced polyamide-6,6,” *Materials Science and Engineering: A*, vol. 393, pp. 303–309, Feb. 2005.
- [158] J. J. Horst and J. L. Spoormaker, “Fatigue fracture mechanisms and fractography of short-glassfibre-reinforced polyamide 6,” *Journal of Materials Science*, vol. 32, pp. 3641–3651, July 1997.
- [159] “Mechanism based failure of 3D-printed continuous carbon fiber reinforced thermoplastic composites | Elsevier Enhanced Reader.”
- [160] B. Nghiep Nguyen and V. Kunc, “An Elastic-plastic Damage Model for Long-fiber Thermoplastics,” *International Journal of Damage Mechanics*, vol. 19, pp. 691–725, Aug. 2010.

Abstract

Short-fiber-reinforced thermoplastics (SFRT) are widely used in the automotive sector, especially by the supplier Novares, to build lighter vehicles. Currently, the European Commission directives impose an increase of the proportion of bio-sourced materials in vehicles. However, the use of SFRT in technical parts remains limited due to the lack of reliable prediction of their behavior, considering the variability of material and/or process parameters.

This PhD thesis work aims at experimentally quantify the microstructural variability of short glass or natural fiber thermoplastics, especially in terms of fiber geometry and orientation, and at studying the influence of injection molding process parameters on these variabilities. The impact of microstructural parameters on the dynamic behavior of SFRT is then analyzed, experimentally and numerically.

In a first step, the variability of the Young's modulus is experimentally identified by tensile tests and modal analysis, and then correlated to the variability of the microstructural parameters. In a second step, the impact of the nature of fibers on the failure history under dynamic loading (bulge tests) is investigated. In view of this, experimental data are input into a numerical behavior model that allows considering the specificities of SFRT (viscoelasto-viscoplasticity, anisotropy induced by the orientation of fibers, damage mechanisms...) in order to compare numerical predictions to vibration and dynamic experiments.

Finally, a failure criterion for SFRT is investigated for a wide range of strain rate.

Keywords : Injection molding, Thermoplastic, Short fibers, Plant fibers, Dynamic behavior, Microstructural analysis

Résumé

Les thermoplastiques renforcés par fibres courtes (TRFC) sont très utilisés dans l'automobile, notamment par l'équipementier Novares, afin d'alléger les véhicules, l'incorporation de fibres végétales permettant de plus d'augmenter la proportion de matériaux biosourcés. Toutefois, l'utilisation des TRFC peut être limitée par un manque de prédiction fiable de leur comportement, prenant en compte la variabilité des paramètres matériaux et/ou de process.

Cette thèse vise donc à quantifier expérimentalement les variabilités microstructurales de composites à fibres de verre ou végétales, notamment en termes de géométrie et d'orientation des fibres, et à étudier l'influence des paramètres du procédé d'injection plastique sur ces variabilités. L'impact des paramètres microstructuraux sur le comportement dynamique des TRFC est ensuite analysé, expérimentalement et numériquement.

Dans un premier temps, la variabilité du module d'Young est identifiée à partir d'essais de traction et d'analyses modales expérimentales, puis corrélée à la variabilité des paramètres microstructuraux. Dans un second temps, l'impact de la nature des fibres sur les schémas de rupture sous chargement dynamique (bulge tests) est investigué. Pour cela, les données expérimentales sont exploitées pour alimenter un modèle de comportement numérique permettant de prendre en compte les spécificités des SFRT (viscoelasto-viscoplasticité, anisotropie induite par l'orientation des fibres, mécanismes d'endommagement) afin de confronter les prédictions numériques aux expérimentations vibratoires et dynamiques.

Finalement, un critère de rupture pour les TRFC est proposé pour une large gamme de vitesse de déformation.

Mots clés : Injection plastique, Thermoplastique, Fibres courtes, Fibres végétales, Comportement dynamique, Analyse microstructurale